

Magnetism of atomically laminated MAX phase Mn_2GaC and $(\text{Cr}_{0.5}\text{Mn}_{0.5})_2\text{GaC}$ films

Der Fakultät Physik
der Universität Duisburg-Essen
zur Erlangung des akademischen Grades
eines Doktors der Naturwissenschaften (Dr. rer. nat.)

vorgelegte Dissertation von

Iuliia Pavlovna Novoselova
aus Verkhoturye, Russische Föderation

Day of submission: 18.12.2019

1. Gutachter: Prof. Dr. Michael Farle

2. Gutachter: Prof. Dr. Galina V. Kurlyandskaya

“We are at the very beginning of time for the human race.

It is not unreasonable that we grapple with problems.

But there are tens of thousands of years in the future.

Our responsibility is to do what we can, learn what we can,
improve the solutions, and pass them on.”

Richard P. Feynman

“The Value of Science”. *Engineering and Science*, **19**, 13-55 (1955)

Abstract

MAX phases have attracted interest due to their anisotropic atomically layered structure resulting in a combination of ceramic and metallic properties. The correlation between the complex crystal structure with the here reported magnetic properties in these compounds can become an important element in the development of microelectronic devices of the future. This thesis presents an experimental study of the magnetic properties of $(\text{Cr}_{0.5}\text{Mn}_{0.5})_2\text{GaC}$ and Mn_2GaC MAX phase films measured by ferromagnetic resonance and magnetometry. Both compounds exhibit a complex magnetism due to competing magnetic interactions and its laminar structure.

The $(\text{Cr}_{0.5}\text{Mn}_{0.5})_2\text{GaC}$ films with a thickness of 20.8 to 156 nm show soft magnetic properties at temperature $T = 100$ K with a narrow hysteresis of less than 4 mT and a magnetization M of about 200 kA/m. No dependence of M on the film thickness was observed. The films display a broad magnetic phase transition to a paramagnetic (PM) state above the transition temperature T_t of about 230 K. The 12.5 nm film's surface exhibits a discontinuity in the surface morphology, which results in a magnetic anisotropy increase comparable to the thicker films. The ferromagnetic resonance field μ_0H_r shows a nearly thickness-independent behavior for the 20.8 – 156 nm films. The 20.8 nm film demonstrated magnetic stability at ambient conditions without any capping layer within the time span of 1 year. This stability makes the material a candidate for low-temperature electronic devices used in oxidation-harsh conditions.

The Mn_2GaC film exhibits two magnetic phase transitions within the range of $50 \text{ K} \leq T \leq 850 \text{ K}$. A magneto-structural transition from noncollinear ferromagnetic (FM) to antiferromagnetic (AFM) configuration occurs at $T_t = 214$ K. A second magnetic transition from an AFM configuration to a presumably PM state appears at 507 K. Theoretically predicted competing FM and AFM interactions were observed in the field-dependent magnetization as metamagnetic transitions and as an opening of the hysteresis loop. The magneto-structural transition is accompanied by a large uniaxial magnetostriction effect of 450 ppm along the c -axis. The magnetostriction changes sign above and below the transition, which leads to a compression or an expansion of the lattice spacing along the c -axis. The magnetoresistance showed a similar behavior also with a change of sign. It reaches 3 % at $T = 300$ K. By cooling the Mn_2GaC with an applied magnetic field across the T_t , μ_0H_r decreases to about 30 % and the linewidth decreases to about 40 %. Such response can be explained by a smaller canting angle between the magnetic moments as they align along the applied magnetic field while experiencing magneto-structural transformations. A negative perpendicular magnetic anisotropy constant $K_{2\perp}$ indicates an “easy-plane” magnetic anisotropy, with no preferred orientation within the basal plane of the film.

The results were published in 2 peer-reviewed journals and were presented at 10 international conferences as oral and poster contributions.

Zusammenfassung

MAX Phasen haben durch ihre anisotrope atomare Schichtstruktur und den damit verbundenen keramischen und metallischen Eigenschaften Aufmerksamkeit erregt. Die Korrelation von komplexer Kristallstruktur und beobachteter magnetischer Eigenschaften ist ein wichtiger Aspekt in der Entwicklung zukünftiger mikroelektronischer Bauelemente. Die vorliegende Arbeit untersucht die magnetischen Eigenschaften der MAX Phasen Filme $(\text{Cr}_{0.5}\text{Mn}_{0.5})_2\text{GaC}$ and Mn_2GaC mittels Magnetometrie und Ferromagnetischer Resonanz. Aufgrund der anisotropen laminaren Struktur zeigen die Materialien einen von konkurrierenden Wechselwirkungen beeinflussten komplexen Magnetismus.

$(\text{Cr}_{0.5}\text{Mn}_{0.5})_2\text{GaC}$ Filme mit Dicken von 20.8 nm bis 156 nm zeigten weichmagnetische Eigenschaften bei 100 K mit einer engen Hystereseschleife mit weniger als 4 mT Breite und einer Magnetisierung M im Bereich von 200 kA/m ohne Dickenabhängigkeit. Es wurde ein für konkurrierende magnetische Wechselwirkungen typischer breiter magnetischer Phasenübergang von niedrigen Temperaturen zu einem paramagnetischen (PM) Zustand bei einer Übergangstemperatur T_t von 230 K festgestellt. Die diskontinuierliche Oberflächenmorphologie eines 12.5 nm dicken Films führt zu einer Erhöhung der magnetischen Anisotropie um 30 % im Vergleich zu dickeren Filmen. Ferromagnetische Resonanz (FMR) Messungen zeigen ein nahezu dickenunabhängiges Resonanzfeld für Filmdicken von 20.8 nm bis 156 nm. Eine magnetische Stabilität nach einjähriger Lagerung unter normalen Umgebungsbedingungen wurde für den 20.8 nm dicken Film ohne schützende Deckschicht festgestellt, so dass das Material ein geeigneter Kandidat für die Nutzung in elektronischen Bauelementen unter oxidativen Umgebungsbedingungen sein kann.

Der Mn_2GaC Film zeigt zwei magnetische Phasenübergänge zwischen 50 K und 850 K. Bei $T_t = 214$ K findet ein magneto-struktureller Phasenübergang von einem nicht-kollinearen ferromagnetischen (FM) zu einem antiferromagnetischen (AFM) Zustand statt. Ein Übergang von einem AFM zu einem PM Zustand liegt bei 507 K. Die theoretisch vorhergesagten zuvor genannten konkurrierenden Wechselwirkungen wurden in feldabhängigen Magnetisierungsmessungen als metamagnetische Übergänge und als Öffnung in der Hystereseschleife beobachtet. Der Phasenübergang ist von einer großen uniaxialen Magnetostriktion von 450 ppm entlang der c -Achse begleitet. Der temperaturabhängige Wechsel des Vorzeichens der Magnetostriktion führt zu einer Kompression oder Expansion der c -Achse. Ein entsprechender Vorzeichenwechsel wurde ebenfalls für den Magnetowiderstand beobachtet, dessen Größe 3 % bei $T = 300$ K erreicht. Kühlen des Mn_2GaC Films unter T_t bei angelegtem magnetischem Feld führt zu einer Verringerung des FMR-Resonanzfelds um 30 % und der FMR-Linienbreite um 40 %, was die Folge eines kleineren Verkantungswinkels aufgrund der Ausrichtung der magnetischen Momente entlang des angelegten magnetischen Feldes ist. Die negative uniaxiale magnetische Anisotropiekonstante $K_{2\perp}$ deutet auf eine leichte Ebene ohne Vorzugsrichtung innerhalb der Grundebene des Films hin.

Die erzielten Resultate wurden in zwei peer-reviewed Manuskripten veröffentlicht und auf 10 internationalen wissenschaftlichen Konferenzen als Vortrag oder Poster präsentiert.

Contents

1 Introduction	1
2 Fundamentals	5
2.1 Magnetic order and phase transitions	5
2.2 Magnetic field-induced effects	9
2.3 Magnetic anisotropy	12
2.4 Ferromagnetic resonance	15
2.5 Magnetic MAX phase films	19
2.5.1 Film growth by magnetron sputtering	19
2.5.2 Magnetic properties of related MAX phases	21
3 Experimental methods	25
3.1 Structural analysis	25
3.1.1 X-ray diffraction, X-ray reflectivity	25
3.1.2 Scanning and transmission electron microscopy	27
3.2 Magnetic characterization	29
3.2.1 Magnetometry	29
3.2.2 Magnetoresistance	31
3.2.3 Ferromagnetic resonance	32
4 Results and discussion	39
4.1 $(\text{Cr}_{0.5}\text{Mn}_{0.5})_2\text{GaC}$ films	39
4.1.1 Structural characterization and homogeneity	39
4.1.2 Magnetic phase transition as a function of temperature	45
4.1.3 Angular-dependent ferromagnetic resonance	48
4.1.4 Temperature-dependent ferromagnetic resonance	52
4.1.5 Ferromagnetic resonance with the time span of 1 year	58
4.2 Mn_2GaC film	60
4.2.1 Crystal structure and phase purity	60
4.2.2 Sign reversal of the large uniaxial magnetostriction	63
4.2.3 Field- and temperature-dependent magnetoresistance	66
4.2.4 Magnetic phase transitions	70
4.2.5 Field-dependent magnetization and magnetic entropy change	72
4.2.6 Angular- and frequency-dependent ferromagnetic resonance	76
4.2.7 Temperature-dependent ferromagnetic resonance	82

4.2.8 Correlation of electronic, magnetic and structural properties	87
5 Conclusions	91
6 Outlook	93
7 Appendix	95
A1. Magnetic characterization of the substrate	95
A2. Local homogeneity of the films	97
List of Figures	101
List of Tables	107
List of Publications	109
Acknowledgements	111
Bibliography	113
Erklärung	125

Preface

This thesis is submitted to the University of Duisburg-Essen as one of the required points for the degree Dr. rer. nat. It is based on 2 published papers investigating properties of magnetic films with nanolaminated structure.

This work has been carried out from October 1, 2016 to December 18, 2019 at the Faculty of Physics of the University of Duisburg-Essen under the supervision of Prof. Dr. Michael Farle and co-supervision of Dr. Ruslan Salikhov. The research has been conducted in a collaboration with Linköping University (Sweden), Uppsala University (Sweden) and University of Darmstadt (Darmstadt).

Financial support has been provided by the research grant “Doctoral Programmes in Germany” №57214224 from the Deutsche Akademische Austauschdienst e.V. Experimental consumables were covered by the grant №SA 3095/2-1 from Deutsche Forschungsgemeinschaft.

List of abbreviations

ADF	Annular dark field
AFM	Antiferromagnetic
CVD	Chemical vapor deposition
DFT	Density functional theory
EDX	Energy dispersive X-ray spectroscopy
EPR	Electron paramagnetic resonance
FC	Field cooled
FM	Ferromagnetic
FMR	Ferromagnetic resonance
FW	Field-warmed
FWHM	Full width at half maximum
HAADF	High-angle annular dark field
HR-XRD	High-resolution double-axis X-ray diffraction
LLG	Landau-Lifshitz-Gilbert
MAE	Magnetic anisotropy energy
MCA	Magnetocrystalline anisotropy
MR	Magnetoresistance
MS	Magnetostriction
MSPT	Magneto-structural phase transition
PPMS	Physical property measurement system
PVD	Physical vapor deposition
SC	Superconducting
SED	Secondary electron detector
SEM	Scanning electron microscopy
SQUID	Superconducting quantum interference device
STEM	Scanning transmission electron microscopy
TEM	Transmission electron microscopy
VSM	Vibrating sample magnetometry
XRD	X-ray diffraction
XRR	X-ray reflectivity
ZFC	Zero-field-cooled

1 Introduction

Recent material research focusses on the development of materials that combine properties of multiple nature. Magnetic materials offer a broad span of applications ranging from engineering and materials science to chemistry and medicine [1]. Magnetic micro- and nanostructures are used in sensors [2], detectors [3], electronic components [4] and spintronic devices [5].

Following the trend of miniaturization, the surface quality at interfaces of thin film structures becomes more critical. Thin heterostructures, mono- and multilayers of variable compositions provide a tremendous venue for the research of magnetic interactions due to interface-induced effects in specimens with reduced dimension [6, 7]. Besides the fundamental interest over the last decades, thin films were implemented in microelectronic devices, coatings, energy and memory storage applications, optical electronics and communication technologies [7]. In general, thin film technology consists of three major segments - synthesis, characterization and application. Thin films studied in this thesis were synthesized by magnetron sputtering [8] and characterized by multiple techniques including X-ray diffraction, transmission and scanning electron microscopy, magnetometry and ferromagnetic resonance.

The first discovery of the class of nanolaminated carbides and nitrides was reported by the group of Nowotny [9]. Corresponding compounds that share the same structural features were denominated as $T_xM_yC_z$ where T stands for a transition metal, M for a transition metal or B-group element and C for carbon [9]. The term “nanolaminate” defines a layered structure where the thickness of individual layers is in the nanometer range (fig. 1.1). Therefore, these materials are also known as atomically layered compounds.

In 2000, Barsoum redefined the structural formula to $M_{n+1}AX_n$ and introduced a new name for this class of compounds – MAX phases [10]. In this new notation, M stands for a transition metal, A for an A-group element and X for carbon or nitrogen [10]. Currently, about 155 stable MAX phases are known [11]. The compounds exist as bulk as well as films. Qualitatively, the MAX phases represent nanolaminated structures where the number of $M-X-M$ repetitions is given by an integer n . In this thesis, the MAX phases with $n = 1$ are discussed (fig. 1.1(b)).

The MAX phases possess a combination of ceramic and metallic properties [10, 12]. These features are associated with the crystal structure and the complex chemical bonding. All known MAX phases have a hexagonal structure with the space group $P6_3/mmc$, № 194 in the space group numbers classification [10]. The unit cell consists of 8 atoms that are 2 X , 2 A and 4 M elements (fig. 1.1(a)). The chemical bonding is characterized as a mixture of covalent, ionic and metallic bonds [13]. The MAX phases exhibit strong covalent bonds in $M-X-M$ layers and weaker bonds in $M-A-M$ layers [13].

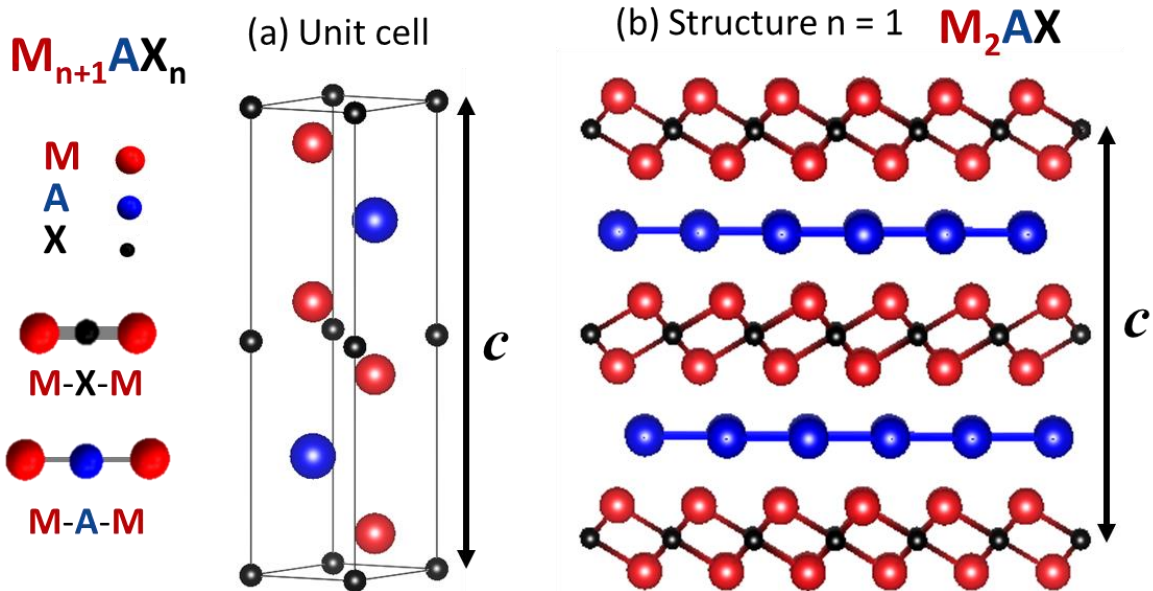


Figure 1.1 (a) $M_{n+1}AX_n$ phase unit cell with the c -axis normal to the basal plane. (b) Nanolaminated $M_{n+1}AX_n$ phase structure with $n = 1$, where the monolayer of the A element is interleaved by $M-X-M$ slabs. M , A and X atoms are colored red, blue and black, respectively. Stronger bonds between $M-X-M$ and weaker bonds between $M-A-M$ layers are schematically shown on the left side by the grey solid lines. Redrawn from [14].

In general, the MAX phases are thermally and electrically conductive, highly resistive against high temperatures, oxidation and chemical treatment, they are machinable and stiff [15]. The Al- and the Si-based compounds such as Ti_2AlC , Ti_3AlC_2 and Ti_3SiC_2 showed self-healing properties after a crack damage [16]. Ti_2AlC has been suggested as a gas burner nozzle in corrosive atmosphere and for heating elements [17]. The Ti-based MAX phases have been discussed as possible candidates for high temperature nuclear applications, and their decomposition and degradation under pressure or ion irradiation has been investigated [18]. Barsoum's review [10] summarizes the potential of MAX phases for applications.

New subclasses emerged in the last years include, for example, quaternary "o-MAX" phases, a subclass which is characterized by a unique out-of-plane chemical ordering of M elements [11, 19]. As a further development, the "i-MAX" phases subclass was discovered with the characteristic in-plane ordering of M -elements according to $(M_{1/3}^1 M_{1/3}^2)_2AX$ [20-22]. The group of J. Rosén predicted and synthesized the first magnetic MAX phase in 2013 that are $(Cr_{0.75}Mn_{0.25})_2GeC$ films with ferromagnetic order up to room temperature [23]. In the following years, an extensive amount of new magnetic MAX phases were synthesized in bulk and in the shape of a film [24-29].

As the research area of magnetic MAX phases is rather new, no established commercialized application has been reported to date, though several directions can be outlined. Mn-based MAX phase films that possess antiferromagnetic (AFM) long-range ordering at room temperature could be used for spintronic devices [30]. AFM

materials are advantageous due to the absence of stray fields and their resistance to external magnetic field perturbations [31]. In addition, they generally possess ultra-fast dynamics and reveal field-/current-induced phenomena [32]. An alternative direction is the creation of MAX phase multilayer systems by deposition of different MAX phase compounds on top of each other. It could result in the discovery of new heterostructures [33]. For example, Mn_2GaC and $(\text{Cr}_{0.5}\text{Mn}_{0.5})_2\text{GaC}$ seem to be suitable candidates due to similar lattice parameters [24, 26, 34], which is favorable for the MAX phase formation, and the possibility to use the same elemental targets.

The nanolaminated nature of the MAX phases has inspired scientists to create 2D graphene-like chemically strongly bonded M-X flakes denoted as MXene by etching the weakly-bonded A elements [35]. A well-described magnetic MAX phase can be considered as a precursor for the synthesis of the first magnetic MXene with anticipated highly anisotropic properties due to the nanolaminated structure. Since magnetic MAX phases can be stabilized in the shape of thin films, an ensemble of MXenes could result in a combination of corrosion resistance, high temperature stability, machinability and other features associated with MAX phases [36].

A narrow magnetic hysteresis loop, as it is reported for MAX phases in the scope of this thesis and in [23, 37], could be used in applications where the material is magnetized in cycles; for example power supply transformers. Alternatively, the MAX phase may be potentially interesting as an active shielding component against magnetic fields, since these phases are able to form continuous films with a thickness-independent magnetic response in a wide range (chapter 4.1.2). Other known materials for this purpose are Si-Fe, Fe-based amorphous and nanocrystalline alloys as well as Fe-Al sandwich composites [38] due to their low coercivity and high permeability. The shielding effectiveness of such soft magnetic materials is often sensitive to the microstructure so that cracks can reduce the operational performance [39]. Therefore, it makes specific MAX phases even more attractive due to the observed high temperature crack-healing effect in Al- and Si-based compounds [16]. Relevant magnetic properties reported in the literature up to date will be discussed in more detail in chapter 2.5.2.

In this thesis, the magnetic characterization of two high-quality magnetic MAX phases in the shape of film, Mn_2GaC and $(\text{Cr}_{0.5}\text{Mn}_{0.5})_2\text{GaC}$, is reported. Their structure with $n = 1$ consists of strongly bonded M-X-M slabs interleaved by monoatomic layers of A element as shown in fig. 1.1(b). In the film, these highly ordered layers are stacked along the c -axis which is oriented normal to the film plane. Selected structural aspects are presented as a part of the collaboration project (DFG, №SA 3095/2-1) and discussed to complement the obtained results. This contribution includes X-ray diffraction, X-ray reflectometry and transmission electron microscopy studies (chapters 4.1.1., 4.2.1).

In chapter 2, an overview of the general concepts of magnetism that are related to the thesis results are given. Chapter 3 contains a brief description of the experimental techniques and setups used through this thesis. Chapter 4 includes the discussion of the results obtained in this thesis, where chapter 4.1 is devoted to $(\text{Cr}_{0.5}\text{Mn}_{0.5})_2\text{GaC}$ and chapter 4.2 to Mn_2GaC .

The thin film approach can be used to tailor the surface magnetism of MAX phases. Varying the number of layers has an influence on the magnetic characteristics of the compound. There are few studies investigating thickness-dependent structural and magnetic properties regarding MAX phase films in the literature [23, 26]. Therefore, an influence of the thickness on magnetic properties was studied on the quaternary $(\text{Cr}_{0.5}\text{Mn}_{0.5})_2\text{GaC}$ MAX phase and is presented in chapters 4.1.2 - 4.1.3.

The ceramic nature of the MAX phases is expected to manifest itself in enhanced material properties such as high temperature stability and oxidation resistance [10]. In the scope of this thesis, the long-term stability of magnetic parameters at ambient conditions was tested and presented in chapter 4.1.4.

The research on magnetic phase transitions was conducted by magnetometry and ferromagnetic resonance (FMR), the results are given in chapters 4.1.2 - 4.1.5 and 4.2.3 - 4.2.7. An observed magneto-structural phase transition resulted in a uniaxial magnetostriction, which is discussed in chapter 4.2.2.

The calculated magnetic ground state of the Mn-based magnetic MAX phase films revealed a long-range magnetic order with AFM and FM states that are very close in energy [40]. Such narrow lying states are expected to be very sensitive to applied external stimuli. Therefore, a magnetic response to magnetic fields and temperature was examined. Theoretical studies predicted a long-range AFM order in Mn_2GaC at room temperature and a critical order-disorder temperature of approximately $660\text{ K} \pm 20\%$ [41]. A magnetometry at high temperatures has been performed to study this transition, which is presented in chapter 4.2.4 – 4.2.5.

Magnetoresistive appliances are critical components for a wide variety of technological applications such as spintronics [42], high-density storage [43], non-destructive testing [44] or location monitoring devices [45]. The electrical resistivity and the magnetoresistance (MR) of Mn_2GaC are investigated as a function of temperature and an external magnetic field in chapter 4.2.3.

Magnetic anisotropy of $(\text{Cr}_{0.5}\text{Mn}_{0.5})_2\text{GaC}$ and Mn_2GaC was determined by a temperature-, frequency- and angular-dependent FMR (chapters 4.1.3, 4.2.7).

2 Fundamentals

The following chapter gives an overview on the fundamental aspects of magnetism that are relevant for the analysis of the experimental results obtained in this thesis. It includes an introduction into the concepts of the magnetic order in solids, magnetic transitions, changes in structure and electrical resistivity under applied magnetic field, types of magnetic anisotropy and magnetic resonance. The description of each part is supported by references with more detailed information.

2.1 Magnetic order and phase transitions

Magnetic order

All materials exhibit magnetic behavior that is different in nature. They can be classified by a magnetic response of a material to an applied magnetic field. This quantity is the magnetic susceptibility, which is generally defined as $\chi = M/H$ with the magnetization M , represented by the sum of the magnetic moments per unit volume, and the applied magnetic field H [46]. At high temperature paramagnetic (PM) and diamagnetic (DM) materials, show a positive and negative linearly field-dependent χ .

Diamagnetism has two general descriptions: Langevin and Landau [47]. Langevin's theory characterizes materials with filled electronic shells of atoms. Landau theory introduces diamagnetism in metals as a free electron gas due to non-localized electrons. PM materials may possess Pauli or Curie paramagnetism [47]. Pauli paramagnetism in metals arises due to the weakly interacting conduction electrons. It is temperature-independent and smaller than the Curie paramagnetism [47]. The latter is associated with localized spin and orbital magnetic moments in a magnetic field, for which the Curie law is often written as [47]

$$\chi = \frac{C}{T}, \quad C = \frac{n\mu_0\mu_B^2}{k_B}, \quad (2.1)$$

with the temperature T , the Curie constant C , the number of magnetic moments per unit volume n , the magnetic permeability of free space μ_0 , the Boltzmann constant k_B and the Bohr magneton μ_B .

In contrast, for ferromagnets and antiferromagnets, χ is a complex quantity due to the magnetic moments coupling in such materials [46], which is the result of the short-range exchange interaction [48] and can be characterized by a magnetostatic exchange length given by [49, 50]

$$l_{ex} = \sqrt{\frac{A}{\mu_0 M_s^2/2}} = \sqrt{\frac{A}{K_d}}, \quad (2.2)$$

where A is the exchange constant, M_s is the saturation magnetization, and K_d is the maximum demagnetization energy density. For Fe, l_{ex} is about 2.3 nm [50]. At M_s , all magnetic moments are aligned along the direction of an applied magnetic field. The exchange constant is positive for a ferromagnet and negative for an antiferromagnet[47].

Materials that contain several phases often exhibit a combination of magnetic components, and the total χ is expressed as a sum of these contributions:

$$\chi_{total} = \chi_{DM} + \chi_{PM} + \chi_{FM} + \chi_{AFM} + \dots \quad (2.3)$$

The schematic representation of the four conventional types of magnetic order is shown in fig. 2.1. Besides PM, FM and AFM, it generally includes a ferrimagnetic order. These types are largely expanded to a magnetic family tree [47, 51] that defines more sophisticated types of magnetic order. The most known are spin glasses with frustrated magnetic interactions due to randomly oriented frozen magnetic moments; superpara- and metamagnets as well as more complex noncollinear magnetic configurations such as helical magnets [47]. A typical arrangement of the magnetic moments in a PM material is shown in fig. 2.1(a) when no magnetic field is applied, and the magnetic moments are randomly oriented. By applying the external magnetic field, the magnetic moments align along the field direction. After removing the external field, the magnetic moments re-orient randomly again due to the thermal fluctuations of the magnetic system. Figs. 2.1(b) - (d) display magnetic materials with coupled magnetic moments caused by the exchange interaction [52]. In FM materials the magnetic moments are aligned in parallel, while ferrimagnetic materials are characterized by two sublattices with unequal magnetic moments oriented antiparallel. AFM materials show an antiparallel orientation of equal magnetic moments.

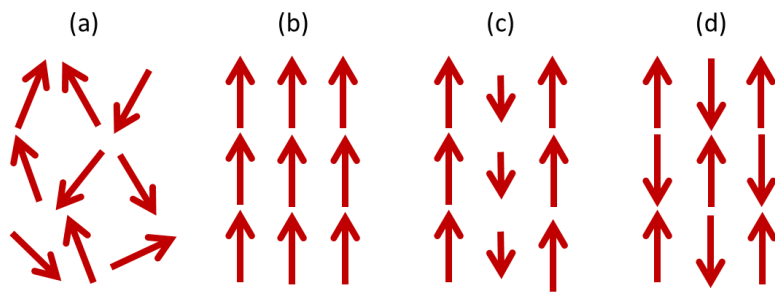


Figure 2.1 Classical types of magnetic order in (a) paramagnetic, (b) ferromagnetic, (c) ferrimagnetic, and (d) antiferromagnetic solid materials. Red arrows indicate orientation of the magnetic moments. Redrawn from [47].

A FM material is generally described by a hysteresis behavior of the magnetization M under applied magnetic field [52]. A complete magnetization cycle is displayed in fig. 2.2. FM materials are classified to be magnetically soft and hard [47] by the coercivity H_c for which the difference between some of the softest (about

0.1 A/m for α Fe-Co-B) and the hardest (about 10⁶ A/m for Nd-Fe) materials may reach more than eight orders of magnitude [47]. H_c defines the field of a magnitude, where M reverses under an applied magnetic field. The saturation magnetization M_s for classical materials such as Fe, Ni and Co are 1720, 485 and 1370 kA/m [47], respectively. At the zero external magnetic field, the remanent magnetization M_r persists, which possesses a reduced magnitude with respect to M_s due to the nucleation of magnetic domains.

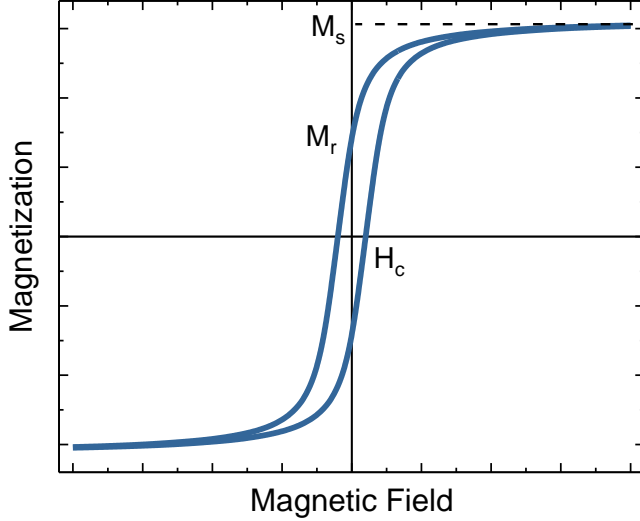


Figure 2.2 Magnetic field-dependent magnetization for an arbitrary ferromagnetic material. The saturation magnetization M_s , the coercive field H_c and the remanent magnetization M_r are indicated.

The form of the magnetic hysteresis depends on the potential coexistence of more than one magnetic phase, magnetic domains, and the direction of the applied magnetic field with respect to crystallographic directions and the overall shape of the material (magnetocrystalline and shape anisotropy). Magnetic domains form in order to minimize the magnetostatic contribution stray fields outside of the materials to the total energy [53]. Differently oriented magnetic domains are separated by so called domain walls, where the magnetic moments rotate from one direction to another. The Bloch and the Néel domain walls are schematically presented in fig. 2.3.

The dynamics and structure of domain walls are significantly influenced by local characteristics of a material. A domain wall can get pinned at defects of the material; this pinning can be weak or strong depending on the type of defects [47]. In general, a domain wall pinning tends to increase H_c of the material [52]. Besides, specimens such as multilayer systems can stabilize different patterns; for instance, the remanent domain configuration of Co/Pt multilayer films can be tuned from bubbles to stripes as a function of an applied magnetic field [54].

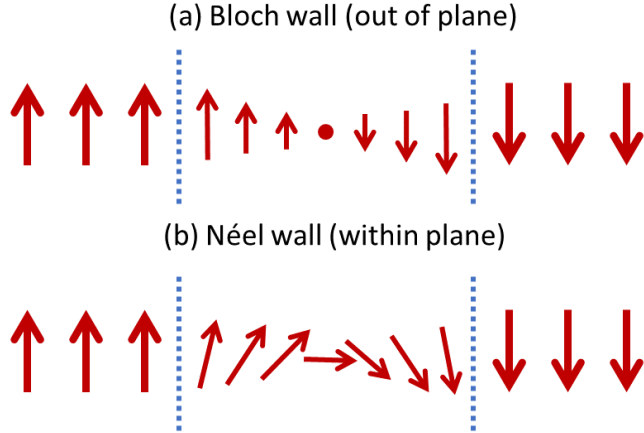


Figure 2.3 Representation of a domain wall of (a) Bloch and (b) Néel type. The domain wall is the area between the blue dashed lines. Adapted from [52].

Magnetic phase transitions

Ferromagnets and antiferromagnets are magnetically ordered materials (fig. 2.1). At higher temperatures, thermal fluctuations overcome the magnetic exchange and reduce the (sublattice) magnetization. Transitions between magnetic states occur at the Curie temperature T_c for ferromagnets and the Néel temperature T_N for antiferromagnets [55]. In both cases, a material undergoes a transition to a PM state with increasing T . In general, these phase transitions are reversible when the microstructure of the sample does not irreversibly change as a function of temperature. In this thesis, it is shown that the magnetization of Mn_2GaC loses this reversibility when heated up to $T = 850$ K (chapter 4.2.5).

In the scope of the molecular field theory, the magnetization can be expressed by the Brillouin function $B_J(x)$ [47]

$$M = M_0 B_J(x), \quad M_0 = n g_J \mu_B J, \quad (2.4)$$

where n is the number of magnetic atoms per volume, g_J is the Landé g-factor and J is the total angular momentum quantum number [47]. $B_J(x)$ is a quantum statistical formulation for PM materials which includes J , the Boltzmann constant k_B and the temperature- and field-dependent parameter x defined by the ratio between the Zeeman and thermal energies [55]. Combining eq. 2.4 and $\chi = M/H$, a solution for the temperature-dependent χ , that is the Curie-Weiss law, can be obtained [55]:

$$\chi = \frac{C}{T - T_c}, \quad C = \frac{n_w n \mu_0 g_J^2 J (J+1) \mu_B^2}{3 k_B}, \quad (2.5)$$

with C as the Curie constant. A ferromagnet becomes a paramagnet at $T > T_c$ and χ diverges at $T = T_c$ [47].

AFM order in materials implies the existence of equal magnetic moments with oppositely oriented sublattices “A” and “B” [47]. In the molecular field theory, the antiparallel orientation of neighboring magnetic moments has to be taken into account. The net magnetization $M = M_A + M_B$ is zero as $M_A = -M_B$. Considering two antiparallel sublattices, the internal fields can be defined as [47]:

$$\begin{aligned} H_A^i &= n_{AA}M_A + n_{AB}M_B + H, \\ H_B^i &= n_{BB}M_B + n_{BA}M_A + H \end{aligned} \quad (2.6)$$

with $n_{BB} = n_{AA}$ and $n_{AB} = n_{BA}$. The spontaneous magnetization of each sublattice marked $\alpha = A, B$ is expressed by [47]:

$$M_\alpha = M_{\alpha 0}B_J(x_\alpha) = \left(\frac{n}{2}\right)g_J\mu_BJB_J(x). \quad (2.7)$$

The result for a PM region above T_N with $\chi = C/T$ and $M_\alpha = \chi H_\alpha^i$ is the Curie-Weiss law written with the paramagnetic Curie temperature θ_P [47]:

$$\chi = \frac{2C}{T+\theta_P}. \quad (2.8)$$

By applying a large enough magnetic field it is possible to reorient the magnetization into a parallel direction [47]. In general, one distinguishes a first- and a second-order magnetic phase transitions [52] according to the order of the free energy differential that may display a discontinuity [52]. For the transition of the first-order, an abrupt change in the first derivative of the free energy is anticipated, which involves volume, entropy or magnetization M . For the second-order transition, the heat capacity or χ experience a discontinuous change in the second derivative of the free energy [52].

2.2 Magnetic field-induced effects

Magnetocaloric effect

A first-order transition is accompanied by an absorption or release of heat (energy) and is characterized by a thermal hysteresis [52]. This effect can be studied by the isothermal entropy change ΔS or adiabatic temperature change ΔT and, typically, it defines the presence of the magnetocaloric effect (MCE) that results from magneto-structural transformations [47, 56]. The internal energy $U(S, V, (H, M))$ of a magnetic material depends on the entropy S , the volume V and the magnetic field H or M [56], so it experiences changes upon an applied magnetic field. The MCE described by an entropy change ΔS , which is defined for isobaric conditions [56] as

$$dS = \left(\frac{\partial S}{\partial T}\right)_H dT + \left(\frac{\partial S}{\partial H}\right)_T dH. \quad (2.9)$$

By integrating eq. 2.9 over a magnetic field in the range $0 \leq \mu_0 H \leq H$, the isothermal entropy change ΔS associated with the $M(H)$ change is written as [56]:

$$\Delta S_M = \int_0^H \left(\frac{dM}{dT}\right)_H dH \rightarrow \Delta S_M \left(\frac{T_1+T_2}{2}\right) = \frac{1}{T_2-T_1} \left[\int_0^H M(T_2, H) dH - M(T_1, H) dH \right], \quad (2.10)$$

where T_1 and T_2 are temperatures of the two neighboring isotherms. Experimentally magnetization curves are commonly recorded at fixed temperatures (chapter 4.2.4) or fixed magnetic fields [57].

Magnetostriction

A magnetic material can change its size and shape under an applied magnetic field. This effect is known as the magnetostriction (MS) and is governed by the coupling between spin and lattice structure [58]. Firstly, it was observed on iron bars by J. Joule in 1842 as a microscopic change in lateral size [59]. Thin magnetic films deposited on a substrate often exhibit strain due to a lattice mismatch between the film and the substrate [60].

On the microscopic scale, MS results from the interatomic distance changes depending on magnetic and electronic exchange interactions within the material. Spontaneous MS can appear while crossing the T_c when the domains are forming and its average value can be described as the sum of the domains spontaneous MS within the material [61]. The field-induced MS reflects the growth of energetically favorable domains under the external magnetic field, which causes a domain boundary motion and, thus, strain [61].

On the macroscopic scale, two processes stand out, both related to the domain structure of a FM material. The first one is the domain wall motion whilst the external magnetic field application [62]. The second mechanism is a rotation of the domains itself [62]. The combination of these phenomena leads to a physical size change of the material under the influence of a magnetic field [62]. One of the best known magnetostrictive materials, Terfenol-D that is Tb-Dy-Fe, exhibits a strain of about 200 - 2500 ppm [63, 64] at room temperature, in comparison to about -1200 ppm in amorphous Sm-Fe-B films and about 500 ppm in Tb-Dy-Fe/Nb multilayers [65]. The uniaxial magnetostriction value λ , which is the deformation or strain caused in two-dimensional space or parallel to an applied magnetic field is defined as [61]

$$\lambda = \frac{\Delta l}{l_0} = \frac{l-l_0}{l_0}, \quad (2.11)$$

where l_0 is the initial length of the sample and l is the resulting length after applying the external magnetic field. This general approach can be used to study the change of

the sample dimensions at a nanoscale by comparing the interplane distances of the crystal lattice.

In the scope of this thesis, the interplane distances of the Mn₂GaC film were studied by high-resolution X-ray diffraction measurements as a function of a magnetic field applied parallel to the film plane. The uniaxial magnetostriction at two selected temperatures below and above the magneto-structural phase transition is discussed in chapter 4.2.2.

Magnetoresistance

The change in electrical resistance upon the application of a magnetic field, is called magnetoresistance (MR) and is widely used in modern technological devices. The classification of a MR is defined by the effect's magnitude. For instance, it includes anisotropic (AMR), giant (GMR), tunnel (TMR), colossal (CMR) and extraordinary (EMR) MR, for which the magnitudes vary from a few to hundreds percent [47, 55]. The GMR effect discovered by A. Fert and P. Grünberg in 1988 [66, 67] initiated the development of GMR-based sensors. For almost two decades, these sensors are components of magnetic data storage devices [31].

The electrical resistance usually increases with increasing temperature as the thermal motion in the crystal lattice grows [68]. In fact, in an ideally ordered metallic crystal at the temperature of 0 K, an anticipated resistance for the current flow is zero [68]. On the other hand, a real crystal contains inhomogeneities and imperfections shown in figs. 2.4(a) - (b), which decrease the conductivity and mobility due to the electron scattering occurring on these defects [68]. The mean free path λ_* is the path of an electron between two collisions with ions within the relaxation time τ [47]. According to the free electron model [47], it is described as

$$\lambda_* = v_F \times \tau, \quad v_F = \sqrt{2E_F/m_e}, \quad (2.12)$$

where v_F is the Fermi velocity, which defines the electrons velocity and E_F is the Fermi energy. The theory for the resistivity in metals has been analytically formulated within the frame of the Bloch-Grüneisen approach [55]. For metallic compounds the temperature dependence of the resistivity changes from T^5 at low temperatures to a linear increase at high temperatures, because the influence of lattice-vibrations becomes dominant over dislocations, defects and impurities [69], which is schematically presented in fig. 2.4(c). Typically, this dependence is described using a linear approximation [70]:

$$\rho(T) = \rho_0(1 + \alpha(T - T_0)), \quad (2.13)$$

where ρ_0 is the resistivity at T_0 and α is the temperature coefficient of the resistivity.

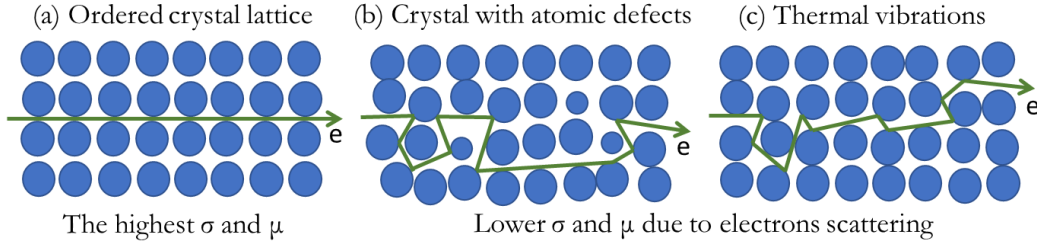


Figure 2.4 Representation of an electron e scattering path (green arrow) through (a) ordered crystal lattice, (b) crystal lattice with atomic defects and imperfections and (c) ordered crystal lattice that experience thermal vibrations. σ is the electrical conductivity and μ is the electron mobility. The drawing is adapted from [69].

MR in thin films can be totally different from the bulk values as the commonly assumed model of an infinite crystal with a periodic potential for the conduction bands calculation should be modified due to the film edges and film dimensions [71]. In general, a conductive material possesses a resistance, which changes as a function of the magnetic field due to the Lorentz force moving the electric charge under external magnetic fields [47]. Therefore, the relation between resistivities with $\rho(H)$ and without $\rho(H = 0)$ an external magnetic field defines the MR as [47]

$$MR = \frac{\rho(H) - \rho(H=0)}{\rho(H=0)}. \quad (2.14)$$

The dimensionless residual resistivity ratio (RRR) can be used as an estimation of the purity of the sample as it varies depending on impurities and defects within the material [72]. It can be calculated as follows [72]:

$$RRR \sim \frac{\rho(T=300\text{ K})}{\rho(T=0\text{ K})}, \quad (2.15)$$

where $\rho(T)$ is the resistivity at a fixed temperature. For the case of $T = 0$ K, the lowest temperature achieved in experiment is considered. A high RRR means a small resistance at low temperatures, what could be a sign of a small amount of imperfections within the material. For example, the RRR for a copper varies between 10 and 100, while in defect free pure metals the values can be above 10000 [72].

2.3 Magnetic anisotropy

The magnetic anisotropy energy (MAE) defines the energy difference between easy and hard orientations of the magnetization. If an external field is aligned in the easy direction, the saturation magnetization is reached at lower fields than when aligned

along the so-called “hard” direction. The general description is given in the current paragraph using the Gibbs free energy density F_G as the sum of several energetic contributions [73]:

$$F_G = F_Z + F_{sh} + F_{ex} + F_{me} + F_{mca} \dots \quad (2.16)$$

with the Zeeman F_Z , the shape F_{sh} , the exchange F_{ex} , the magnetoelastic F_{me} and the magnetocrystalline F_{mca} contributions.

The Zeeman energy F_Z is the energy of a system under an applied external magnetic field, which is written with respect to rotational angles (fig. 2.5) as:

$$F_Z = - \vec{M} \cdot \vec{H} (\sin\theta \sin\theta_H \cos(\varphi - \varphi_H) + \cos\theta \cos\theta_H). \quad (2.17)$$

The generated demagnetization field in a FM specimen points to the opposite direction of the magnetization [47]. The minimization of this stray field defines a magnetic domain pattern. The corresponding magnetic shape anisotropy F_{sh} which appears due to the magnetic dipole-dipole interaction is given as [74]

$$F_{sh} = \frac{\mu_0}{2V} \int \vec{M} \bar{\bar{N}} \vec{M} dV, \quad (2.18)$$

where V is the sample volume and $\bar{\bar{N}}$ is the demagnetization tensor, taking into account the shape of the sample [46]

$$\bar{\bar{N}} = \begin{pmatrix} N_1 & 0 & 0 \\ 0 & N_2 & 0 \\ 0 & 0 & N_3 \end{pmatrix}. \quad (2.19)$$

F_{sh} of a thin film is defined as [60]

$$F_{sh} = \frac{1}{2} (N_{\perp} - N_{\parallel}) \mu_0 M_s^2 \cos^2 \theta, \quad (2.20)$$

where the demagnetization factor N_i is a component of $\bar{\bar{N}}$, for an applied magnetic field parallel and perpendicular to the specimen, N_{\perp} and N_{\parallel} are defined, respectively. For an infinitely thin film approximation, these terms are $N_{\perp} = 1$ and $N_{\parallel} = 0$ [60].

The exchange (EX) energy density F_{ex} is defined by interactions that arise between adjacent magnetic dipoles due to exchange interaction [73]. It is defined by the nearest neighbor spins S_i and S_j and the exchange coupling constant J :

$$F_{ex} = -JS_i S_j. \quad (2.21)$$

The magnetoelastic (ME) energy F_{me} describes the deformation of the material under the external magnetic field due to the magnetostriction as an internal factor and due to the external stress as a magneto-mechanic response [46].

The magnetocrystalline anisotropy (MCA) energy density F_{mca} reflects favorable crystallographic easy directions, where magnetic moments prefer to be aligned [46]. In the case magnetic moments align along a hard direction, F_{mca} may result in a significant contribution to the free energy density [60]. This contribution appears mainly due to the spin-orbit interaction, and it is sensitive to the crystallographic axes [60]. For hexagonal sample systems that are investigated in this work, F_{mca} is expressed by [60]

$$F_{mca} = K_2 \cos^2 \theta + K_4 \sin^4 \theta + K_6 \sin^6 \theta \cos^6 \varphi, \quad (2.22)$$

where K_n is the magnetocrystalline anisotropy constant of different orders, θ and φ are rotational angles with respect to an applied magnetic field. The coordination system for a specimen in the film shape is presented in fig. 2.5. The polar angle θ gives the orientation of the magnetization with respect to the c -axis, where $\theta = 0^\circ$ defines the orientation normal to the film plane. The azimuthal angle φ defines the angle within the basal plane and, thus, characterizes the anisotropy energy which is needed to rotate M in the plane perpendicular to the c -axis.

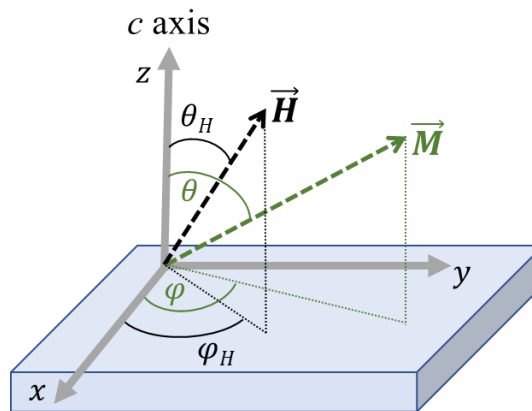


Figure 2.5 Representation of the film geometry with respect to an external magnetic field \vec{H} , resulting magnetization \vec{M} and corresponding azimuthal φ_H and polar θ_H angles for \vec{H} . Redrawn from [75].

All above mentioned contributions compete with each other in order to minimize the total energy F_G . It may result in a change of material properties under external stimuli such as temperature, external magnetic field or mechanical stress. For a detailed description, the reader is referred to [31].

There are two specific sources of the MCA origin outlined in the literature: the single- and the two-ion contribution [47]. The single-ion magnetic anisotropy is

described by the crystal-field interaction between the electrons in their orbitals and the potential on the atomic site caused by the surrounding atoms. This spin-orbit coupling results in the preferred crystallographic alignment of the magnetic moments [47].

The two-ion magnetic anisotropy is related to the dipole-dipole interaction and to an anisotropic exchange. The dipole-dipole interaction is negligible for certain lattices such as cubic ones and can be significant for noncubic lattices. An anisotropic exchange could appear due to spin-orbit coupling as higher-order corrections to the isotropic Hamiltonian of the Heisenberg model which results in the alignment of the exchange-coupled pairs [47].

The temperature dependence of K and M based on a spin fluctuation theory was described by Callen and Callen [76]. This theory formulates a universal relation between the reduced K and the reduced M for a single-ion anisotropy in a ferromagnet

$$\frac{K(T)}{K(0)} = \left(\frac{M(T)}{M(0)} \right)^\alpha \quad (2.23)$$

with the exponent $\alpha = 3$ for uniaxial anisotropy [77]. The result of $\alpha = 2.9$ that is close to the theory was obtained for the out-of-plane uniaxial anisotropy in uncapped Fe ultrathin film on GaAs in the case of a negligible fourth-order anisotropy constant K_4 [77]. The smaller exponent of $\alpha = 2.1$ obtained for FePt films was explained by the two-ion anisotropy that dominates over the expected single-ion contribution due to the induced Pt moments [78].

In this work, ferromagnetic resonance (FMR) experiments were performed to study the magnetic anisotropy of $(\text{Cr}_{0.5}\text{Mn}_{0.5})_2\text{GaC}$ and Mn_2GaC films. A theoretical background of FMR is discussed in chapter 2.4, the experimental details are given in chapter 3.2.3, and the results are presented in chapters 4.1.3 – 4.1.5 and 4.2.6 – 4.2.7.

2.4 Ferromagnetic resonance

The resonant absorption of a radiofrequency magnetic field in a FM sample, under the condition of an applied uniform magnetic field \vec{H} , is known as FMR [73]. The uniform magnetic field is oriented perpendicularly to the oscillation plane of the radiofrequency magnetic field [73]. By defining the resonance field position $\mu_0 H_r$ and linewidth ΔH , an information about the magnetic anisotropy, magnetic relaxation and damping processes, magnetization and g -factor can be obtained. Angular dependent measurements are used for the calculation of magnetic anisotropy constants, frequency dependent measurements can be used for the damping and g -factor estimation, while temperature-dependent measurements allow to study the magnetic phase transitions of the sample.

The theoretical description is based on the precessional motion of the magnetization around the orientation of an effective magnetic field $\mu_0 \vec{H}_{eff}$. This effective magnetic field consists of multiple field contributions, including the applied external magnetic field, the high-frequency magnetic field of the microwave, the magnetic anisotropy field. The motion of the magnetization is described by the Landau-Lifshitz-Gilbert equation (LLG) [73]:

$$\frac{d\vec{M}}{dt} = -\gamma(\vec{M} \times \mu_0 \vec{H}_{eff}) + \frac{\alpha}{M_s} \left[\vec{M} \times \frac{d\vec{M}}{dt} \right], \quad (2.24)$$

The first summand of eq. 2.24 describes the precession of the magnetization around an equilibrium position defined by $\mu_0 \vec{H}_{eff}$. The second summand adds the relaxation of the magnetization towards the equilibrium position, with α as the dimensionless Gilbert damping parameter [79].

Due to the excitation by the radiofrequency magnetic field the magnetization of the sample is slightly deflected out of its equilibrium position. In this case the magnetization is defined as [73]

$$\vec{M} = \vec{M}_s + \vec{m} e^{i\omega t} \quad (2.25)$$

with the saturation magnetization \vec{M}_s and a time-dependent high frequency magnetization \vec{m} :

$$\vec{m} = \bar{\chi} \vec{h}, \quad (2.26)$$

where \vec{h} is the radiofrequency magnetic field and $\bar{\chi}$ is the complex high frequency susceptibility tensor [73]:

$$\bar{\chi} = \begin{pmatrix} \chi_{xx} & i\chi_{xy} & 0 \\ -i\chi_{yx} & \chi_{yy} & 0 \\ 0 & 0 & 0 \end{pmatrix}. \quad (2.27)$$

When the radiofrequency magnetic field is polarized along a single direction, a relation between a corresponding component of $\bar{\chi}$ and the absorbed power of the radiofrequency field by the sample can be derived. This component is a complex number consisting of a dispersion component (real part) and an absorption component (imaginary part). The imaginary part of a component of $\bar{\chi}$ is proportional to the absorbed microwave power by the sample in resonance [75]. An approximation of a resonance condition including azimuthal and polar angular dependencies of the magnetization M (fig. 2.5) is given by the Smit-Beljers approach [80]:

$$\frac{\omega}{\gamma} = \frac{\sqrt{1+\alpha^2}}{M \sin(\theta)} \sqrt{\frac{\partial^2 F}{\partial \theta^2} \frac{\partial^2 F}{\partial \varphi^2} - \left(\frac{\partial^2 F}{\partial \theta \partial \varphi} \right)^2}. \quad (2.28)$$

The resonance condition provides an expression of the resonance field as a function of the external magnetic field angles for a fixed frequency. The free energy F includes energy density terms that depend on the crystal symmetry and shape of the specimen (chapter 2.3). For the samples investigated in this thesis, the case of thin films with hexagonal symmetry is considered. Thus, the free energy density F can be written as following [60]:

$$F = \frac{1}{2} \mu_0 M_s \cos^2 \theta - K_2 \cos^2 \theta - \mu_0 M_s H (\cos \theta \cos \theta_H + \cos(\varphi - \varphi_H) \sin \theta \sin \theta_H) \quad (2.29)$$

with terms for demagnetization, uniaxial magnetocrystalline (in first order only) and Zeeman energies, respectively. All terms are stated as a function of polar and azimuthal angles. For FM thin films without pronounced magnetic anisotropy in the film plane, the demagnetization factors in the shape anisotropy term are $N_{\perp} = 1$, $N_{\parallel} = 0$ [60]. In that case and when the field is applied perpendicular $\mu_0 H_{r\perp}$ or parallel $\mu_0 H_{r\parallel}$ to the film plane, the resonance condition is written as [60]

$$\frac{\omega}{\gamma} = \mu_0 (H_{r\perp} - \mu_0 M_s + \frac{2K_{2\perp}}{M_s}),$$

$$\left(\frac{\omega}{\gamma} \right)^2 = \mu_0^2 H_{r\parallel} (H_{r\parallel} + \mu_0 M_s - \frac{2K_{2\perp}}{M_s}) \quad (2.30)$$

For these particular cases, the contribution of the effective magnetic anisotropy is described in terms of the effective magnetization $\mu_0 M_{eff} = \mu_0 M_s - 2K_{2\perp}/M_s$. The uniaxial perpendicular magnetic anisotropy constant $K_{2\perp}$ has two contributions, the volume K_v and the surface anisotropy K_s . In order to determine $K_{2\perp}$, $\mu_0 M_{eff}$ can be expressed as [46]

$$\mu_0 M_{eff} = \mu_0 M_s - \frac{2K_2}{M_s}, \quad K_2 = K_v + \frac{2K_s}{d}, \quad (2.31)$$

where d is the film thickness, and K_s consists of the film/substrate K_i^{FS} and the film/air K_i^{FA} contributions that are measured simultaneously and, thus, cannot be unambiguously separated. Therefore, the coefficient 2 used in front of K_s averages both contributions [60]. According to eq. 2.31, the surface contribution increases with decreasing film thickness.

The linewidth of an FMR signal gives an information regarding the magnetic relaxation process, sample inhomogeneities, and it is related to the intrinsic Gilbert

damping constant α [60]. In the representation of magnetic field terms, the linewidth can be formulated as a function of frequency [81, 82]:

$$\Delta H(f) = \Delta H_0 + \Delta H_G + \Delta H_{2m} + \Delta H_{LF}, \quad (2.32)$$

with ΔH_0 as the inhomogeneous broadening term describing intrinsic defects. The Gilbert damping is described by $\Delta H_G = \frac{4\pi\alpha f}{\sqrt{3}\gamma}$. For thin films often only $\Delta H_0 + \Delta H_G$ terms have been employed to evaluate magnetic damping of the system, although other contributions are known to cause a deviation from the linear behavior. Low-field losses expressed by [83]

$$\Delta H_{LF} = \Delta H_{low}/f^n \quad (2.33)$$

may contribute due to a microwave field inhomogeneity giving a sharp rise at low fields as it was observed for annealed Heusler alloys $(Co_2Mn)_{1-x}Ge_x$ [83]. The two-magnon scattering mechanism for a thin film can be expressed by [84]

$$\begin{aligned} \Delta H_{2m}(\omega, \theta_H, \varphi_H) = & \sum_{\langle x_i \rangle} \Gamma_{\langle x_i \rangle} f(\varphi_H - \varphi_{\langle x_i \rangle}) \times \\ & \times \arcsin \left[\sqrt{\frac{\sqrt{\omega^2 + (\omega_0/2)^2} - \omega_0/2}{\sqrt{\omega^2 + (\omega_0/2)^2} + \omega_0/2}} \right] \times U(\theta_{eq} - \theta_c), \end{aligned} \quad (2.34)$$

where the parameter $\Gamma_{\langle x_i \rangle}$ defines how strong is the two-magnon scattering along the crystallographic *in-plane* direction $\langle x_i \rangle$, and $U(\theta_{eq} - \theta_c)$ is the step function to evaluate a critical *out-of-plane* angle, where the two-magnon scattering vanishes. A detailed description about parameters determination is given in [84]. A line broadening caused by mosaicity as a result of a parameters variation in sample regions is formulated in [84] to describe a magnetic relaxation of Fe_3Si films as

$$\Delta H_{mos}(\omega, \theta_H, \varphi_H) = \left| \frac{\partial H_r(\omega, \theta_H, \varphi_H)}{\partial \varphi_H} \Delta \varphi_H \right| + \left| \frac{\partial H_r(\omega, \theta_H, \varphi_H)}{\partial \theta_H} \Delta \theta_H \right|, \quad (2.35)$$

where $\Delta \varphi_H$ and $\Delta \theta_H$ are average spreads of the easy axes *in-plane* and *out-of-plane*, respectively [84]. In order to find a model to describe a line broadening, it is necessary to have an extensive knowledge about the structure of the investigated material, so the information concerning inhomogeneous regions regarding composition, roughness, dislocation planes or grains can be taken into account.

2.5 Magnetic MAX phase films

MAX phases have been produced as thin films since 2002 [85] to assess its potential. Materials studied in this work were produced in the shape of thin films; thereby, the details about bulk synthesis of MAX phases are omitted, and the reader is referred to [17]. Well-established MAX phases thin film synthesis techniques include physical vapor deposition (PVD), chemical vapor deposition (CVD), and solid-state reaction [86]. Thermal spraying is mentioned as a complementary approach to synthesize MAX phase layers thicker than 100 μm as a coating.

The first successful synthesis of a magnetic MAX phase film was performed by the magnetron sputtering technique in the group of J. Rosén (Linköping University, Sweden). These experimental results on the $(\text{Cr}_{0.75}\text{Mn}_{0.25})_2\text{GeC}$ film were reported in 2013 [23]. The authors denoted this compound as a “self-organized atomic laminate” to emphasize its possibility to form perfect layers during the deposition from element targets.

The synthesis process was further optimized to produce new members of MAX phase films with long-range magnetic order [26, 34, 86, 87]. Competing phases of ternary and quaternary compounds are a challenge for the MAX phases stabilization. Prior to synthesis, ab-initio calculations based on density functional theory (DFT) were performed in order to find out potential competing phases with similar formation enthalpies [88, 89].

2.5.1 Film growth by magnetron sputtering

In order to grow heteroepitaxial MAX phase films with the basal planes oriented normal to the film plane, the hexagonal lattice of a substrate is required [89]. Beside hexagonal materials, a common choice is to use cubic structures with a (111) facet cut. For instance, the magnesium oxide MgO (111) facet with the lattice constant $a = 2.982 \text{ \AA}$ was successfully used for magnetic MAX phase growth [23]. It was used as the substrate for the synthesis of the MAX phases investigated in this thesis.

Physical properties of films depend on their microstructure. The phenomenological description of the film growth modes [90] takes into account an interplay between interface interactions, induced film strain and, importantly, energies on the substrate forming the film and its interface. The general classification identifies three growth modes, which are schematically presented in fig. 2.6 at early stages of the growth – an initial formation of the first monolayer and further development [91]. If the interaction between the substrate and the material is stronger than with the neighboring atoms and there is no lattice mismatch, a film has a two-dimensional growth, called Frank-van-der-Merve growth. The result is a smooth surface as the nucleation goes with monoatomic steps. On the other hand, with a weaker substrate-material interaction, the material atoms will adsorb onto one another, thus forming islands and

conglomerates, which is named Vollmer-Weber growth. In the intermediate case under the appearance of some strain, depending on the strength, films can grow in three dimensions in a mixed process, called Stranski-Krastanov growth mode [90]. In general, the epitaxial growth of MAX phases is similar to the step-flow growth, when the growth rate of basal planes is much higher than along the c-axis normal to basal planes [86].

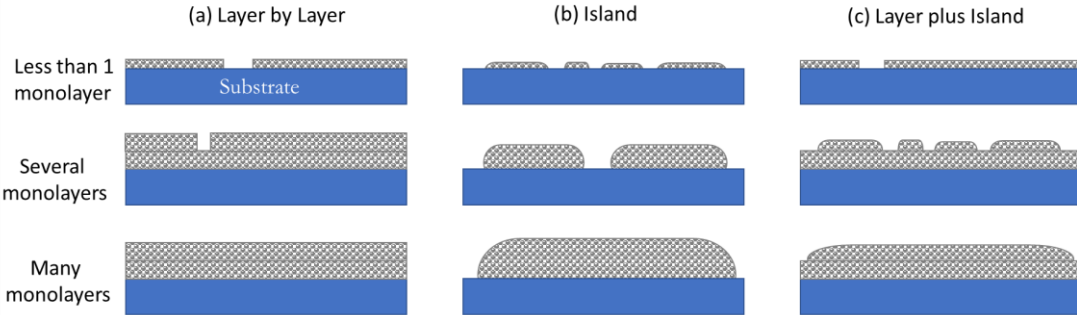


Figure 2.6 Common growth mechanisms of thin films. (a) Frank-van-der-Merve growth, (b) Vollmer-Weber growth, (c) Stranski-Krastanov growth. Redrawn from [90, 91].

The selected substrate for the heteroepitaxially growth of the films is generally made of another material and, thus, has a different lattice constant. A quantitative estimation for the lattice mismatch is commonly calculated as [90]

$$\frac{\Delta a}{a} = \frac{a_{substrate} - a_{film}}{a_{substrate}}, \quad (2.36)$$

where $a_{substrate}$ and a_{film} are unit cell parameters of the substrate and the film in the basal plane of the sample. These parameters are commonly extracted from X-ray diffraction (XRD) measurements.

The magnetron sputtering technique is one of the most prevalent methods of thin films synthesis with a high crystal quality [8]. In an ultra-high vacuum chamber targets with different materials are placed on magnetrons (fig. 2.7). The targets consist of a coating material in a solid form. The high quality of the film synthesis is persisted through the ultra-high vacuum conditions. The chamber is filled with a working gas, which can be argon, nitrogen or oxygen in a common operational mode. For the films investigated in this thesis, the argon was used during the deposition [24, 26].

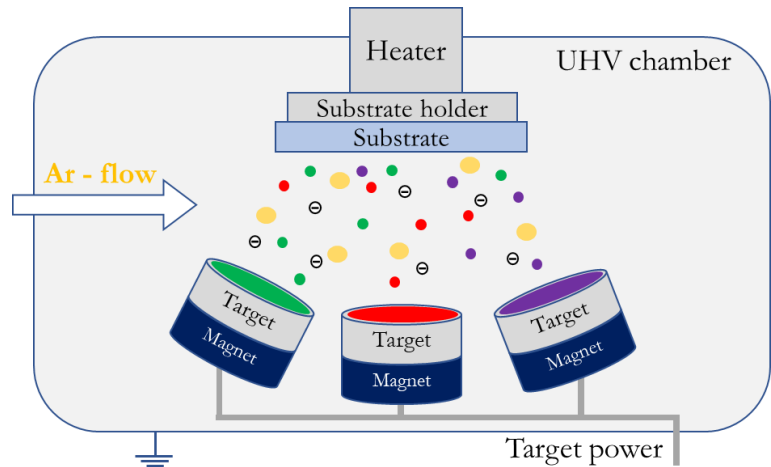


Figure 2.7 Schematically presented components of the magnetron sputtering setup. Targets with different material are shown in green, red and purple. The corresponding atoms shown as circles follow the same color code. Electrons are indicated as circles with a minus sign. The Ar gas flow is indicated by yellow dots. Redrawn from [14].

Briefly, the process can be described as follows: a negative electrical potential is applied to the magnetrons, acting as cathodes, while the ground reference is the anode. The electrical potential forces free electrons to speed up towards the anode to deprive working gas electrons by colliding with its atoms. Created positive charged ions with an energy of < 100 eV [8] accelerate then towards the magnetron and hit out atoms from the target. After, these hit-out atoms condense on a substrate specially placed above the magnetrons. The recombination of positively charged ions with free electrons continues until the desired thickness of a film is achieved. A typical energy of atoms during the magnetron sputtering ranges within few eV. By varying the gas pressure, it is possible to shift the energy distribution of atoms arriving to the substrate. A detailed description is given in the PhD thesis of A. Petruhins [14], who synthesized MAX phase films studied in this thesis.

2.5.2 Magnetic properties of related MAX phases

Magnetic order was observed in bulk and film MAX phases [33]. Resulting magnetic properties of the compound heavily depend on the choice of the *M*-, *A*-, and *X*-element as well as on the sample quality which can be characterized by phase purity, homogeneity and crystallinity [34].

A room-temperature FM response was observed for $(\text{Cr}_{0.75}\text{Mn}_{0.25})_2\text{GeC}$ film with Ge on the *A*-site [23]. $(\text{CrMn})_2\text{AlC}$ films with Al on the *A*-site showed a nearly temperature-independent FM order up to 280 K with the magnetic phase transition clearly above room temperature [28]. Polycrystalline CrGa-based MAX phases were synthesized with C or N on *X*-site: Cr_2GaC showed the temperature-dependent $\chi(T)$ of a Pauli paramagnet whereas Cr_2GaN exhibited a pronounced decrease of a $\chi(T)$ until a rise at the very low

temperatures near 0 K [92]. The suggested magnetic ground state for Cr_2GaN is a spin density wave with the transition at 170 K, which points on the presence of the two-dimension-like electronic structure [92].

In the following, an overview on magnetic properties of MAX phases that contain Cr, Mn, Ga and C elements will be given since they are related to compounds studied in this thesis. $(\text{Cr}_{0.7}\text{Mn}_{0.3})_2\text{GaC}$ demonstrated a complex temperature-dependent magnetization $M(T)$ with two magnetic phase transitions at 38 K and 153 K presumably originated from coexisting nanoscale Mn-rich and Mn-poor regions [29]. Polycrystalline CrMnGaC showed a weak ferrimagnetic component on the field-dependent magnetization $M(H)$ measured at 5 K and a PM response at higher temperatures with an effective magnetic moment μ_{eff} of 1.63 μ_{B} [93]. The calculated magnetic ground state for epitaxial Cr_2GaN films is an AFM configuration with 0.75 μ_{B}/Cr atom, where in each half-unit cell Cr magnetic moments reverse their orientation [25].

The first magnetic MAX phase with $n = 2$, $(\text{V, Mn})_3\text{GaC}_2$, showed a FM behavior between 100 and 300 K with a temperature-independent coercive field H_c of 0.035 T and a magnetic saturation at about 1 T [94]. A magnetic configuration of competing AFM and FM phases was suggested since a characteristic to magnetic MAX phases S-shaped $M(H)$ and a reduced remanent magnetization were observed [94].

Doping of Mn to the superconducting Mo_2GaC MAX phase resulted into a $(\text{Mo}_{0.5}\text{Mn}_{0.5})_2\text{GaC}$ film with a similar S-shaped $M(H)$ and a FM component visible up to 150 K [27, 95]. $M(T)$ showed a magnetic phase transition from an ordered magnetic state to a PM state with a transition temperature of about 220 K [95]. An in-plane easy axis of the magnetization was determined. For 3 K, H_c is 0.06 T, which is the largest reported for magnetic MAX phases up to date, and μ_{eff} of about $0.66 \pm 0.4 \mu_{\text{B}}$ [27, 95]. A magnetic order in $(\text{Mo}_{0.5}\text{Mn}_{0.5})_2\text{GaC}$ was described as a canted AFM spin configuration originated from the Mn-Mn exchange interaction similar to a proposed configuration for Mn_2GaC [40].

The resistivity for the $(\text{Mo}_{0.5}\text{Mn}_{0.5})_2\text{GaC}$ film demonstrated classical behavior of a metal with a slight deviation from linearity at 170 – 220 K explained by the magnetic phase transition [95]. The magnetoresistance is negative with a magnitude of 6 % at 5 K with the magnetic field of 9 T applied parallel to the film plane [95].

Temperature-dependent ferromagnetic resonance with an applied magnetic field parallel to the film plane showed a shift of the resonance field $\mu_0 H_r$ to lower values with decreasing temperature, while the opposite behavior was observed when a magnetic field was applied perpendicular to the film plane [95]. The magnetic relaxation rate is reduced with increasing temperature due to the observed decrease of the FMR linewidth ΔH [95]. A magnetocrystalline anisotropy (MCA) was determined to have an easy axis parallel to c -axis with a uniaxial MCA constant $K_{2\perp}$ of 4.5 kJ/m³ [95]. The temperature-dependent $K_{2\perp}$ obeys the Callen-Callen power law [76] with an exponent of 3.4 which is close to the expected value of 3 ascribed to a single-ion magnetic

anisotropy in uniaxial ferromagnets with the second-order term of the MCA [95]. Further, the density functional theory calculations showed that the MCA energy is strongly dependent on the *a*- and *c*-lattice parameters so that an easy axis switches from an in-plane to an out-of-plane orientation (parallel to the *c*-axis) characterized by a sign change [95]. The experimental MCA energy lies in this transition area and has a small positive magnitude which is in agreement with an observed soft magnetic properties [95]. An overall easy-plane magnetic anisotropy results from the dominant shape anisotropy contribution [95].

For the $(\text{Cr}_{0.5}\text{Mn}_{0.5})_2\text{GaC}$ films, a FM component was experimentally observed on $M(H)$ for $30 \text{ K} \leq T \leq 300 \text{ K}$. At 30 K, H_c is found to be 0.012 T and μ_{eff} is $0.067 \mu_{\text{B}}/\text{M-element}$; at 300 K, H_c is 0.008 mT and μ_{eff} is $0.019 \mu_{\text{B}}/\text{M-element}$ [26]. The transition temperature was defined to be higher than 300 K and the proposed magnetic configuration is a noncollinear long-range magnetic order, where AFM and FM interactions are competitive [26].

Temperature-dependent ferromagnetic resonance (FMR) measurements at 9.23 GHz showed a μ_0H_r increase with increasing T which is similar to an observed behavior for the $(\text{Mn}_{0.5}\text{Mn}_{0.5})_2\text{GaC}$ film [95]. μ_0H_r reached 0.33 T at about 250 K for an applied field both parallel and perpendicular to the film plane [96] and resides close to the resonance field calculated for the free electron with $g = 2.0023$. Therefore, the magnetic phase transition at about 205 – 230 K is proposed to be from a magnetically ordered state to a PM state [96]. ΔH_{pp} decreases from about 42 mT to about 26 mT with increasing T from 110 to 200 K with an observed peak of about 45 mT at about 225 K, which was ascribed to the critical fluctuations near the magnetic phase transition [96]. Angular-dependent FMR showed a negligibly small $K_{2\perp}$ and a *g*-factor of 2.00 was determined for both 300 and 110 K, which denotes that the orbital contribution to the magnetic moment of the compound is small [96]. It was concluded that the magnetic moments in the basal plane are ferromagnetically ordered while the coupling between the layers is dependent on the applied magnetic field orientation [96].

The Mn_2GaC compound synthesized as a film was extensively studied due to magneto-structural changes that result into an unconventional complex magnetic behavior [24, 40, 41, 97, 98]. A presence of a FM component was observed between 3 and 230 K with a nearly saturated $M(H)$ at 5 T. A magnetic transition to a proposed AFM state occurs at the vicinity of 230 K characterized by emerging field-induced transitions on $M(H)$ at about 2 T visible up to 300 K [40]. The critical order-disorder transition for this compound was predicted to take place at about 660 K [41]. Calculated ground states are FM and several AFM configurations, all are indistinguishable in energy which promotes its competition and, thus, a high sensitivity to the external stimuli like an applied magnetic field [40].

Modelled AFM configurations represent a predominant FM coupling in Mn-C-Mn slabs and a AFM-FM coupling of Mn atoms across Ga with a periodicity of 1- and 2-unit cells, the latter is shown to be closer to the experimentally observed XRD data [40].

According to calculations, the configuration of the magnetic moments affects the *c*-lattice parameter in a way that the interlayer distance of Mn-C-Mn is constant whereas Mn-Ga-Mn interlayer distance changes being smaller for a parallel alignment [40]. These anisotropic changes were experimentally confirmed by XRD measurements performed for two temperatures across the transition: at 150 and 300 K [40].

In order to describe the presence of a FM component at low *T*, a noncollinear magnetic configuration with a canting angle of the magnetic moments was proposed [40]. The total energy of canted moments simulated with a canting angle from 0° (AFM) to 90° (FM) deg. resulted in a possible energy minimum at a small canting angle below 12 degrees [40]. An observed increase of the total energy with a canting angle increase is in agreement with experimental magnetometry data since higher magnetic fields and temperatures are required to align the magnetic moments ferromagnetically [40]. The field-induced transitions on $M(H)$ above 230 K are assigned to metamagnetic transitions changing from noncollinear magnetic configuration to a canted AFM state [40]. Further studies by neutron reflectometry showed that the 2-unit cell periodic AFM configuration proposed in [40] is a suitable model to describe the magnetic configuration for Mn_2GaC film at 300 K [97]. In the same work, additional calculations revealed no energy difference between a FM alignment and a canted configuration of up to 7° [97] which supports the competing AFM/FM interactions in Mn_2GaC .

3 Experimental methods

Here, an overview of the experimental techniques used for the characterization of the investigated samples is provided. The chapter is divided into two parts describing structural and magnetic characterization methods.

3.1 Structural analysis

3.1.1 X-ray diffraction, X-ray reflectivity

X-ray diffraction (XRD) provides an information about structural phases of a material and its parameters. In this work, structural data were obtained by A. Petruhins using a Panalytical Empyrean Materials Research Diffractometer (MRD) with monochromatic Cu-K α X-ray radiation of $\lambda = 1.5419 \text{ \AA}$. MAX phases possess a hexagonal crystal lattice with unit vector lengths $a = b \neq c$ and angles between the unit vectors $\alpha = \beta = 90^\circ$ and $\gamma = 120^\circ$ [55]. Crystal lattice plane families are specified by Miller indices that are three integer numbers h, k, l [55].

X-rays are electromagnetic waves with a wavelength in the range of about 10 nm to 10 pm that is compatible to atomic distances [55]. When the set of planes with distances d_{hkl} is irradiated by X-rays with an angle θ , destructive or constructive interference occurs, depending on the angle of incidence. Geometrically, the incidence angle is equal to the scattering angle whilst propagating through the crystal. This principle is defined in the Bragg condition for a maximum constructive interference shown in fig. 3.1, which is valid for any lattice structure [99, 100]:

$$n\lambda = 2d_{hkl} \sin\theta, \quad (3.1)$$

where θ defines the scattering angle, d is the atomic spacing, n is the reflection order, and λ is the incident wavelength. The spacing between the family of (hkl) planes and its relation to the lattice parameters for the hexagonal crystal system are calculated as [100]:

$$\frac{1}{d_{hkl}^2} = \frac{4}{3a^2} (h^2 + hk + k^2) + \frac{l^2}{c^2}. \quad (3.2)$$

All studied films were measured in the standard Bragg-Brentano configuration, which is known as $\theta - 2\theta$ scan. In such geometry, only lattice planes oriented parallel to the basal film plane contribute to a Bragg reflection. For the MAX phase films with the layers perpendicular to the c -axis, observed XRD peaks correspond to $(000n)$ basal planes.

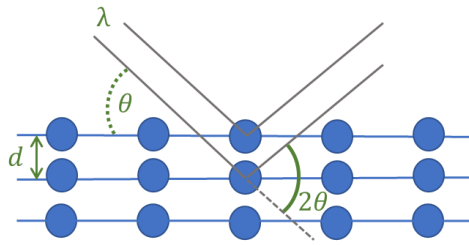


Figure 3.1 Representation of the Bragg's condition for a maximum constructive interference according to eq. 3.1.

X-ray reflectivity (XRR) was used to gain an information about density, thickness and roughness of the sample systems [101], which is schematically shown in fig. 3.2. The XRR data was obtained by A. Petruhins using a Panalytical Empyrean MRD. XRR is based on the total external reflection, so for the incident of electromagnetic waves the refractive index $n = 1 - \delta - i\beta$ of a material is almost 1, where δ is a parameter dependent on λ , density and composition of the specimen, and β is a coefficient related to an X-ray absorption [101].

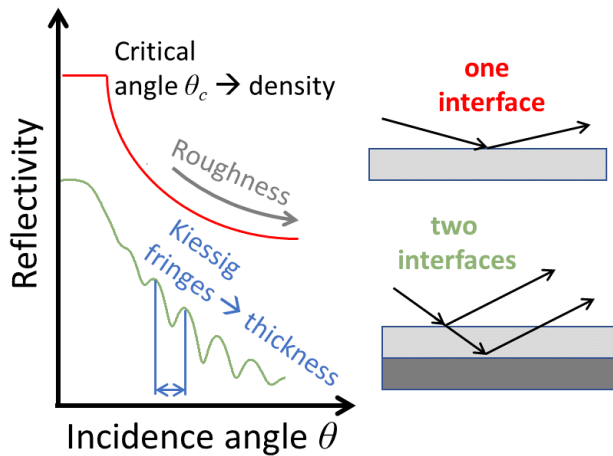


Figure 3.2 Information regarding the film specimen that X-ray reflectivity can provide. Red and green curves are arbitrary XRR profiles for one and two interfaces, respectively. Redrawn from [101].

Materials experience total reflection at a very small angle, when the incident angle on a surface does not exceed the critical angle for total reflection θ_c [101]. At this incidence angle all X-rays are reflected. From θ_c , one can obtain the density of the film [101]. If the film is sufficiently smooth, the resulting XRR curve contains oscillations – so-called Kiessig fringes [101]. By applying the Fourier transformation to the Kiessig fringes oscillation curve, the thickness of a measured single layer film can be obtained [101]. The film roughness r is determined from the decay of the amplitude as a function of angle: the larger the roughness, the more rapidly the amplitude decreases [101]. This analysis is commonly performed by a software implemented in the instrumental setup that allows to simulate a theoretical curve based on the desired layer model and

subsequently fits the experimental data until an optimal solution for thickness, density and roughness is achieved [101].

3.1.2 Scanning and transmission electron microscopy

Two experimental techniques were used in this thesis to perform a structural characterization of the studied samples. Scanning electron microscopy (SEM) provided an information about the surface morphology down to nm scale [102]. Transmission electron microscopy (TEM) study was made to examine the internal structure of the material down to atomic columns [103]. The following paragraph gives a brief introduction into the SEM technique along with the local and the element-specific analysis by the standard energy dispersive X-ray spectroscopy (EDX) and the basic principles of TEM imaging.

SEM results discussed in this thesis were obtained on the Zeiss LEO 1530 with the standard Schottky emitter module operating at the acceleration voltage of 5 – 20 kV. Using a focused electron beam with an energy range from 0.1 to 30 keV [102], it is possible to scan the surface and detect different types of electrons emitted from it. SEM is equipped with magnetic lenses used to focus and scan the electron beam onto the surface. A vacuum system is used to decrease collisions of electrons and increase the mean free path. The secondary electrons with energies up to 50 eV are generated from the primary beam due to inelastic interactions within the material. A secondary electron detector (SED) catches the secondary electrons that are coming from the sample [102]. By using the SED and the scanning method, the SEM image is created as the intensity of the secondary electrons at the position of the primary beam [102]. The SEM intensity information is colored as a grey-scale image. Different SEM intensity occurs due to the changes of the surface-normal towards the SED. Therefore, if the surface-normal points into the SED, the SEM intensity is high (white); in the case of perpendicular orientation of the surface-normal, the SEM intensity is low (black). Thus, the topography information of the scanned surface can be obtained as the variations in SEM intensity [102]. In the case of a porous structure, the imaging can be enhanced by tilting the specimen; a higher brightness appears on the pores' front-edges.

Besides secondary electrons, the interaction between the primary electron beam and the specimen generates characteristic X-rays and *bremsstrahlung* ("braking radiation"). Characteristic X-rays originate from the recombination of the electrons in the atomic shells after being excited by the primary electrons. Continuous *bremsstrahlung* appears due to the decelerated primary electrons in the material [102]. The local homogeneity analysis was performed with EDX [102, 104]. The experimental setup consists of a SEM combined with an EDX detector (Oxford Instruments MAX 80 mm²). This system features a position accuracy of the primary electron beam of better than 10 nm. All EDX data were taken at 10 or 20 kV with the energy resolution of 5 and 10 eV, respectively. The EDX detector identifies the energy of each individual X-ray

photon and summarizes the energy quantities into an energy-dependent spectrum. The Oxford Instruments software (INCA 4.14) was used to analyze this spectrum. It identifies all elemental peaks of the characteristic X-rays. INCA calculates the elemental contribution under the assumption of a homogeneous elements' distribution within the interaction volume (see below and Appendix A2). From each spectrum, the atomic percentage (at. %) of elements can be obtained. The analysis of EDX spectra contains an error of about 1 at. % of the material components. In addition, an operator has a possibility to choose elements of interest and generate a comparative spectrum under the assumption of a homogeneous element's distribution (Appendix A2).

The CASINO software [105] was used to simulate the penetration depth and the straggling effect of the primary electron beam in the specimen that represents a thin film on a bulk substrate (Appendix A2). It is based on a Monte Carlo simulation and calculates the interaction volume by visualizing the total distance travelled by the primary beam electron in the specimen. An area in the specimen, where the electrons travel, is usually denoted as the interaction volume [102].

In this thesis, transmission electron microscopy (TEM) data were obtained by M. Spasova on a JEOL JEM 2200FS [98] located at the Interdisciplinary Center for Analytics on the Nanoscale (ICAN) at the University of Duisburg-Essen. This model is equipped with GATAN UltraScan®1000XP CCD-camera, bright-field (BF) and annular dark-field (ADF) detectors, and SDD X-MaxN 80 TLE Oxford detector for an EDX analysis. It allows to perform studies in a scanning regime (STEM) with the resolution of down to 0.2 nm for a BF imaging and down to 0.1 nm for an ADF imaging at the acceleration voltage of 200 kV. TEM studies provide an information about the internal structure of the material down to single atom columns. A spatial resolution of 0.1 nm to 0.3 nm can be reached [103], which is in the dimension of atomic distances. It is possible to achieve such resolution due to the high acceleration voltage of 100 - 200 kV in standard and up to 3 MV in high-voltage electron microscopes [103]. The vacuum system is used in the same way as described for the SEM technique above. The electron beam is focused on the sample by using a multistage condenser lens system. This system creates parallel electron beams to homogeneously illuminate the sample. The electrons transmitted through the sample are focused onto a fluorescent screen by a lens system incorporating 3 to 8 lenses [103]. While the electrons transmit through the specimen, an elastic and inelastic scattering with the specimen atoms occur. Therefore, it is necessary to have a thin film of material of about 5 nm to 100 nm (100 keV electrons) for electrons to be able to penetrate the whole thickness of the sample [103]. For BF imaging, only the transmitted electron beam is observed by discarding scattered electron using the objective aperture. In contrast, in DF imaging scattered electrons are imaged, while the pure transmitted electron beam is discarded. Scattered electrons fulfilling the Bragg condition (see chapter 3.1.1) result in electron diffraction patterns [103] that are analyzed to study crystallinity, symmetry and lattice parameters.

Common techniques for the complex sample preparation are electropolishing and ion-beam etching [103].

Instead of illuminating the specimen area, the electron beam in a STEM mode focuses on a spot of up to 0.2 nm and then scans point-by-point over the specimen area [103]. This method allows to perform an EDX mapping or a Z-contrast ADF imaging simultaneously to imaging. The Z-contrast images are obtained by a high-angle ADF (HAADF) imaging that it is based on incoherently scattered electrons and provides an information about atomic number variations in the specimen [103]. Atoms with higher Z give a brighter contrast on a resulting image. This effect is related to stronger electrostatic interactions [103].

3.2 Magnetic characterization

3.2.1 Magnetometry

Temperature- and field-dependent magnetization studies were performed on the vibrating sample magnetometer (VSM) option of the Physical Property Measurement System (PPMS) from Quantum Design [106]. A PPMS is equipped with a superconducting magnet with a maximum magnetic field up to 9 T. The specimen is attached to the end of a rod that is connected to the vibrational unit. This unit vibrates with a fixed frequency and amplitude along the gradiometer pickup coil. During the measurement, the sample oscillates vertically with respect to the detection pickup coil (fig. 3.3) and induces a voltage, which is recorded then by the software [106]. The time-dependent induced voltage in a pickup coil is

$$V_{\text{pickup coil}} = \frac{d\Phi}{dt} = \left(\frac{d\Phi}{dz} \right) \left(\frac{dz}{dt} \right) \quad (3.3)$$

with the magnetic flux Φ , the vertical position z of the specimen with regard to the coil and time t [106]. The VSM option allows to measure the magnetic moment down to 10^{-9} Am^2 [106]. The detailed description of the components is given in the official manual for the setup [106].

For this thesis, measurements were performed at an applied magnetic field of $\pm 9 \text{ T}$. At temperatures below 350 K, the standard quartz half-rod from Quantum Design was used. Measurements from 300 to 850 K were carried out using the extended configuration of the setup with a heater connected to the sample rod [106]. The sample holder for the high temperature measurements is a ceramic sheet with an integrated heater and a temperature sensor at the sample area to provide local heating and temperature control.

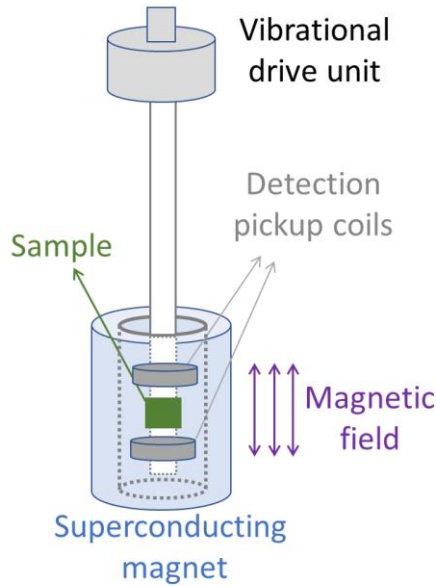


Figure 3.3 Schematic of the VSM option in the PPMS, adapted from [107]. The sample is fixed on a rod that is connected to the vibrational drive unit. The sample moves through the detection coils.

Complementary temperature- and field-dependent magnetization studies were performed on a Superconducting Quantum Interference Device (SQUID) implemented in the commercial setup MPMS-XL from Quantum Design [108]. A MPMS-XL equipped with a superconducting magnet with a maximum magnetic field of ± 5 T allows to perform measurements in the temperature range of $5 \leq T \leq 400$ K.

During the measurement, the specimen moves through a second-order gradiometer superconducting detection coil system which is coupled to the SQUID sensor [108]. As the SQUID sensor is enclosed with the detection coils, a magnetic flux produces a proportional change in the persistent current. Since SQUID acts as a current/voltage convertor, a change in an induced voltage is proportional to the magnetic moment of the specimen. A typical induced voltage from the specimen with respect to coils is shown in fig. 3.4. This response is achieved when the sample is smaller than detection coils and is uniformly magnetized. For detailed information, the reader is referred to [107, 108].

The sample was mounted onto a paper stripe longer than the scan length to eliminate the signal change during the measurement. The standard clear drinking straw was used as a sample holder. The measured magnetic moment was divided by the film volume or by the substrate volume to obtain the volume magnetization. The specimen volume was determined from the thickness derived from XRR and the sample area estimated from an image of the sample.

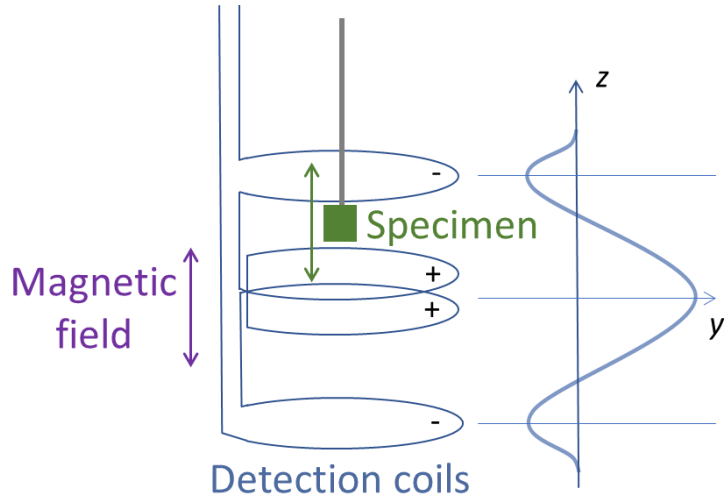


Figure 3.4 MPMS-XL detection coils configuration with respect to the specimen, which is attached to a straw-holder. On the right side, an induced voltage of the specimen that moves through the gradiometer detection system. The z -axis defines the specimen's position and the y -axis shows an output voltage. Adapted from [107].

3.2.2 Magnetoresistance

Electrical resistivity measurements were performed in a Physical Property Measurement System (PPMS) from Quantum Design at $4 \text{ K} \leq T \leq 350 \text{ K}$. A standard 4-probe geometry method was used [71]: 4 gold-coated pin contacts were attached to the specimen surface. Currents up to 10 mA were driven via the two outer pins through the specimen whilst measuring a voltage drop across the inner pins (fig. 3.5) [71]. In order to achieve an undisturbed distribution of electrical field lines, the pin contacts should be positioned much closer to each other than to the lateral dimensions of the sample to avoid edge contributions. By using this measurement geometry, the influence of contacts and wiring can be kept minimal [71]. In the case when the film thickness is much smaller than the distances between the probes $d \ll s_n$, the film can be approximated as an infinite 2D sheet. In this model, the current is assumed to flow over the surface without going into the film depth. The electrical resistivity ρ_{2D}^{4p} for the case of the equidistant probes location is [71]

$$V = \frac{I \rho}{2\pi d} \times \ln \left(\frac{s_2 s_3}{s_1 s_4} \right) \quad \Rightarrow \quad \rho_{2D}^{4p} = \frac{\pi d}{\ln 2} \times \frac{V}{I}, \quad (3.4)$$

where V is the voltage drop between the inner probes, I is the current, d is the film thickness, and s_n is the distance between the probes (fig. 3.5) [71]. Further, the sheet resistance R_{sheet} as an approximation for a homogeneous and finitely thick specimen is calculated [71]

$$R_{sheet} = \frac{\rho}{d} = \frac{\pi}{\ln 2} \times \frac{V}{I} \quad (3.5)$$

It implies that for 2D-like objects such as thin films, R_{sheet} appears to be independent on the distance between the probes.

The measurements were performed by U. Wiedwald in an external magnetic field applied parallel to the current direction and to the film plane [98]. The temperature change was fixed at 2 K/min, the magnetic field was swept with the speed of 0.01 T/s.

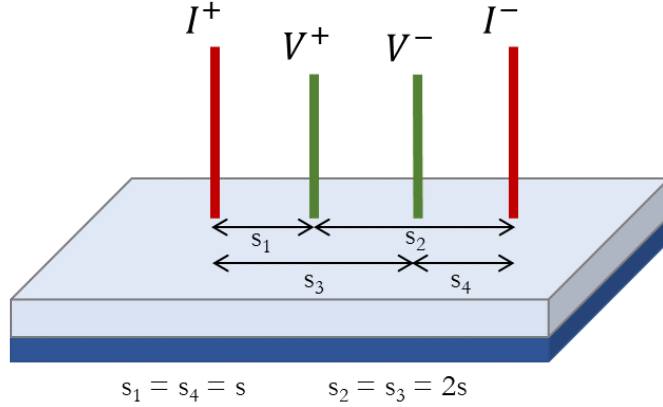


Figure 3.5 Experimental configuration for electrical resistivity measurements using a standard 4-probe geometry. I and V indicate current and voltage, respectively. + and - specify their directions. The values s_x define the spacing between the probes. Adapted from [71].

3.2.3 Ferromagnetic resonance

Microwave resonator setup

Angular and temperature-dependent FMR studies were conducted on a commercial Bruker Elexsys E500 spectrometer with the cylindrical mode Bruker cavity model ST9246 [109]. The core components of the experimental setup include a microwave resonant cavity, a microwave bridge, an electromagnet and a signal processing system (fig. 3.6). The specimen is placed inside of a resonant cavity fixed on a glass rod that serves as a holder. A rod can be attached to the goniometer to be able to rotate the specimen in a magnetic field applied at specific specimen positions such as out-of-plane and in-plane in the case of a film shape.

For the measurements in this work, an X-band bridge was used that generates microwave radiation in the narrow frequency range of about 9.5 ± 0.5 GHz and includes a Schottky barrier diode as the detector for microwave radiation being reflected from the sample in case of magnetic resonance [109]. The generated linearly polarized microwaves are guided by a circulator through a waveguide system into the resonant cavity where they interact with the specimen. A part of the microwave radiation is directed to a reference arm before the circulator. By that the integrated detector gets the microwave power needed for the operation in a linear regime. The overlaying microwave radiation at the detector coming from the reference arm and the specimen are phase matched by a phase shifter built into the reference arm. An

important parameter of resonant cavities is the quality factor Q , which is defined as [109]

$$Q = \frac{f_{res}}{\Delta f}, \quad (3.6)$$

where f_{res} is the cavity eigenfrequency and Δf is the resonance width at half height. Q characterizes the stored energy in the cavity with respect to the energy dissipated from the cavity per one microwave period [109]. Massive samples often exhibit non-resonant absorption of the microwaves via electric fields. This effect may cause a Q decrease as the dissipated amount of energy increases [109].

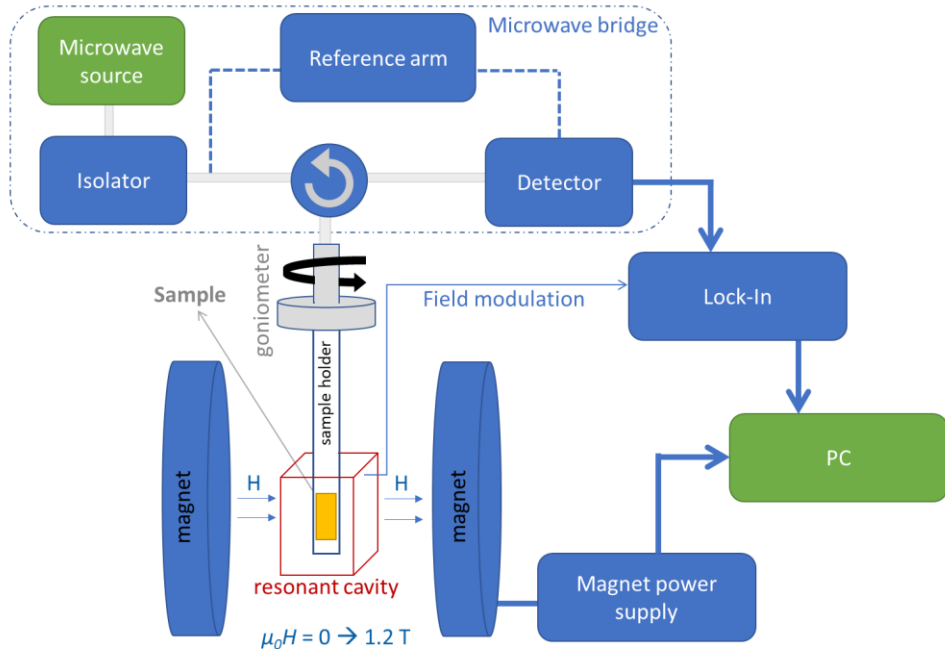


Figure 3.6 Schematic of the experimental setup for the angular- and temperature-dependent ferromagnetic resonance studies based on a resonant cavity. Frequency range can be extended by complementary microwave bridges besides a standard X-band bridge.

The detection scheme uses the resonance of the cavity to detect the FM or PM resonance of the specimen. The microwave frequency is adjusted to match the eigenfrequency of the cavity with the specimen in the way that no microwaves are reflected out of the cavity. A standing wave is generated inside of the cavity, which implies that the electric and magnetic field components of the microwave are out of phase. The specimen should be placed at the position where the magnetic component of the microwave is maximal. This location depends on the cavity geometry, for a cylindrical TE₀₁₁ mode cavity the maximum of the magnetic microwave component is in the central part [110]. The microwaves couple to the cavity through an iris which is a hole in the cavity. By changing the size of this iris with a coupling iris-screw, the incoming and reflected microwave quantity is controlled by matching the impedance

of the cavity and the waveguide [109]. An impedance is defined as a resistance to the waves. Therefore, when the specimen resonantly absorbs the microwave power, the cavity loses its coupling and the microwaves are reflected back to the detector which results in a signal. An automatic frequency control (AFC) built into the spectrometer adjusts the microwave frequency to match the shifted cavity eigenfrequency which occur at resonance absorption. The detected signal is processed by a Lock-in amplifier using a field-modulation f (100 kHz in this work) as the reference f . The field modulation is calibrated by the standard sample – a strong pitch containing 0.11 % of KCl [109].

Angular and temperature-dependent FMR studies were conducted at the temperature range $100 \text{ K} \leq T \leq 650 \text{ K}$ and a magnetic field up to 1.5 T. The sample was mounted onto a glass rod by a double-sided adhesive tape and fixed inside a goniometer. The goniometer with a computer-controlled stepper motor allows to conduct angular studies with a resolution of 0.125° . The rotation of the sample was performed in in-plane or out-of-plane orientation. For the temperature stabilization, the cooling insert was used in addition to the standard experimental configuration. It includes the liquid nitrogen gas-flow transfer system to cool down the specimen area by applying a nitrogen gas flow and a heater element positioned under the resonant cavity. The temperature is set by a controller that adjusts the gas flow and the operation of the heater element. This combination ensures the effective temperature variation. The cavity was loaded with the vacuum glass tube to secure the temperature stabilization around the sample area. The heater is installed below the sample in the vacuum glass tube. The same cooling insert was used for the measurements up to 650 K with an additional modification regarding the nitrogen flow which is dominant in this configuration in order to achieve high temperatures.

Microwave short setup

Frequency dependencies for the Mn_2GaC film were measured on a noncommercial setup engineered as a part of M. Riebsch Master's thesis [111]. The core components are schematically presented in fig. 3.7. A superconducting magnet is located inside of a liquid helium bath and a gas-flow cryostat. The microwaves generated in the synthesizer are carried through the coaxial cable that is used instead of a conventional resonator cavity. The magnet allows a bidirectional sweep of the field up to $\pm 12 \text{ T}$ and the temperature variation of $100 \text{ K} \leq T \leq 300 \text{ K}$.

A resonant microwave absorption is realized by a short-circuited semi-rigid coaxial cable used to guide the microwaves to the specimen area (fig. 3.8). Microwaves generated propagate to the short-circuited end of the semi-rigid coaxial cable, where the specimen is mounted. At this position, the sample is penetrated by an alternating high frequency magnetic field due to the microwave near field effect [111]. For the signal optimization, a slide screw tuner was used to maximize the microwave absorption in the specimen. For the detection of the reflected microwave power at

resonance, a Schottky diode was used in connection with a Lock-in amplifier. A temperature sensor was mounted onto the sample holder, a complementary temperature sensor was mounted in the close vicinity of the specimen and the heater to display the temperature gradient in the chamber and, thus, ensure a precise control of the temperature stabilization. For further details, the reader is referred to [111].

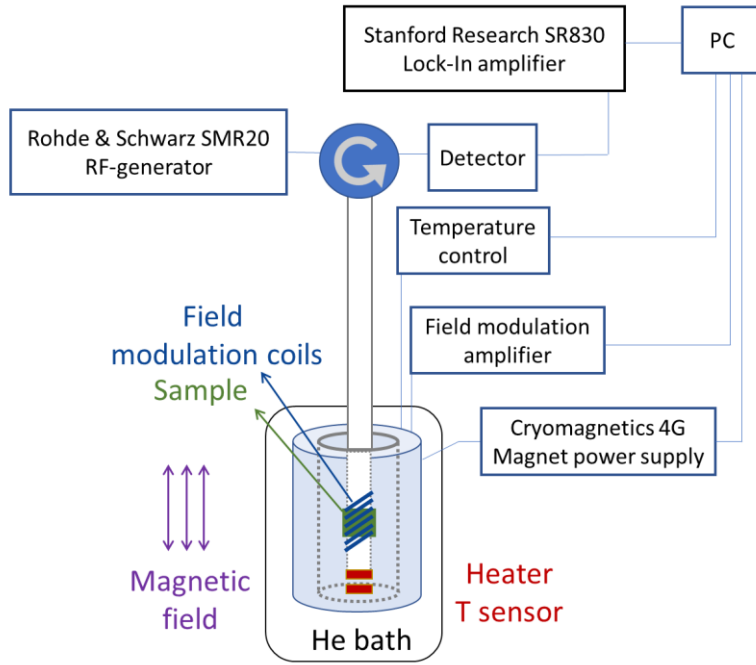


Figure 3.7 Schematic of the experimental setup for the frequency- and temperature-dependent ferromagnetic resonance detection. Adapted from [111].

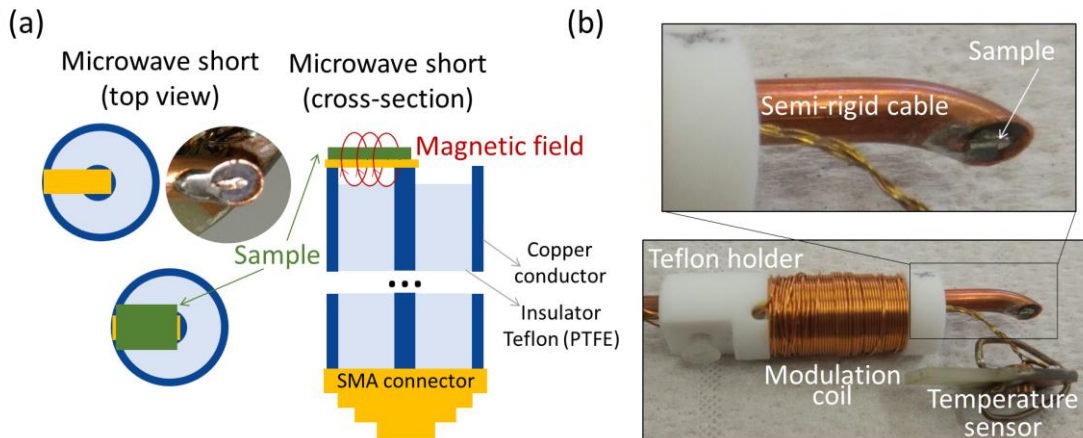


Figure 3.8 (a) Sample (green) mounted on the short-circuited end of the semi-rigid coaxial cable (yellow). An alternating magnetic field (red) is induced by the microwave near-field effect from the microwave short at the specimen area. (b) The semi-rigid cable with the microwave short and the mounted specimen. On the Teflon holder, the modulation coil is visible as well as the holder for the temperature sensor. Adapted from [111, 112].

Data processing

In FMR experiments, a FM material experiences a resonant absorption of an electromagnetic radiation at specific frequency [60]. A theoretical description of FMR is given in chapter 2.4.

A typical FMR spectrum of Mn_2GaC on MgO measured at 110 K with the magnetic field applied parallel to the film plane is shown in fig. 3.9. The blue-colored part describes the FMR signal at low magnetic field and the background contribution. Generally, a background is linear at high fields as it is presented in fig. 3.9 by the black dashed line. The subtraction is performed by a linear function applied to the data set. If the electric field distribution of the measuring cavity is disturbed by the sample, a background contribution can show an angular dependence. The origin of this effect has a complex multiparameter nature and is related mainly to an electric field distortion via an impedance imbalance during the rotation of the massive sample or to a temperature destabilization during the measurement. The red part indicates multiple sharp resonances attributed to the PM inclusions in MgO , which were earlier observed in [113]. $\mu_0 H_r$ was obtained from the position, where the resonance line crosses zero on the y -axis after a background subtraction.

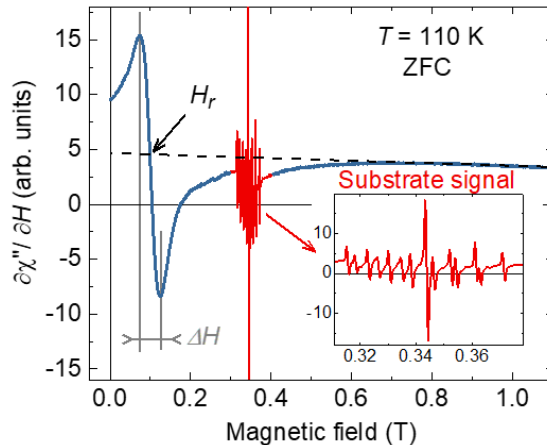


Figure 3.9 Ferromagnetic resonance signal measured at 110 K for the zero-field-cooled (ZFC) Mn_2GaC film. The resonance field H_r and linewidth ΔH are marked. The red-colored part of the signal (magnified in the inset) displays multiple sharp resonances that originate from inclusions incorporated in the MgO substrate. The black dashed line indicates the linear background contribution.

For many samples, a symmetric FMR lineshape of the microwave absorption can be described by a Lorentz distribution [60]. On another hand, FMR signals could carry certain asymmetries depending on the individual characteristics of a magnetic system. For instance, a non-uniform penetration of the microwave field could lead to induced eddy currents in the specimen [114]. If the magnetic system experiences a small damping, a FMR lineshape can be described by a Lorentzian function [115]. In order to account for an asymmetry of FMR line, the solution combining the sum of symmetric and asymmetric Lorentzian lineshapes was obtained in [114, 115]:

$$f(x) = a \frac{1+\beta(H_r-H_0)/\Delta H}{(H_r-H_0)^2+(\Delta H/2)^2}, \quad (3.7)$$

where H_r is the resonance field, a is the scale parameter and the asymmetry of the signal is defined with the parameter β . This function was used to extract the linewidth ΔH of an FMR line.

Magnetic anisotropy constants and a g -factor were obtained by fitting an angular-dependent resonance field H_r extracted from FMR measurements. The fit is based on the Smit-Beljers approach that contains the free energy density as a fit model corresponding to the sample system (chapter 2.4, eq. 2.28). The free energy should contain the energy contributions that are anticipated for the investigated material according to its magnetic properties and crystal structure. Major contributions are given in chapter 2.4 and in more details in [46, 73]. An external magnetic field $\mu_0 H$ is included in the Zeeman free energy density contribution. An angular-dependent magnetization M was implemented by an angular-dependent factor to M with respect to azimuthal and polar M angles (fig. 2.5). Additionally, an effective canting angle for M was introduced as a parameter for fit. A script for the fit operations was developed by B. Zingsem using the Mathematica software by Wolfram Research [115]. A fit was performed for the material-specific parameters that can be inserted into the code as a fixed value or as a variable, e. g. measuring frequency f , saturation magnetization M_s , uniaxial anisotropy constant K_2 or g -factor. The first iteration of the fit operation minimizes the free energy density for a given start field value H_r . With the M direction obtained from the first iteration, the corresponding H_r is calculated for a selected resonance frequency by solving the resonance condition. Then this calculated H_r is compared to the starting H_r , and, when these values do not match, the calculated H_r is selected to perform the next iteration. This method is combined with an interpolation method, calculating the resonance field for a chosen frequency by doing an interpolation of the resonance field to a position between the two next neighboring resonances. These procedures are repeated by the program code till the best match between an experiment and corresponding fit is achieved.

4 Results and discussion

4.1 $(\text{Cr}_{0.5}\text{Mn}_{0.5})_2\text{GaC}$ films

Magnetic MAX phase $(\text{Cr}_{0.5}\text{Mn}_{0.5})_2\text{GaC}$ films with thicknesses of 12.5, 20.8, 40.3 and 156 nm were studied as a function of an external magnetic field and temperature. The synthesis, XRD and XRR analysis were performed by the group of Prof. J. Rosén (Linköping University, Sweden) [26]. Data from SEM, magnetometry and FMR investigations presented in this thesis were partially published in [116].

4.1.1 Structural characterization and homogeneity

$(\text{Cr}_{0.5}\text{Mn}_{0.5})_2\text{GaC}$ films were epitaxially grown on MgO (111) substrates by magnetron sputtering with nominal thicknesses of 160, 40, 20 and 10 nm. A high crystal quality was achieved by the deposition at elevated $T = 823$ K. Thicknesses determined by the growth rate and the deposition time slightly differ from thicknesses obtained by the XRR analysis. In the following, the measured thicknesses will be used (table 4.1).

X-ray diffractograms are presented in fig. 4.1 and show the Bragg peaks of the $(\text{Cr}_{0.5}\text{Mn}_{0.5})_2\text{GaC}$ (000*l*) basal planes with no clear traces of side phases; the peaks (logarithmic scale) correspond to a pure MAX phase confirming a high crystalline quality of the samples. A MgO (111) reflection has been observed for all samples [26]. The reflections for 12.5 and 20.8 nm films (figs. 4.1(a) - (b)) have the lowest intensities due to the smaller amount of material.

The (0006) diffraction peaks of the $(\text{Cr}_{0.5}\text{Mn}_{0.5})_2\text{GaC}$ phase identified for both films indicate a similar quality as for the thicker films. Figs. 4.1(c) - (d) show the diffractograms for 40.3 and 156 nm films. The Bragg peaks originated from the MAX phase basal planes (000*l*) of order $l = 2$ up to $l = 8$ can be clearly identified. To gain more information on the film quality at the micro- and nanoscale, high-resolution TEM studies were performed [26]. These studies reveal homogeneous epitaxial films within the entire thickness with the *c*-axis perpendicular to the film plane and a lateral granular size above 150 nm. Uninterrupted basal planes with the MAX phase laminated structure show the high crystalline quality of the films.

A further analysis of the XRD data includes a detailed look at the most intensive peak (0006) at the angle of 43.6 deg. (fig. 4.2). The (0006) Bragg peak position of all samples is the same, indicating no lattice strain in (000*l*) direction within the error bar of 10^{-4} nm [116]. On another hand, a lattice strain could be expected due to 2.8 % *a*-lattice mismatch between $(\text{Cr}_{0.5}\text{Mn}_{0.5})_2\text{GaC}$ and MgO [26], since the basal plane tensile strain could lead to a coherent *c*-axis lattice strain. In a 570 nm film of the same compound, the *c*-axis lattice constant is found to be about 0.095 % smaller than the one of the 34 nm film [26]. It suggests that the *c*-lattice relaxation may occur at film thicknesses larger than 570 nm. The in-plane *a*-lattice parameter, however, remains unchanged for all thicknesses [26].

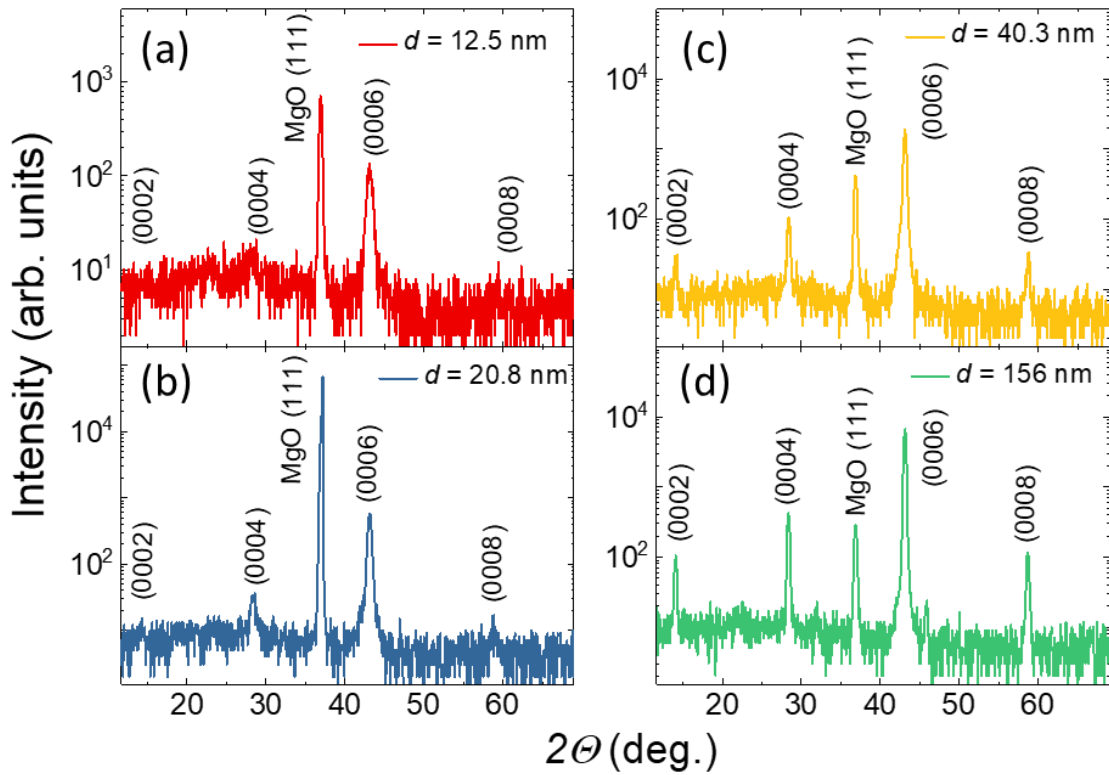


Figure 4.1 $\theta - 2\theta$ X-ray diffraction scan of the $(\text{Cr}_{0.5}\text{Mn}_{0.5})_2\text{GaC}$ films for (a) 12.5 nm, (b) 20.8 nm, (c) 40.3 nm, and (d) 156 nm. (111) reflections originate from the MgO substrate. Adapted from [116].

An absence of peaks coming from side phases (fig. 4.1) confirms the phase purity of the $(\text{Cr}_{0.5}\text{Mn}_{0.5})_2\text{GaC}$ films. Nevertheless, a peak at about 45.8 deg. for 156 nm film can be seen (indicated by violet asterisk in fig. 4.2). It can be associated with: (a) an appearance of tilted grains with increasing thickness, (b) a minor amount (less than 0.1 %) of cubic Cr_4Ga (220) [116].

One possibility to identify different magnetic phases is to perform magnetic resonance spectroscopy, the results will be shown in chapter 4.1.3. This method is sensitive to FM or PM phases and impurities which would manifest themselves as additional signals within the available magnetic field range. No additional magnetic resonance signals were observed in the fields up to 1.2 T except the main resonance from the Mn_2GaC film (fig. 4.12). Thus, it is inferred that if impurities are present in the $(\text{Cr}_{0.5}\text{Mn}_{0.5})_2\text{GaC}$ MAX phase films, they are negligibly small and do not carry a considerable magnetic signal.

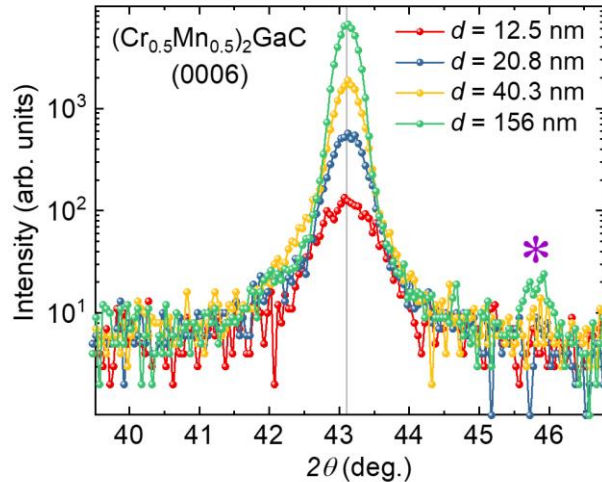


Figure 4.2 Comparison of the (0006) peak position for the 12.5 nm, 20.8 nm, 40.3 nm and 156 nm $(\text{Cr}_{0.5}\text{Mn}_{0.5})_2\text{GaC}$ films. The violet asterisk marks peaks that may originate from tilted grains or from a trace amount of Cr_4Ga [116].

X-ray reflectivity (XRR) scans are presented in fig. 4.3. The Panalytical X'pert Reflectivity v1.3 profile fitting routine was used to fit the experimental data within the framework of a standard single layer model [26, 116]. From the fit, thickness d , density ρ and roughness r were extracted. The results are summarized in table 4.1.

The critical angle θ_c defines an angular position where a sharp decrease of the XRR curve appears, typically shortly before Kiessig fringes [101]. In general, θ_c becomes larger with increasing ρ according to the relation $\theta_c \propto \sqrt{\rho}$ [101]. θ_c was found to be slightly smaller for the 12.5 nm film and nearly the same for the 20.8 – 40.3 nm films. For 20.8 - 156 nm films, we obtain $\rho = 6.4 \pm 0.3 \text{ g/cm}^3$, whereas a fit for the thinnest 12.5 nm film was possible to perform only by assuming about a $20 \pm 2 \%$ reduction of the mass density so the resulting ρ is $5.1 \pm 0.3 \text{ g/cm}^3$ [116].

XRR profiles for 12.5, 20.8 and 40.3 nm films are presented in fig. 4.3. No Kiessig fringes were observed for 156 nm film. Kiessig fringes are the oscillations caused by the X-ray interference between the film surface and the surface-film interface. The period of the fringes is used for the film thickness determination. The distance between the two maxima/minima $\Delta\theta_i$ is proportional to $\lambda/2d$ [101]. The origin of this effect can be related to an instrumental limitation related to the ability to differentiate scattered X-rays, which are getting closer with increasing thickness combined with the low X-ray intensity. It could be as well a sign of a larger roughness at higher thicknesses, assuming a step-flow growth mode with a heterogeneous nucleation [86].

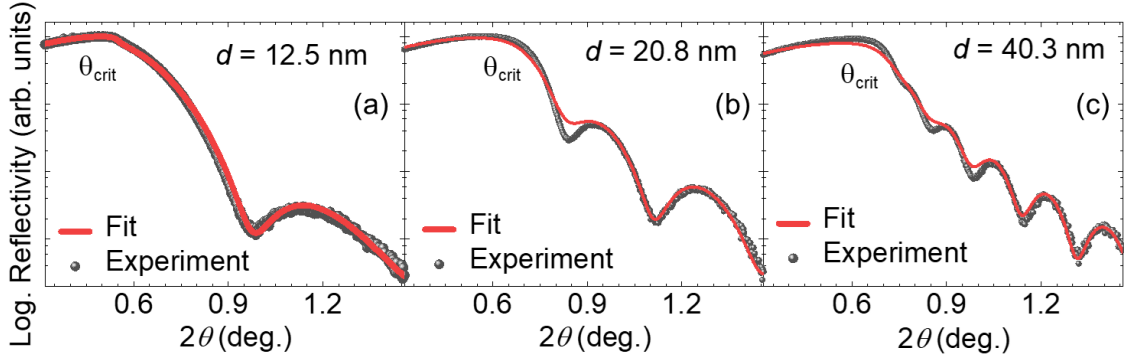


Figure 4.3 X-ray reflectivity profiles and corresponding fits for the (a) 12.5 nm, (b) 20.8 nm, and (c) 40.3 nm $(\text{Cr}_{0.5}\text{Mn}_{0.5})_2\text{GaC}$ films. Adapted from [116].

For the $(\text{Cr}_{0.5}\text{Mn}_{0.5})_2\text{GaC}$ films, the roughness derived from XRR simulations is similar for all films and is about 2.2 nm within the error bar (table 4.1). As the films exhibit the *c*-lattice parameter of 1.258 nm, it implies that the surface roughness is about 2-unit cells. Simulations for different materials show that, in general, fringes are significantly suppressed when the roughness is larger than 2 nm [101].

Table 4.1 Results of XRR measurements for $(\text{Cr}_{0.5}\text{Mn}_{0.5})_2\text{GaC}$ series. The nominal thickness is given besides the parameters obtained from the XRR fit: thickness d , density ρ and roughness r [116].

d (nominal), nm	d (XRR), nm	ρ , g/cm ³	r , nm
160	156	6.4	2.3
40	40.3	6.6	2.2
20	20.8	6.3	2.0
10	12.5	5.1	2.4

SEM images of 12.5 nm, 20.8 nm, 40.3 nm and 156 nm films were recorded to study the surface morphology (fig. 4.4). The SEM contrast from a film surface is usually attributed to a) materials/phases with different electron densities or b) a distance variation to the detector and, thus, qualitatively different height. For all thicknesses, smooth films are found confirming the XRR roughness results. Darker contrasts are ascribed to void areas which decrease with increasing film thickness as grains also grow laterally at higher thicknesses. It is unlikely that there is a second phase since with this gradual increase of the darker areas, additional peaks in XRD should be detected as a function of thickness, which is not the case (fig. 4.1). This observation shows that these films exhibit a heterogeneous nucleation growth process, which leads to the formation of almost continuous layers for films thicker than 12.5 nm.

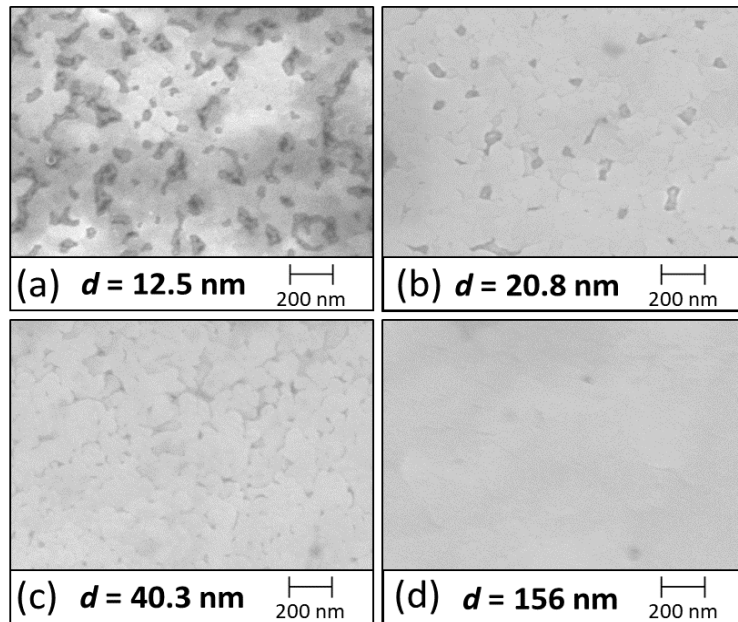


Figure 4.4 Scanning electron microscopy images of a surface for the (a) 12.5 nm, (b) 20.8 nm, (c) 40.3 nm, and (d) 156 nm $(\text{Cr}_{0.5}\text{Mn}_{0.5})_2\text{GaC}$ films. Data adapted from [116].

In order to clarify the nature of the darker areas, SEM imaging of the 20.8 nm film tilted by 60° has been performed using an InLens detector, which is presented in figs. 4.5(a) - (b). The tilted geometry reveals the darker areas with a brighter “ring” on the one side and more blurry edge on the other side. Such observation confirms a porous structure of the specimen. The pores do not exceed the size of 100 nm and are homogeneously distributed over the surface vanishing with increasing thickness. In contrast, SEM investigation of the 20 nm $(\text{CrMn})_2\text{AlC}$ MAX phase film on a Al_2O_3 substrate deposited by pulsed cathodic arc revealed islands on the micrometer scale with a substrate coverage of around 72 % [28].

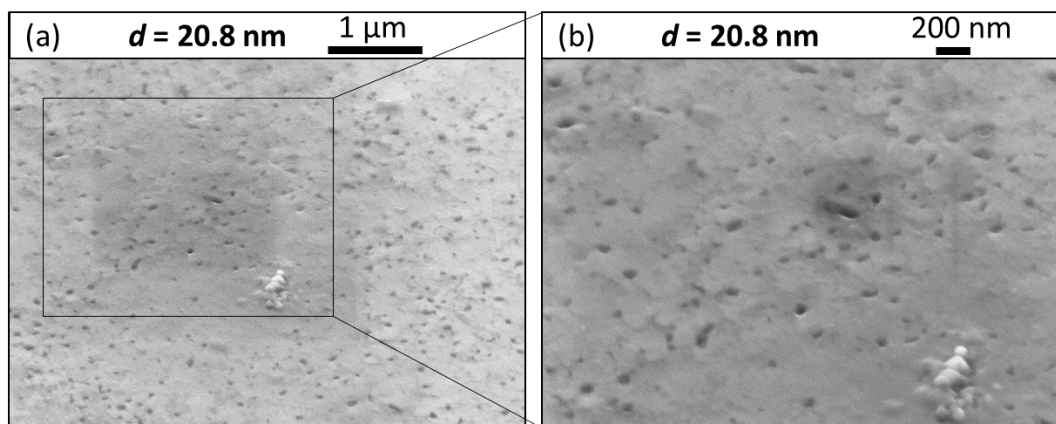


Figure 4.5 Scanning electron microscopy image for the 20.8 nm $(\text{Cr}_{0.5}\text{Mn}_{0.5})_2\text{GaC}$ film tilted by 60° .

The difference in contrast between pores and covered material is useful to determine the area which is covered by pores. Parts of fig. 4.4(a) were analyzed using the ImageJ software [117]. The “Analyze Particles” tool was used to evaluate the pores fraction. Prior to analysis, image fragments were converted into binary images with black and white colors, a contrast enhancement of 3 % was applied to improve the identification of pores. A threshold adjustment was performed to visualize the pores’ contour. Size and shape of objects of interest were parametrized to be able to identify complex patterns as the observed pores do not exhibit simple spherical/quadratic shape [118]. Image fragments and overlaying masks are presented in fig. 4.6(a) - (c) and (d) - (f), respectively. For the 12.5 nm film, pores constitute an area of $20 \pm 5 \%$ (painted red in figs. 4.6(a) – (d)). This observation is in agreement with an effective density reduction found from XRR analysis (table 4.1). Thicker films were not analyzed due to more homogeneous surface morphologies.

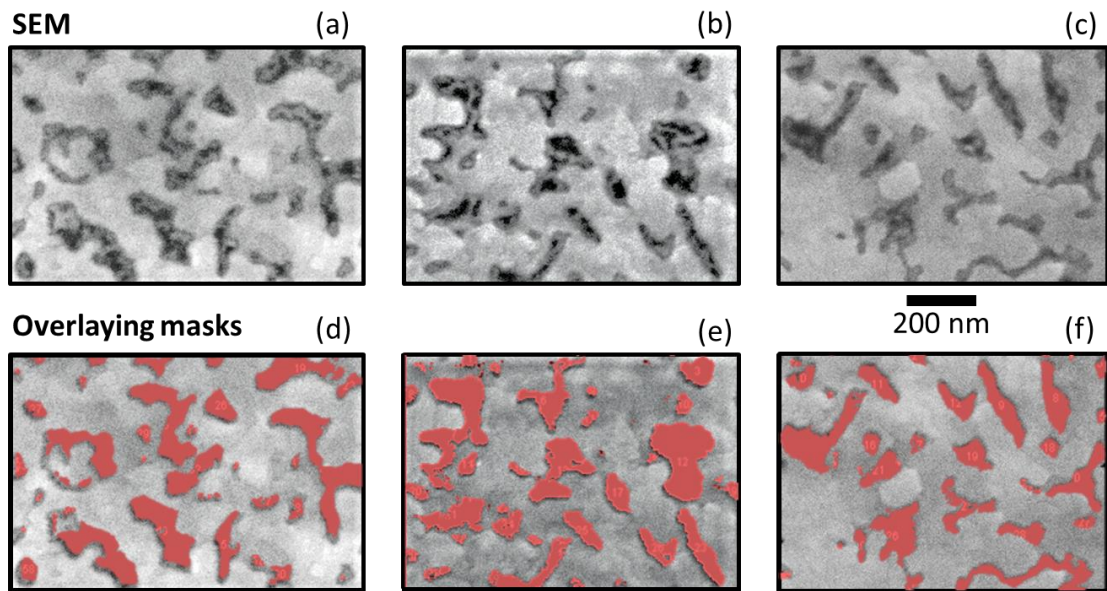


Figure 4.6 (a)-(c) Scanning electron microscopy images for the 12.5 nm $(\text{Cr}_{0.5}\text{Mn}_{0.5})_2\text{GaC}$ film’s surface and (d)-(f) respective overlaying masks (red) that identify a pores’ area obtained using ImageJ [117, 119].

An electron dispersive X-ray spectroscopy (EDX) was used to investigate the local composition of the 12.5 and 156 nm films (see in Appendix A2). The films are found to be homogeneous. The local composition varies by less than 2 at. % over the whole film. The thickness of 20.8 nm appears to be the lowest limit for a continuous film-growth of $(\text{Cr}_{0.5}\text{Mn}_{0.5})_2\text{GaC}$ [116], as it was shown in fig. 4.4. Bright spots close to the center part of the image in fig. 4.5(a) are clusters on the sample’s surface that formed during the film deposition. Ga-Mn clusters were observed on the surface of both 12.5 and 156 nm films (see Appendix A2). The origin of these clusters is unclear. Its presence could be attributed to the sample preparation which includes high temperatures of 823 K and, thus, may cause clustering.

4.1.2 Magnetic phase transition as a function of temperature

Cr or Mn containing alloys can show competing AFM and FM interactions leading to the frustration of magnetic moments resulting in a spin-glass-like behavior [120, 121]. The temperature-dependent magnetization $M(T)$ can provide information on such frustration effects by cooling the sample through the transition temperature under zero-field (Zero-field-cooled: ZFC) and subsequently measuring it with increasing temperature under a small magnetic-field followed by the measurement in the same field with decreasing temperature (field-cooled: FC).

The presence of these frustration effects in 156 nm and 20.8 nm $(\text{Cr}_{0.5}\text{Mn}_{0.5})_2\text{GaC}$ films can be seen in the splitting between the ZFC- and FC- $M(T)$ curves [121] measured in a magnetic field of $\mu_0 H = 0.02$ T applied parallel to the film plane (fig. 4.7). This splitting can be characterized by a freezing temperature T_f . The defined T_f is 160 ± 7 K for the 156 nm film and is qualitatively below 160 K for the 20.8 nm film, albeit it cannot be clearly identified due to small magnitude of the signal that reaches about 20 % of the signal measured for the 156 nm film. Below 50 K, the increase of $M(T)$ for the 20.8 nm film is related to the presence of PM impurities in the substrate (fig. 4.7(a)).

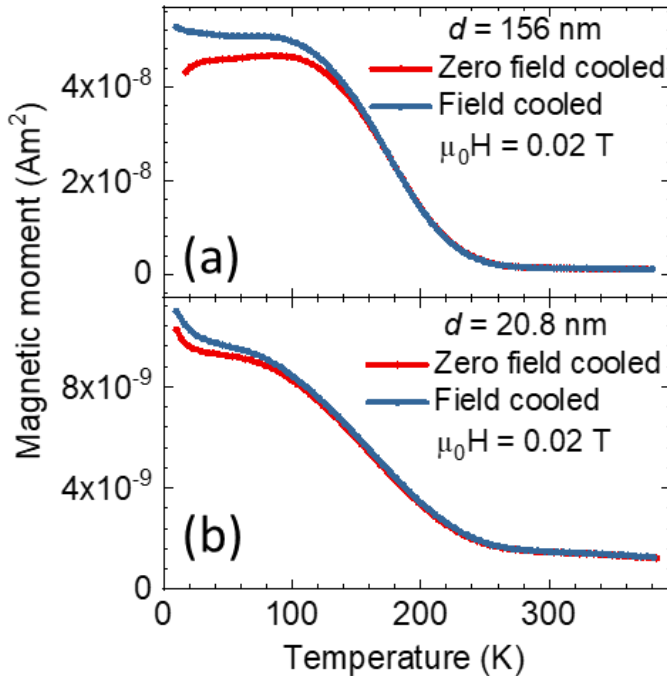


Figure 4.7 Temperature-dependent magnetic moment measured at $\mu_0 H = 0.02$ T applied parallel to the film plane for the (a) 156 and (b) 20.8 nm $(\text{Cr}_{0.5}\text{Mn}_{0.5})_2\text{GaC}$ films.

Under ZFC conditions, the competing magnetic configurations are randomly frozen below T_f , whereas in the FC case they are frozen in a preferred orientation given by the direction of the external magnetic field. This leads to a higher magnetization below T_f in the FC- $M(T)$ (blue curves) than the ZFC- $M(T)$ (red curves). The smeared-out behavior around the transition temperature T_f and the splitting of the ZFC and FC $M(T)$ curves

below T_f [122] indicates that competing magnetic interactions in $(\text{Cr}_{0.5}\text{Mn}_{0.5})_2\text{GaC}$ films are present for all thicknesses.

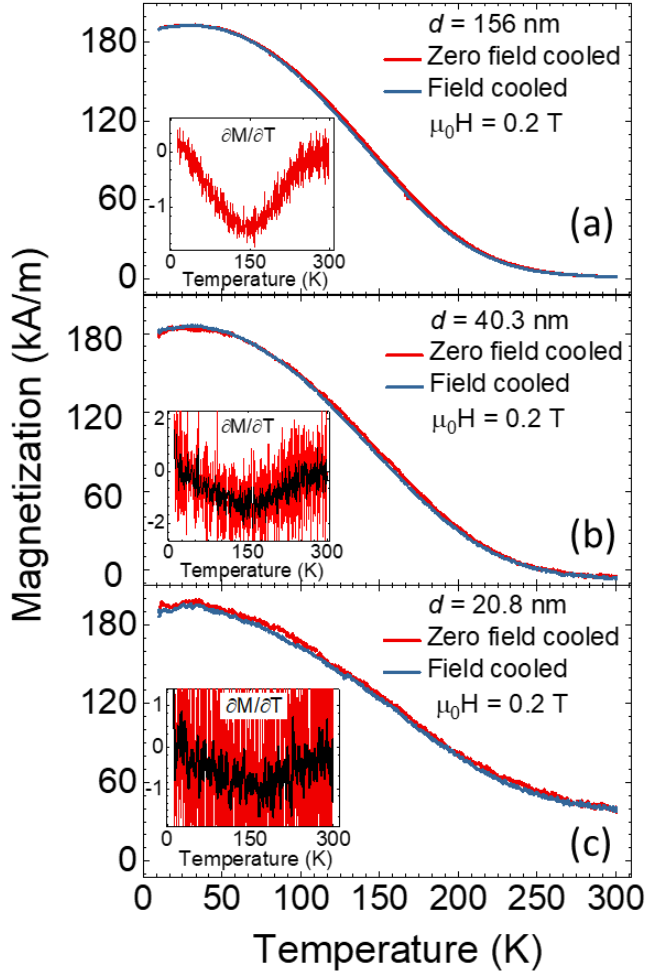


Figure 4.8 Temperature-dependent magnetization measured at $\mu_0H = 0.2 \text{ T}$ applied parallel to the film plane for the (a) 156 nm, (b) 40.3 nm and (c) 20.8 nm $(\text{Cr}_{0.5}\text{Mn}_{0.5})_2\text{GaC}$ films. The background from the substrate has been subtracted (fig. A.1). Insets show the derivatives of $M(T)$ (red) with an “adjacent averaging filter” (black) of 5 and 10 points for 40.3 nm and 20.8 nm, respectively.

By applying magnetic fields that are close to the magnetic saturation fields, the spin-glass frustration effects are usually suppressed so that the splitting between ZFC- and FC- $M(T)$ disappears (fig. 4.8). $M(T)$ for 156 nm, 40.3 nm and 20.8 nm $(\text{Cr}_{0.5}\text{Mn}_{0.5})_2\text{GaC}$ films at $\mu_0H = 0.2 \text{ T}$, which is about 80 % of the saturation-field, applied parallel to the film plane is presented in figs. 4.8(a) – (c). The magnetization of the blank MgO substrate was measured separately and subtracted from the film signal (see Appendix A1, fig. A.1). For all samples, the magnetization decreases with increasing temperature showing a broad phase transition around 160 K. Such smeared magnetic phase transition can be attributed to a presence of more than one type of magnetic interaction in the sample volume. In this case, the precise value of T_t is difficult to identify. For comparative analysis, we chose the temperature T_s where the first derivative of the magnetization $\partial M / \partial T$ shows an extremum (fig. 4.8 insets). The

“adjacent-averaging filter” in the Origin software was used to smooth the noise of the calculated derivatives for 40.3 nm and 20.8 nm films. The inflection points appear at 146 ± 5 , 159 ± 5 and 164 ± 10 K for 156 nm, 40.3 nm and 20.8 nm films, respectively. A slight decrease of T_s with increasing thickness can be suggested; however, taking into account competing interactions and a smeared transition, it can be concluded that for all thicknesses T_s is similar. The magnetic transition to PM state for $(\text{Cr}_{0.5}\text{Mn}_{0.5})_2\text{GaC}$ occurs at $T_t = 230 \pm 30$ K.

The field-dependent magnetization with $\mu_0 H$ applied parallel to the film plane was studied at 100 K for all samples. In the raw data, FM components clearly visible at low magnetic fields of 0.4 T have magnitudes of about 2×10^{-8} Am², 6×10^{-9} Am² and 3×10^{-9} Am² for 40.3 nm, 20.8 nm and 12.5 nm films, respectively (fig. 4.9(a)). The strong linear background is governed by the substrate contribution (fig. 4.9(a)) which dominates the FM response from the film at high magnetic fields. It was subtracted by performing a linear fit to the $M(H)$ at the highest measured magnetic fields between 3.5 and 5 T [123, 124]. The field-dependent volume magnetization for 156 nm, 40.3 nm, 20.8 nm and 12.5 nm after the background subtraction are shown in fig. 4.9(b). All signals show large saturation fields, which can be attributed to non-FM (PM, AFM or superparamagnetic) components.

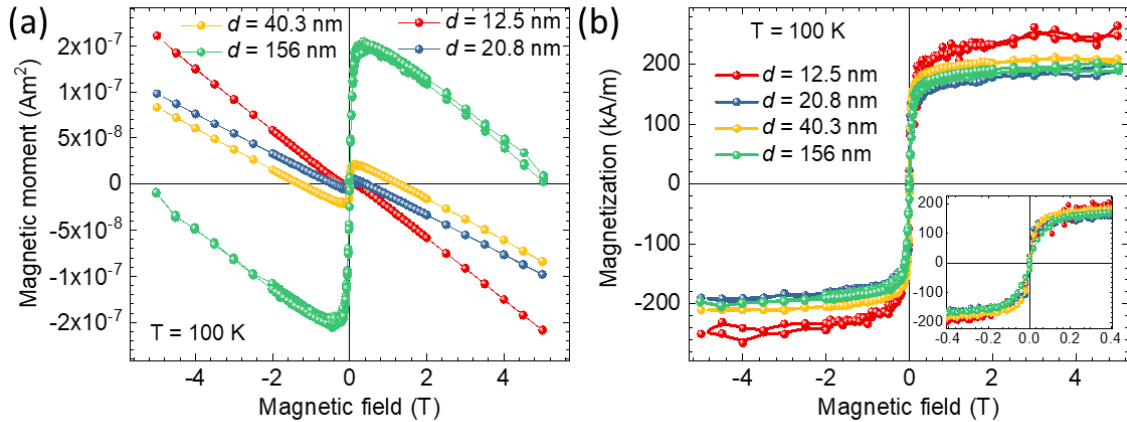


Figure 4.9 (a) Field-dependent magnetic moment for the 156 nm, 40.3 nm, 20.8 nm and 12.5 nm $(\text{Cr}_{0.5}\text{Mn}_{0.5})_2\text{GaC}$ films on MgO (111) at $T = 100$ K with $\mu_0 H$ applied parallel to the film plane. (b) Magnetization curves obtained from (a) after the background subtraction using a linear function fitted to the data between 3.5 and 5 T and after normalization with respect to volume of the films. The inset shows the magnification for ± 0.4 T.

For all films, $M(H)$ shows a similar S-shape character related to a FM order. The remanent magnetization M_r is smaller than 25 kA/m, and the coercive field $\mu_0 H_c$ is below 4 mT for all samples. At the field of 0.2 T, $M(H)$ of all films reaches about 80 % of the magnetization M_{5T} at $\mu_0 H = 5$ T. For the 156 nm, 40.3 nm and 20.8 nm films, $M_{5T} = 200$ kA/m ± 10 % is nearly identical. The error is given by the determination of the magnetic moment and the film volume. For the 12.5 nm film, $M_{5T} = 248$ kA/m is about 24 % larger than for other films. Taking in account the XRR data analysis summarized in table 4.1, the sample volume for this film was reduced by 20 %.

However, the error in M for this film is about the same magnitude due to a complex porous morphology that affects the volume determination. Thus, we suggest the thickness-independent M_{5T} for $20.8 \text{ nm} \leq d \leq 156 \text{ nm}$ [116]. It may be interpreted in a way that volume properties of $(\text{Cr}_{0.5}\text{Mn}_{0.5})_2\text{GaC}$ dominate over surface contributions as it was reported for the $(\text{Cr}_{0.75}\text{Mn}_{0.25})_2\text{GeC}$ MAX phase films [23]. $(\text{Cr}_{0.5}\text{Mn}_{0.5})_2\text{GaC}$ films show general characteristics of a soft ferromagnet which is in agreement with previous works [26, 96]. For this compound, a noncollinear FM order is reported with M_s of $0.67 \mu_B/\text{M element}$ at $30 - 50 \text{ K}$ [26].

Similar results regarding a thickness-independent M have been reported for 36 nm and 102 nm MAX phase films of $(\text{Cr}_{0.75}\text{Mn}_{0.25})_2\text{GeC}$ grown on MgO (111), for which M_s and M_r were found to be identical [23]. Since there are not many reports regarding thickness-dependent properties of magnetic MAX phases, an observed weak dependence of magnetic properties on thickness cannot be denoted as a general trend for these materials yet.

4.1.3 Angular-dependent ferromagnetic resonance

A magnetic anisotropy in the film plane was studied by an angular-dependent FMR as a function of thickness. Microwave absorption derivative spectra were recorded at the frequency $f = 9.46 \text{ GHz}$ with the modulation frequency of 100 kHz . The modulation amplitude was set to 0.6 mT , the microwave power to 19.7 mW , the quality factor was determined to be $Q = 5000$. The time constant and the conversion time on Lock-In amplifier were 20 and 40 ms, respectively. With rotating the specimen, the resonance field $\mu_0 H_r$ change can be described within a context of the shape of the energy landscape [115]. This energy landscape can be obtained in two configurations: by rotating the film-specimen along the azimuthal φ or polar θ angles with respect to an external magnetic field (fig. 2.5), which are denoted as *in-plane* and *out-of-plane*, respectively. A magnetic anisotropy, the Smit-Beljers approach was used to fit the experimental FMR data according to the free energy density containing anisotropy contributions anticipated to be present for the specimen (eq. 2.28) [60]. The fitting procedure includes a minimization of the free energy with respect to M at each angle step. Therefore, equilibrium angles for M are defined for a specified set of parameters that consists of measuring frequency f , anisotropy constants K of an expected order, g -factor and the magnetization M .

First, we discuss *in-plane* FMR measurements performed for the 12.5, 20.8 and 156 nm films at 110 K. Each specimen was rotated for more than 270° with 2° steps to ensure an identification of anisotropy contributions corresponding to two-, four- or six-fold symmetries. For the calculation, $\mu_0 H_r$ were extracted from individual FMR spectra measured at each angle step. These spectra are presented in next chapter for 110 K in fig. 4.10(a) – (b), when a magnetic field is applied in the film plane. Since the studied films exhibit a hexagonal crystal structure with the c -axis normal to the film

plane, a six-fold symmetry is expected to be present. This intrinsic feature would manifest itself as a change of $\mu_0 H_r$ with a periodicity of 60° . In addition, it should be noted that films were deposited on MgO substrates with a cut along $(111) \pm 0.5^\circ$ crystallographic orientation. Typically, even polished substrates exhibit terraces, which may induce an uniaxial magnetic anisotropy [125]. This uniaxial character can be characterized by a 180° periodic change of $\mu_0 H_r$. Therefore, the following free energy density for the *in-plane* configuration is considered:

$$F = \frac{1}{2} \mu_0 M_s \cos^2 \theta + K_{6\parallel} \sin^6 \theta \cos 6\varphi + \frac{1}{2} K_u \sin^2 \theta \cos 2\varphi - K_{2\perp} \cos^2 \theta - \mu_0 M_s H (\cos \theta \cos \theta_H + \cos(\varphi - \varphi_H) \sin \theta \sin \theta_H) \quad (4.1)$$

with the demagnetizing term, the magnetic anisotropy term of a 6th and 2nd order ($K_{6\parallel}$ and K_u , respectively), the perpendicular uniaxial magnetic anisotropy term $K_{2\perp}$, and the Zeeman density term, respectively.

In-plane FMR studies performed at 110 K showed an absence of a six-fold symmetry as well as a uniaxial two-fold symmetry for 20.8 nm and 12.5 nm films with a variation of a $\mu_0 H_r$ magnitude of about 2 % without any angular dependence. In contrast, the 156 nm film revealed a pronounced two-fold symmetry presented in fig. 4.10(a) together with the corresponding fit. For the fitting procedure, M was fixed at 200 kA/m (according to fig. 4.9(b)), whereas $K_{2\perp}$ and K_u were set as a fit parameter with a possibility to vary its magnitude as ± 90 % from the starting value. The starting value for $K_{2\perp}$ was evaluated from temperature-dependent FMR studies discussed in chapter 4.1.4. A fitting operation consisted of 10 iterations, during each of those the fit boundaries were redefined by a factor of 0.5 with the new starting value, which corresponds to the best fit to the experimental data according to the iteration. More details on this calculation method can be found in [115]. The best fit (red solid line) in fig. 4.10(a) was obtained with $K_{2\perp} = 10$ kJ/m³, $K_u = 278$ J/m³ and a *g*-factor equal to 1.99. The fact that the *in-plane* uniaxial magnetic anisotropy is found to be present only for the 156 nm film indicates an induced nature of this property. Moreover, due to a small magnitude, this induced magnetic anisotropy contribution cannot be seen in thinner films as they are less homogeneous and in the case of 12.5 nm do not form complete layers. A higher homogeneity of the 156 nm film can be a result of film relaxation processes and is confirmed by a smaller linewidth $\mu_0 \Delta H$ discussed below and presented in fig. 4.11(d) [75].

The *out-of-plane* angular-dependent $\mu_0 H_r$ for the 156 nm film at 110 K is presented in fig. 4.10(b) along with the fit. $\mu_0 H_r$ changes symmetrically with 180° periodicity, which is an expected response of a metallic FM film [60]. The experimental data were best fitted with $K_{2\perp}$ of 10.5 kJ/m³ and *g*-factor of 2.02. The magnitude of $K_{2\perp}$ correlates with $K_{2\perp}$ calculated from the *in-plane* angular FMR studies. $K_{2\perp}$ and *g*-factor for other films obtained from the fit are summarized in table 4.2, corresponding angular

dependencies and fits for $\mu_0 H_r$ are demonstrated in figs. 4.11(a) - (c), respectively. The magnetic shape anisotropy favors the magnetic moments to be aligned in the film plane, which results in a positive $K_{2\perp}$ for all films. Thus, this term has a dominant contribution to the magnetic anisotropy, which is an anticipated feature for the case of thin films [60]. From the fit, obtained $K_{2\perp}$ are found to be close to each other for all films, having the average value of $10.5 \text{ kJ/m}^3 \pm 10\%$. The g -factor is found to be nearly 2, which is consistent to earlier studies [96], where the 36 nm $(\text{Cr}_{0.5}\text{Mn}_{0.5})_2\text{GaC}$ film was described as a quasi 2D-laminar ferromagnet with the magnetic moments aligned within the basal plane and the magnetic anisotropy was found to be weak or zero with a temperature-independent $g = 2.00 \pm 0.01$ obtained for both 110 and 300 K [96]. It should be noted that for a precise determination of a g -factor, frequency-dependent studies are beneficial.

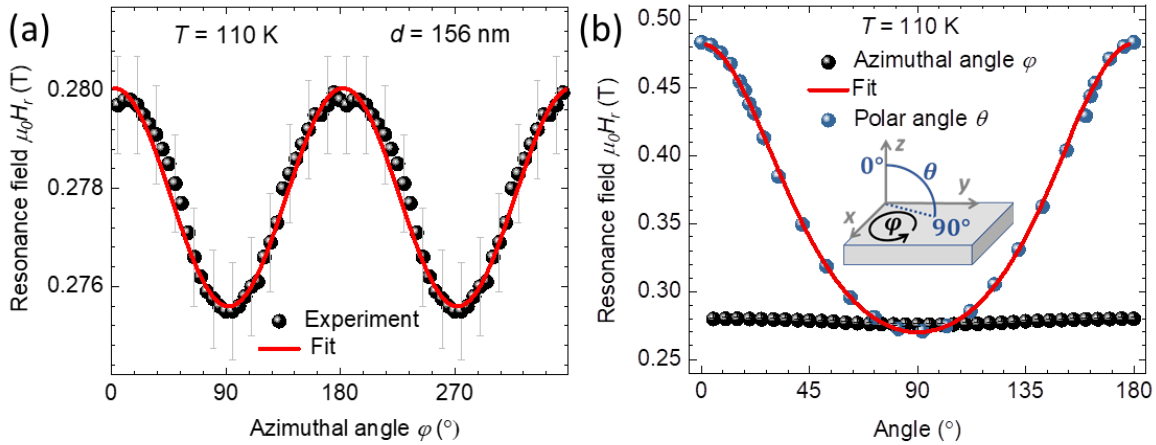


Figure 4.10 Angular-dependent resonance field $\mu_0 H_r$ for the 156 nm $(\text{Cr}_{0.5}\text{Mn}_{0.5})_2\text{GaC}$ film at 110 K. A rotation was performed by changing (a) the azimuthal angle, or (b) the azimuthal and polar angles. The red solid lines represent the best match of the fit by Smit-Beljers approach to experimental data.

Table 4.2 $K_{2\perp}$ and g -factor obtained from the FMR data fit by the Smit-Beljers approach for 110 K with a magnetic field applied in the film plane for the $(\text{Cr}_{0.5}\text{Mn}_{0.5})_2\text{GaC}$ films of different thickness d .

d , nm	$K_{2\perp}$, kJ/m^3	g -factor
12.5	11.3	1.98
20.8	11.1	1.99
40.3	9.2	1.98
156	10.5	2.02

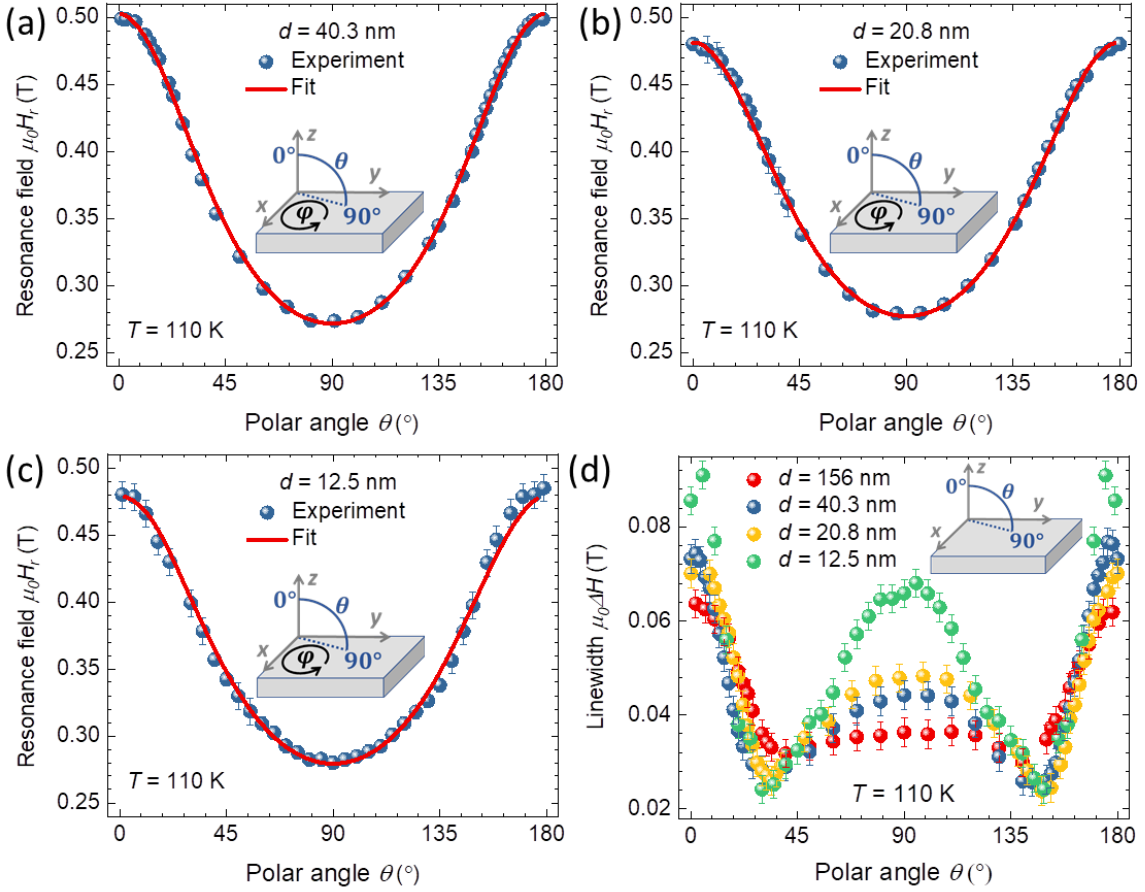


Figure 4.11 Angular-dependent resonance field $\mu_0 H_r$ measured at 110 K for the (a) 40.3 nm, (b) 20.8 nm, and (c) 12.5 nm $(\text{Cr}_{0.5}\text{Mn}_{0.5})_2\text{GaC}$ films. The angle of 0° defines the external magnetic field applied perpendicular to the film plane. The solid red line represents the result of fits by the Smit-Beljers approach. (d) angular-dependent linewidth $\mu_0 \Delta H$ at 110 K for all investigated films.

The angular-dependent $\mu_0 \Delta H$ for 110 K obtained from the *out-of-plane* specimen rotation is presented in fig. 4.11(d) for all films. Here, the smallest $\mu_0 \Delta H$ was observed at intermediate angles of 37° and 143° and the biggest $\mu_0 \Delta H$ at angles of 0° and 90° that correspond to a magnetic field applied perpendicular or parallel to the film plane, respectively. The thinner the film, the stronger this effect is visible. For instance, the thinnest 12.5 nm film showed two clear maxima at 0° and 90° with the highest $\mu_0 \Delta H$ magnitude, which indicates a larger distribution and is consistent to a discontinuous surface morphology of this film (see fig. 4.4(a)). In the case of a FM film, an angular-dependent $\mu_0 \Delta H$ shows minima at 0° and 90° , whereas the maximum should be present at the strongest variation of M direction, which is expected for intermediate angles [60, 126]. A different $\mu_0 \Delta H$ dependence observed for all films can be qualitatively explained by the presence of multiple contributions arising from specific structural properties of the material such as a roughness, the presence of grains or magnetic inhomogeneities [60,

126]. An absence of a six-fold magnetic anisotropy points out to the presence of a distribution of FMR lines that arise predominantly due to structural features described above and may dominate over the dragging effect. Such contribution is assumed for $(\text{Cr}_{0.5}\text{Mn}_{0.5})_2\text{GaC}$ films since they consist of crystallites with an average size of about and above 150 nm [26]. Also, a $\mu_0\Delta H$ magnitude at 0° and 90° decreases with increasing thickness, which is correlated with an increased homogeneity of a $(\text{Cr}_{0.5}\text{Mn}_{0.5})_2\text{GaC}$ film. Another possible contribution could arise from a two-magnon scattering process caused by scattering centers such as surface or interface imperfections [127]. However, a controlled structure with well-defined periodic defects or mosaicity of a material is required to quantitatively analyze its impact [128].

4.1.4 Temperature-dependent ferromagnetic resonance

In the previous chapter, we used FMR to study the influence of the thickness variation on magnetic anisotropies while rotating films with respect to an external magnetic field. Here, the FMR absorption derivatives $\partial\chi''/\partial H$ for 156 nm, 40.3 nm, 20.8 nm and 12.5 nm films presented in fig. 4.12 were examined in terms of temperature-dependent changes across the magnetic phase transition. All $\partial\chi''/\partial H$ were measured in a cylindrical cavity at $T = 110$ K with a magnetic field applied parallel to the film plane (chapter 3.2.3). Measurements were performed at the frequency $f = 9.46$ GHz with the modulation frequency of 100 kHz. The modulation amplitude was set to 0.3 mT, the microwave power to 19.7 mW, the quality factor was determined to be $Q = 3700$. The time constant and the conversion time on Lock-In amplifier were set from a signal optimization routine to 20 and 40 ms, respectively. $\partial\chi''/\partial H$ amplitudes for all films were normalized for a direct comparison of spectra from different films.

All films show a single broad FMR signal with similar asymmetry (fig. 4.12). Multiple narrow EPR lines from the MgO substrate can be also seen in the inset in fig. 4.12(a). The 12.5 nm film exhibits a zero-field absorption signal at the magnetic field below 0.1 T (fig. 4.12(a)), which is small compared to FMR signals of other films, but it stands out due to the amplitude normalization. The FMR signal for 12.5 nm film (fig. 4.12(b)) differs from the FMR signals for other thicknesses, showing a larger resonance field μ_0H_r , a broader linewidth $\mu_0\Delta H$ and a higher asymmetry. Here, we note that if M of the 12.5 nm film would be indeed higher by 24 % than for other films, it would result in a smaller μ_0H_r due to the shape anisotropy contribution. Therefore, FMR indirectly supports the fact that M is nearly the same for all thicknesses including the 12.5 nm with a porous morphology.

The EPR signals at magnetic fields between 0.31 and 0.38 T originate from the impurities in MgO substrates. The inset in fig. 4.12(a) shows signals for 300 K, where they are not obstructed by an FMR signal from films. The central line in the EPR spectra is detected at 0.34 T for all samples. The position and the number of the satellite peaks

are identical for all thickness series. This implies that all MgO substrates are contaminated with identical impurity elements.

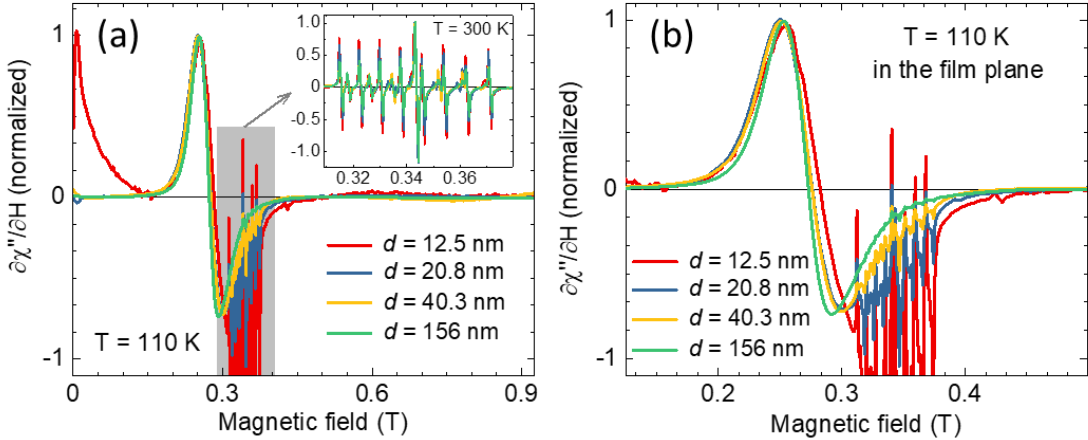


Figure 4.12 (a) Ferromagnetic resonance spectra for the 156 nm, 40.3 nm, 20.8 nm and 12.5 nm $(\text{Cr}_{0.5}\text{Mn}_{0.5})_2\text{GaC}$ films measured at 110 K. A magnetic field was applied parallel to the film plane. Narrow resonances between 0.31 and 0.38 T shown in the inset for 300 K originate from MgO inclusions. (b) Magnification of the FMR signal. Data adapted from [116].

Upon warming from 110 K, $\mu_0 H_r$ increases while approaching the magnetic phase transition at $T_t = 230 \pm 30$ K (fig. 4.8). This behavior is observed for all films. $\mu_0 H_r$ of the 12.5 nm film deviates from the response of other films at T below 170 K. This film has an inhomogeneous, porous surface morphology (fig. 4.4), which results in a smoother approach to a magnetic phase transition [116]. At temperatures up to 300 K the resonance line still can be observed; however, it is located at the position of resonances originated from the substrate, which causes a distortion of the line. Due to this distortion, $\mu_0 H_r$ for temperatures between 270 and 300 K cannot be precisely identified. Above 250 K, the compound exhibits a magnetic phase transition to a PM state [96]. It can be concluded that the magnetic phase transition of the $(\text{Cr}_{0.5}\text{Mn}_{0.5})_2\text{GaC}$ compound does not demonstrate a clear dependence as a function of a film thickness.

The temperature-dependent $\mu_0 \Delta H$ for films are presented in fig. 4.14(a). Above 170 K, the right part of the microwave absorption derivative $\partial \chi'' / \partial H$ is obstructed by signals from the substrate (fig. 4.14(b)). In the case of the 12.5 nm film, the FMR signal is obstructed already at 110 K (red line in fig. 4.12(b)), which increases the error in $\mu_0 \Delta H$ determination. Thereby, a Lorentzian derivative function was used to fit experimental spectra and obtain $\mu_0 \Delta H$ (chapter 3.2.3) for all films and temperatures. At 110 K, $\mu_0 \Delta H$ for the 156 nm film is smaller than for other films and is about 60 % from $\mu_0 \Delta H$ observed for the 12.5 nm film. $\mu_0 \Delta H$ for the 12.5 nm film is found to be broader than the one for the thicker films (fig. 4.14(a)). Such a line broadening with decreasing d provides an information regarding local inhomogeneities, which are prominent for the 12.5 nm film due to the porous surface morphology. In general, $\mu_0 \Delta H$ for all films moves towards an average magnitude of 0.045 T at 300 K. A slight $\mu_0 \Delta H$

increase above 250 K is due to approaching a transition to a PM state. These observations indicate similar magnetic relaxation mechanisms across the phase transition.

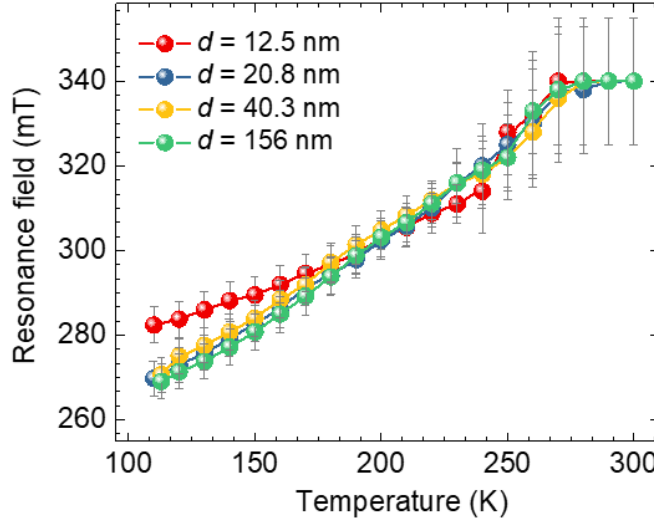


Figure 4.13 Temperature-dependent resonance field $\mu_0 H_r$ for the 156 nm, 40.3 nm, 20.8 nm and 12.5 nm $(\text{Cr}_{0.5}\text{Mn}_{0.5})_2\text{GaC}$ films with a magnetic field applied in the film plane. Adapted from [116].

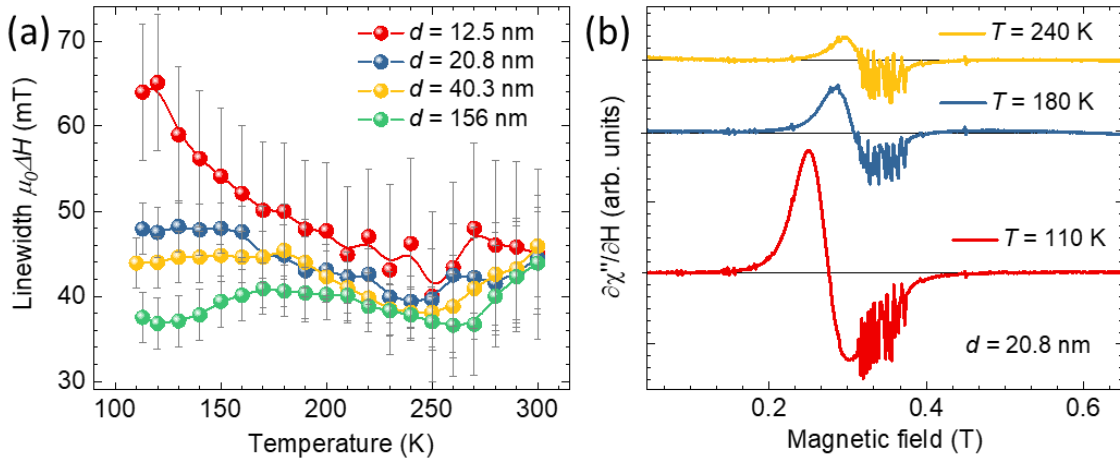


Figure 4.14 (a) Temperature-dependent linewidth $\mu_0 \Delta H$ for the 12.5 nm, 20.8 nm, 40.3 nm and 156 nm $(\text{Cr}_{0.5}\text{Mn}_{0.5})_2\text{GaC}$ films; (b) Field-dependent absorption derivatives for the 20.8 nm film at 110, 180 and 240 K. Positions, where the y -axis is zero, are displayed by the black solid line for each individual measurement.

Surface and interface effects have a big influence on a magnetic anisotropy when the film is thinner than the critical thickness, which is a material-dependent parameter [129]. A homogeneous layer formation for this compound occurs at $d > 13$ nm [116]. Within the definition of a MAX phase monolayer thickness to be equal to a c -lattice parameter, 13 nm would correspond to the thickness of about 10 monolayers [116]. As an additional contribution to a magnetic anisotropy, M of an epitaxial film grown on a substrate is anticipated to follow its roughness profile [130]. For all films, the

roughness is about 2 unit-cells according to the XRR analysis (chapter 4.1.1). Given the above, continuous $(\text{Cr}_{0.5}\text{Mn}_{0.5})_2\text{GaC}$ MAX phase films thinner than 10 monolayers are required to make surface and interface contributions dominate over the volume characteristics.

The temperature-dependent effective magnetization $\mu_0 M_{\text{eff}}$ was calculated by using eq. 2.30 - 2.31. Two contributions to $\mu_0 M_{\text{eff}}$, which are the perpendicular magnetic anisotropy and the magnetic shape anisotropy [60], were considered for the configuration, when a magnetic field is applied in the film plane. The assumption has been made since an *in-plane* magnetic anisotropy was found to be insignificant compared to the perpendicular one (see chapter 4.1.3). For the calculation, we used a *g*-factor of 2.00 ± 0.01 determined for the 34 nm film of the same compound, which is close to the free electron *g*-factor indicating a small orbital magnetic moment and is in agreement with an observed weak magnetic anisotropy [96]. With increasing temperature, $\mu_0 M_{\text{eff}}$ decreases and above 190 K is nearly the same for all films including the thinnest 12.5 nm film (fig. 4.15). The thickness-independent $\mu_0 M_{\text{eff}}$ at $T > 190$ K demonstrates similar magnetic transformations that occur in films while approaching a PM state.

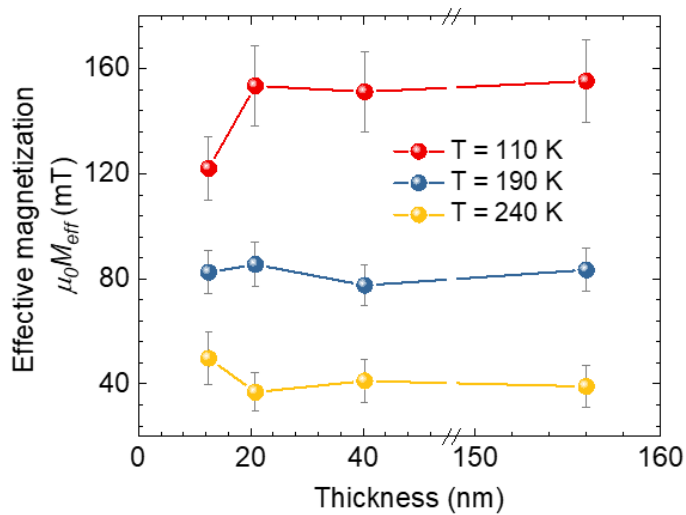


Figure 4.15 Thickness-dependent effective magnetization $\mu_0 M_{\text{eff}}$ at $T = 110$, 190 and 240 K for the 156 nm, 40.3 nm, 20.8 nm and 12.5 nm $(\text{Cr}_{0.5}\text{Mn}_{0.5})_2\text{GaC}$ films. Partially adapted from [116].

At 110 K, $\mu_0 M_{\text{eff}}$ was found to be 153, 151 and 155 mT for 20.8, 40.3 and 156 nm films, respectively. This difference is indistinguishable within the experimental error related to the determination of $\mu_0 H_r$, *g*-factor and *f*. In contrast, $\mu_0 M_{\text{eff}}$ for the 12.5 nm film is 122 mT, which is about 20 % smaller than $\mu_0 M_{\text{eff}}$ for the thicker films. A reduction of $\mu_0 M_{\text{eff}}$ is associated with a discontinuous surface morphology (fig. 4.4). The volumetric filling factor commonly used to account for an effective anisotropy in non-continuous films [131] was evaluated to be of 80 ± 5 % for 12.5 nm film. Additionally, the XRR data analysis showed about 20 % effective density reduction for this film, which correlated with the volumetric filling factor. We concluded that a reduced $\mu_0 M_{\text{eff}}$

results from an inhomogeneous surface of the film [116]. The summary of the magnetic parameters at 110 K for the $(\text{Cr}_{0.5}\text{Mn}_{0.5})_2\text{GaC}$ films is given in table 4.3.

Table 4.3 Resonance field μ_0H_r , effective magnetization μ_0M_{eff} , perpendicular magnetic anisotropy constant $K_{2\perp}$, and linewidth $\mu_0\Delta H$ obtained from the FMR data measured at 110 K for 12.5 nm, 20.8 nm, 40.3 nm and 156 nm $(\text{Cr}_{0.5}\text{Mn}_{0.5})_2\text{GaC}$ films with a magnetic field applied in the film plane.

d , nm	μ_0H_r , mT	μ_0M_{eff} , mT	$K_{2\perp}$, kJ/m ³	$\mu_0\Delta H$, mT
12.5	282	122	13.3	66
20.8	275	153	10.1	50
40.3	276	151	10.4	48
156	273	155	9.9	40

The contribution of the perpendicular magnetic anisotropy energy constant $K_{2\perp}$ at 110 K was calculated from eq. 2.31 using μ_0M_{eff} determined above and $M = 200$ kA/m obtained in chapter 4.1.2. For all films, the thickness-dependent $K_{2\perp}$ presented in fig. 4.16(a) is nearly the same and is $K_{2\perp} = 10.1$ kJ/m³ \pm 14 % except the 12.5 nm film with $K_{2\perp} = 13.3$ kJ/m³ \pm 14 %. The error is given by the determination of M_s and μ_0M_{eff} . An observed increase of an intrinsic anisotropy $K_{2\perp}$ can be associated with the influence of a porous morphology discussed in chapter 4.1.1 (fig. 4.4). The effective volume K_v and surface K_s contributions to the total magnetic anisotropy $K_{2\perp}$ can be examined by the eq. 2.31 [60]. These contributions were determined from the plot of $K_{2\perp}$ multiplied by the thickness d as a function of d [60], where the slope gives K_v and the intercept is K_s which includes a substrate-film and film-air interfaces. A linear fit applied to the plotted $K_{2\perp}d$ versus d function (fig. 4.16(b)) gave the effective $K_v = 9.7 \pm 0.4$ kJ/m³ and $K_s = 2.7 \pm 1.5 \times 10^{-5}$ J/m².

An intrinsic K_s is anticipated to be constant for the same material and, according to eq. 2.31, the effective surface contribution K_s/d should be weaker with d increase [60]. For $(\text{Cr}_{0.5}\text{Mn}_{0.5})_2\text{GaC}$, the K_s/d term is evaluated to be 3.6 kJ/m³, 0.4 kJ/m³, 0.7 kJ/m³ and 0.2 kJ/m³ for 12.5 nm, 20.8 nm, 40.3 nm and 156 nm, respectively. It should be noted that the magnitude of these values is within the error of the K_v determination. For each individual d consequently recalculated from eq. 2.31, obtained K_s are 3.8×10^{-5} J/m², 2.7×10^{-5} J/m² and 0.9×10^{-5} J/m² for 156 nm, 40.3 nm and 20.8 nm films, respectively with 4.5×10^{-5} J/m² for the 12.5 nm film. A trend of K_s decrease with d decrease is observed, except for the thinnest film that showed the highest K_s . However, a substantial error in K_s determination reaching 50 % coming from the linear fit shown in fig. 4.16(b) has to be taken into account, which results in similar values for all films with the biggest surface contribution for the 12.5 nm film. This result is in agreement with a discontinuous surface morphology observed for this film [116]. These films

were reported to exhibit lateral grains of 150 nm [26], therefore, individual local effects cannot be neglected.

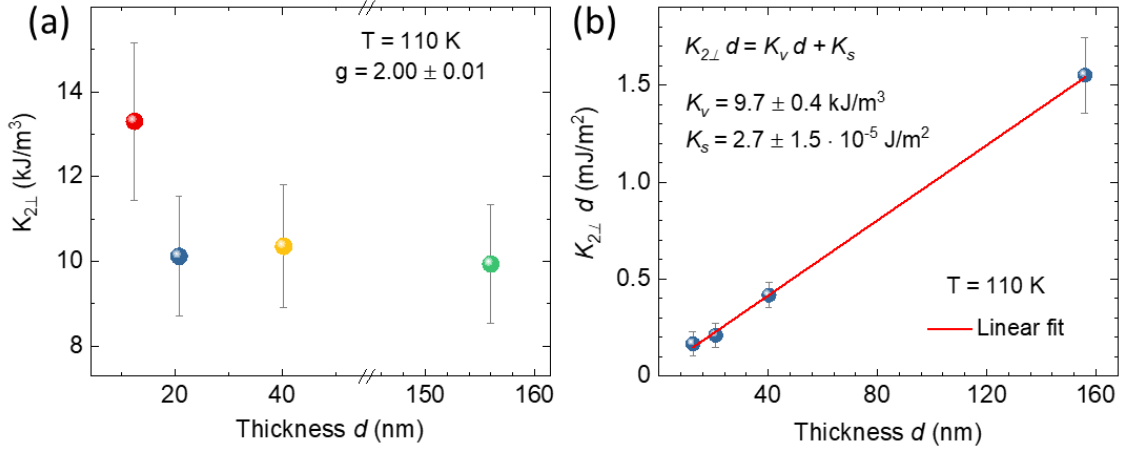


Figure 4.16 (a) Thickness-dependent perpendicular magnetic anisotropy constant $K_{2\perp}$ for the 156 nm, 40.3 nm, 20.8 nm and 12.5 nm $(\text{Cr}_{0.5}\text{Mn}_{0.5})_2\text{GaC}$ films at 110 K for the case when a magnetic field is applied in the film plane. (b) $K_{2\perp}$ multiplied by the thickness d (blue circles) to determine the volume K_v and surface K_s contributions from the linear fit (red line).

The type of the intrinsic magnetic anisotropy for the $(\text{Cr}_{0.5}\text{Mn}_{0.5})_2\text{GaC}$ compound was examined by the Callen-Callen theory [76, 77] that formulates a universal temperature dependence as a power law given in eq. 2.23. For this analysis, experimental data for the 156 nm film were used: temperature dependencies of $K_{2\perp}$ and M were rescaled by values received at 110 K to obtain reduced ratios $K_{2\perp}(T)/K_{2\perp}(100 \text{ K})$ and $M(T)/M_s(100 \text{ K})$ [76, 77]. The exponent α determined from the fit according to eq. 2.23 showed the best fit to experimental data at $\alpha = 2.7 \pm 0.1$ (fig. 4.17(a)). Solutions of this equation using different fixed α were obtained by varying α from 2.0 to 3.5 to compare the fit quality. As it can be seen in fig. 4.17(a), the equally good match is observed for α between 2.5 and 3.0, which gives a span for the error of α determination. For the next step, $K_{2\perp}(T)/K_{2\perp}(100 \text{ K})$ is plotted versus $(M(T)/M_s(100 \text{ K}))^\alpha$ calculated for each fixed α (fig. 4.17(b)).

Based on eq. 2.23, this representation should exhibit a linear dependence if it obeys the Callen-Callen power law. Indeed, the experimental data fulfills this condition and a linear behavior of the simulated curves is observed for α equal to 2.5 and 3.0, whereas $\alpha = 2.0$ and 3.5 reveals a curvature. The obtained span for α is close to the theoretical value of $\alpha = 3$ given for the ferromagnet with a uniaxial magnetic anisotropy [76, 77, 132]. Despite $(\text{Cr}_{0.5}\text{Mn}_{0.5})_2\text{GaC}$ is not a classical ferromagnet and exhibits competing interactions [26, 96], the results are in agreement with the Callen-Callen law. A reduced α may result from a presence of an itinerant ferromagnetism in the compound being based on a transition metal, as it was proposed in [133] for Mn_5Ge_3 compound with $\alpha = 1.5$. A coexistence of an itinerant and localized magnetism was reported for the Mn-doped Cr_2GeC MAX phase [134], which is a close related compound to those studied in

this thesis. An itinerant nature of a magnetism for $(\text{Cr}_{0.5}\text{Mn}_{0.5})_2\text{GaC}$ was also suggested in [96].

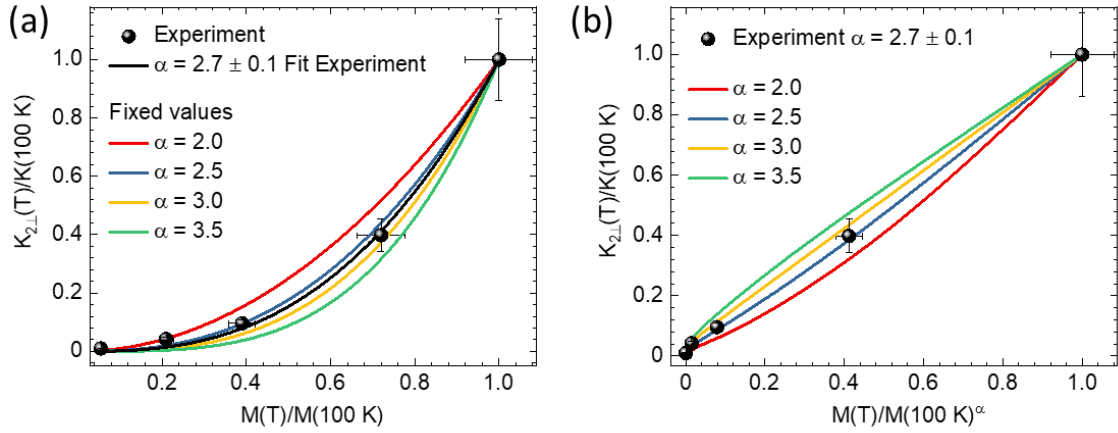


Figure 4.17 (a) $K_{2\perp}$ versus $M(T)/M(100 \text{ K})$ for α determination according to eq. 2.23. (b) Comparison between $K_{2\perp}(T)/K_{2\perp}(100 \text{ K})$ and $M(T)/M(100 \text{ K})^\alpha$. Data analyzed for the 156 nm $(\text{Cr}_{0.5}\text{Mn}_{0.5})_2\text{GaC}$ film.

4.1.5 Ferromagnetic resonance with the time span of 1 year

Most metallic magnetic ultrathin films are magnetically and chemically unstable under environmental conditions [60, 75]. Metallic films often do not possess a sufficient corrosion or oxidation resistance, so to protect the surface against degradation a capping layer is frequently used [130, 135]. Surface modifications can significantly influence magnetic properties of a system and, thus, reduce its functionality [130]. For modern applications in electronic devices like magnetic sensors it is essential to have environmentally stable ultrathin films. A weak thickness dependence of the magnetic response is considered as an additional benefit as it gives a possibility for developers to vary thickness when accounting for a reliable response.

To investigate the possible surface degradation via oxidation or corrosion the unprotected 20.8 nm $(\text{Cr}_{0.5}\text{Mn}_{0.5})_2\text{GaC}$ film was exposed with its surface to air at ambient conditions. FMR spectra were measured over the time span of 1 year (fig. 4.18). After proper background subtraction the spectra were normalized in an amplitude to compare $\mu_0\Delta H$ and μ_0H_r , which are sensitive to changes in a surface or volume magnetic anisotropy. The intensity is not discussed as it depends on the sample location and an adjustment of the experimental setup. In fig. 4.18, it is clearly visible that neither the linewidth $\mu_0\Delta H$ nor the resonance field μ_0H_r experienced a significant shift, both lines overlap. The “noise” peaks between 0.32 and 0.38 T are resonances, which originate from PM impurities in MgO substrate [116].

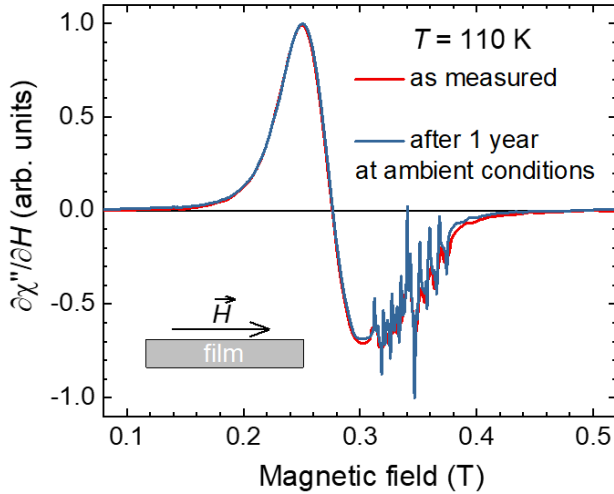


Figure 4.18 Normalized absorption derivatives measured on the same sample for the 20.8 nm $(\text{Cr}_{0.5}\text{Mn}_{0.5})_2\text{GaC}$ film with a magnetic field applied in the film plane recorded for the time interval of 1 year. Adapted from [116].

The result implies that the magnetic properties remained stable and did not experience changes due to a surface modification by oxidation or deterioration. Such a response indicates a high environmental stability of the 20.8 nm film at ambient conditions for over than one year. In contrast, $(\text{Cr, Mn})_2\text{GeC}$ MAX phase films were found to change its magnetic properties after 6 months at ambient conditions. Metallic surfaces show a rapid oxidation of several nanometers within minutes, however, the oxidation does not go further into material and the passivation layer occurs [136]. We suggest a similar passivation surface effect in MAX phase $(\text{Cr}_{0.5}\text{Mn}_{0.5})_2\text{GaC}$ films due to strong bonds between M-X-M slabs. It should be noted that oxides were not identified by XRD studies.

4.2 Mn₂GaC film

The magnetic MAX phase Mn₂GaC film with the thickness of 100 nm was one of the first ternary magnetic compounds that revealed a long-range magnetic order [24]. The film synthesis and primary structural characterization by XRD were performed by the group of Prof. J. Rosén [24]. TEM studies were carried out by M. Spasova [98]. The high-resolution double-axis X-ray diffraction (HR-XRD) data were provided by T. Hase, F. Magnus, V. Kapaklis and Á.S. Ingason [98]. Electrotransport data were obtained by U. Wiedwald. Further studies presented in this chapter include magnetometry, scanning electron microscopy, and ferromagnetic resonance (FMR) data analysis. Partially, the XRD, TEM, magnetometry and electrotransport results presented in this thesis were published in [98].

4.2.1 Crystal structure and phase purity

The heteroepitaxial Mn₂GaC film was deposited on the MgO (111) substrate by magnetron sputtering. The atomically layered normal to the basal plane MAX phase structure was sustained with a lattice mismatch of about 2.7 % between *a*-lattice parameters of the substrate and the film [34]. The X-ray diffractogram measured in $\theta - 2\theta$ configuration (chapter 3.1.1) is presented in fig. 4.19. Here, detected (000l) reflections are plotted in a logarithmic scale and are visible up to $l = 12$, which represents a good crystallinity of the film [98]. These reflections originate from crystal planes grown normal to the basal film plane.

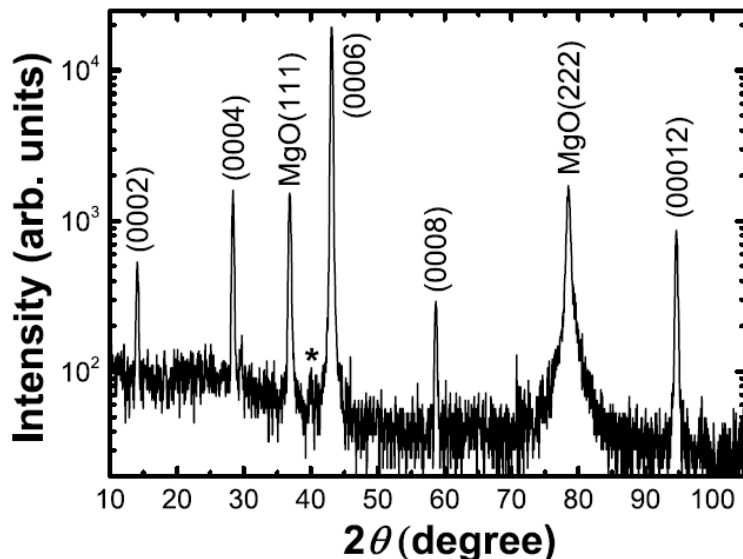


Figure 4.19 $\theta - 2\theta$ X-ray diffraction scan for the 100 nm Mn₂GaC film measured at $T = 300$ K. An asterisk at about 40 deg. is attributed to trace amounts of Mn₃GaC (111) [98].

The film is found to be phase-pure since only Mn₂GaC and MgO reflections were observed, except an insignificant peak at about 40° marked by an asterisk in fig. 4.19,

which was defined to be an antiperovskite Mn_3GaC (111) reflection [137]. The Mn_3GaC compound exhibits a sharp magnetic phase transition at about 160 K [137], which was not detected by temperature-dependent magnetization studies (fig. 4.28). Thus, only trace amounts of other phases are expected for this specimen. The determined *c*-lattice parameter is $c = 1.255$ nm. The in-plane *a*-lattice parameter of $a = 0.290$ nm was identified from the $(10\bar{1}3)$ peak, data was obtained by tilting and rotating the sample [98]. Therefore, the calculated unit cell volume is 91.405 \AA^3 .

The TEM study is summarized in fig. 4.20 [98]. A low magnification cross-sectional bright-field TEM image presented in fig. 4.20(a) reveals a uniform film with the thickness of 100 nm. Note that lateral grains of around 150 nm cannot be excluded since the contrast difference can be observed and grains of about 400 nm were reported in earlier work [24].

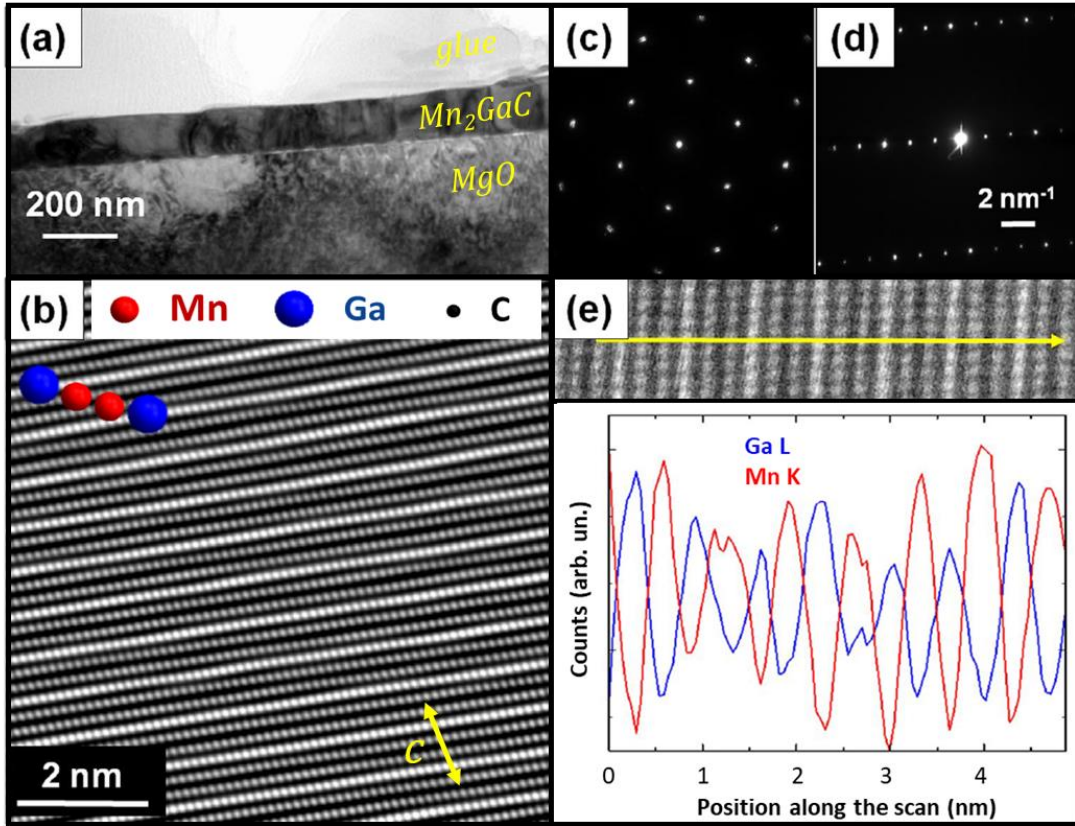


Figure 4.20 Mn_2GaC film on MgO : (a) Bright-field transmission electron microscopy (TEM) image, cross-section; (b) High-angle annular dark-field scanning TEM (HAADF/STEM) image, cross-section. White or grey points correspond to Ga or Mn atomic columns, respectively. Selected area electron diffraction patterns recorded (c) in the plane of the film with the [0001] zone axis and (d) the cross-section of the $[0\bar{1}\bar{1}0]$ zone axis. (e) The line-scan analysis using STEM/energy-dispersive X-ray (EDX) spectroscopy along the yellow arrow on the HAADF/STEM image that demonstrates a Ga and Mn distribution. Adapted from [98].

The high-angle annular dark-field scanning HAADF/STEM image of the film's cross-section shown in fig. 4.20(b) demonstrates the atomic columns periodically stacked along the *c*-axis. This highly ordered pattern confirms the MAX phase structure. The

brightness of the atomic columns is proportional to the n^{th} power of the atomic number Z , so the brightest atomic columns correspond to Ga (blue) and two grey atomic columns correspond to Mn (red). The line-scan performed by STEM energy dispersive X-ray analysis (EDX) shown in fig. 4.20(e) demonstrates periodically arranged Mn and Ga atomic planes along the c -axis [98]. The selected area electron diffraction patterns for the basal-plane and the cross-section views shown in fig. 4.20(c) - (d) display a high crystal quality. The determined $c = 1.26 \text{ nm}$ and $a = 0.294 \text{ nm}$ are in agreement with XRD studies giving a difference of about 1.4 % for the a - and of about 0.4 % for the c -lattice parameter. Therefore, the Mn_2GaC film consists of uninterrupted atomic layers stacked along c -axis normal to the basal plane with a lateral texture that includes grains of about 150 – 400 nm.

A surface roughness and chemical homogeneity are important characteristics that could significantly influence magnetic properties of the film [138, 139]. By using SEM imaging, the 100 nm Mn_2GaC film's surface morphology was studied in comparison to a 370 nm Mn_2GaC film (figs. 4.21(a) - (d)).

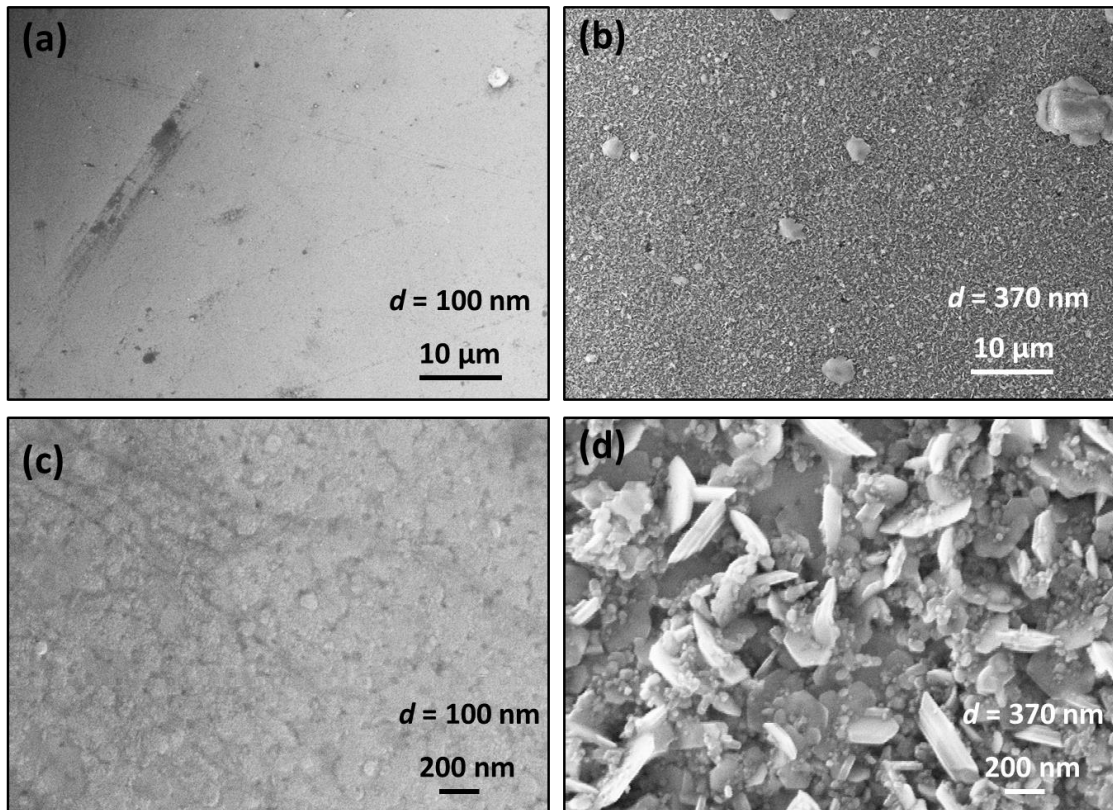


Figure 4.21 Scanning electron microscopy images for the (a), (c) 100 nm and (b), (d) 370 nm Mn_2GaC films to compare their surface morphology.

The 100 nm film possesses a smooth surface in contrast to the 370 nm film, which revealed a heterogeneous surface morphology seen as a contrast difference. According to EDX analysis, observed droplets on the surface are associated with Ga splashes that can be a consequence of the deposition process. A synthesis of a MAX phase without Ga

drops on the surface is challenging. Nevertheless, phase-pure Ga-containing MAX phase films of a good crystalline quality were successfully grown by magnetron sputtering by using a specially designed crucible placed under the substrate [26, 27].

On the nanoscale, a difference in a surface morphology is more pronounced: the 370 nm film formed flakes protruded from the surface as presented in figs. 4.21(b), (d). These features can be attributed to the step-flow growth, where basal planes form faster than the *c*-axis [86] and at the critical thickness this process may cause a formation of dislocation planes that stick out of the layer. Such inhomogeneous structures contribute into the magnetization process since a domain structure become complex and the material possesses a mixed magnetic anisotropy distribution. However, the 100 nm film, studied in this thesis, exhibits a homogeneous surface without flakes that those observed for the 370 nm film. Nevertheless, the surface is rough on the nanoscale, which should be considered for the magnetic characterization, e.g. magnetic anisotropy [140].

4.2.2 Sign reversal of the large uniaxial magnetostriction

The influence of temperature and external magnetic field variation on the *c*-lattice parameter evolution of Mn₂GaC is studied in this chapter. Magnetostrictive effects in AFM materials are subject of an intense study as, in contrast to FM materials, different magnetic structures can be stabilized by varying temperature and magnetic field across the magnetic phase transition. Competitive AFM and FM interactions across the Ga atomic layers in Mn-Ga-Mn chains are predicted by density functional theory [40]. This complex magnetic behavior results in a strong dependence of the Mn₂GaC compound magnetic ground state configuration on pressure (*c*-axis lattice parameter), temperature and external magnetic fields [40]. Mn-based systems like binary orthorhombic MnP and related materials often form complex noncollinear magnetic phases, where the change from AFM to FM configuration depends on the interatomic distance between Mn atoms [141].

The consecutive parallel planes of atoms are associated with the d_{hkl} spacing which is defined as the distance between two neighboring planes [142]. Field- or temperature-dependent structural transformations of a magnetic material can be characterized by this parameter. Here, the position of the most intensive (0006) Bragg reflection was examined as a function of the scattering vector Q under an external magnetic field up to 3 T applied parallel to the film plane. High-resolution X-ray diffraction scans were performed for two fixed temperatures of 200 and 270 K (figs. 4.22(a) and (b), respectively) that are below and above the magneto-structural phase transition of $T_t = 214$ K [98]. At 200 K, where Mn₂GaC is in the noncollinear AFM state, the diffraction peak moved towards smaller Q as the external magnetic field increases. It denotes an expansion effect on the *c*-axis lattice parameter. The opposite behavior is tracked for 270 K, where the material is in an AFM state: the (0006)

diffraction peak moved towards larger Q with increasing field indicating a contraction of the c -lattice [98].

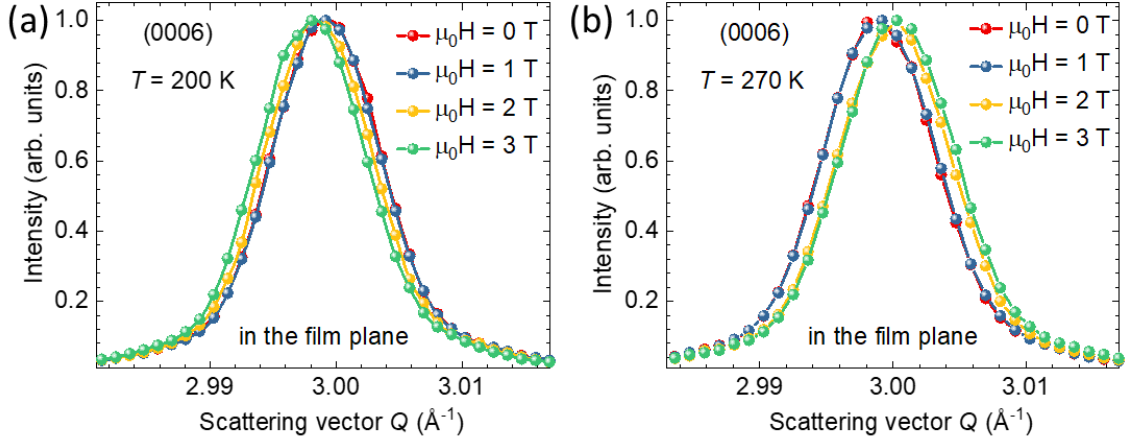


Figure 4.22 High-resolution X-ray diffraction scan in the vicinity of the (0006) reflection as a function of the scattering vector Q at magnetic fields of $0 \text{ T} \leq \mu_0 H \leq 3 \text{ T}$ applied parallel to the film plane: (a) below and (b) above the magneto-structural phase transition at 214 K [98].

An interplane distance change Δd with respect to the corresponding d_0 at zero magnetic field was recalculated for both temperatures using relations between the general equation of interplanar spacing d_{hkl} for a hexagonal lattice and the Bragg condition [142]

$$|\vec{Q}| = \frac{2\pi}{d_{hkl}} = \frac{4\pi \sin\theta}{n\lambda}, \quad \frac{\Delta d}{d_0} = \frac{d_{H \neq 0} - d_{H=0}}{d_{H=0}}, \quad (4.2)$$

where a and c are the lattice constants, θ is the angle of incidence for the atomic plane with Miller's indices hkl , λ is the X-ray wavelength. In this work, $\Delta d / d_0$ defines the uniaxial magnetostriction and displays a relative change in the c -axis (fig. 4.23(a)) upon the magnetic field applied parallel to the film plane. The MgO substrate was measured separately and showed a constant d -spacing as a function of an applied magnetic field [98]. $\Delta d / d_0$ at temperatures above the magneto-structural phase transition is negative indicating a c -lattice contraction with increasing the applied magnetic field. In contrast, $\Delta d / d_0$ becomes positive below T_t revealing a tensile strain [98]. Up to $\mu_0 H = 0.5 \text{ T}$, $\Delta d / d_0$ is close to zero for 280 K and there is a small decrease for 200 K which is indistinguishable within the experimental error. With increasing the field, an almost linear response was observed at magnetic fields between 1.5 and 2.5 T for both temperatures. Due to technical limitations, measurements were performed up to 3 T. Therefore, only a trend to a saturation could be proposed for higher magnetic fields. Presumably, at these fields the magnetic moments should be aligned with the external magnetic field. Albeit, the Mn₂GaC exhibits competing AFM and FM interactions [40], which should be taken into account since it is not fully understood if

these fields are enough to complete a field-induced alignment of an AFM subsystem in Mn_2GaC .

Quantitatively, $\Delta d / d_0$ of $(0.45 \pm 0.04) \times 10^{-3}$ or 450 ± 40 ppm at $\mu_0 H = 3$ T for both cases is determined, which is comparable to approximately 500 ppm at $\mu_0 H = 0.1$ T known for TbFe/FeCo multilayers and to -1200 ppm at $\mu_0 H = 0.5$ T reported for SmFeB amorphous films [65]. Such large uniaxial magnetostriction can be attributed to a magnetic moments' reorientation during field-induced metatransitions from AFM or noncollinear AFM towards FM configuration. This process leads to a significant c -lattice modification across T_t which is schematically shown in fig. 4.23(b) [98].

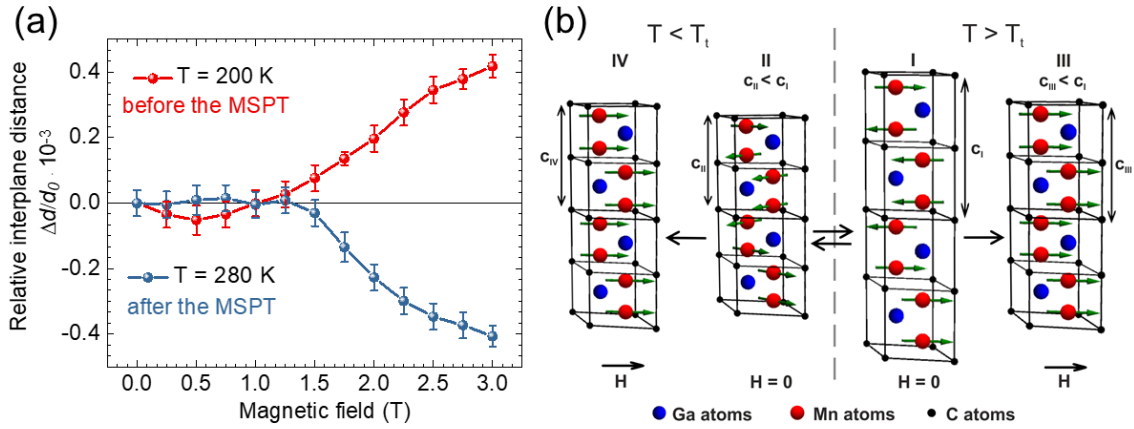


Figure 4.23 (a) Field-dependent interplane distance Δd with respect to the d -spacing at zero field d_0 for 200 and 280 K with a magnetic field applied parallel to the Mn_2GaC film plane. (b) Magneto-structural transformations across the transition temperature T_t shown on a doubled unit-cell: (I) At $T > T_t$, the system has an AFM configuration and the spin alignment is predominantly collinear. (II) At $T < T_t$, the Mn_2GaC undergoes a magnetic phase transition characterized by a magnetic spin transformation to a noncollinear AFM state resulting in a c -lattice compression ($C_{\text{II}} < C_{\text{I}}$). An external magnetic field initiates a parallel spin alignment for (III) and (IV) cases, resulting in a c -lattice compression ($C_{\text{III}} < C_{\text{I}}$) and expansion ($C_{\text{IV}} > C_{\text{II}}$), respectively. Adapted from [98].

The observed magnetic transformations are schematically shown in fig. 4.23(b). The largest c -axis lattice compression by around 0.2 % [40] arises across the magneto-structural phase transition without an applied magnetic field, which is presented from (I) to (II) in fig. 4.23(b). FM alignment of the magnetic moments leads to a compression by 0.045 % at $T > T_t$ from (I) to (III) and an expansion by 0.045% at $T < T_t$ from (II) to (IV). The temperature induced lattice compression from (I) to (II) is approximately 4.4 times larger than the magnetic field induced negative and positive magnetostriction. The sign inversion at T_t implies that the sign of the exchange coupling between Mn moments across the Ga atomic layers has an oscillatory-like behavior as a function of the c -axis lattice constant. A sign change of the exchange coupling as a function of the c -lattice parameter is expected for a layered magnetic system with competing interactions [40]. No a -lattice change was reported with the temperature variation [40]. The unit cell volume change should be further confirmed by complementary

measurements to study a possible simultaneous a -lattice modification upon an applied external magnetic field.

A c -lattice change as a function of temperature and a magnetic field across the phase transition (fig. 4.24) was plotted to qualitatively describe the observed material's response. A c -lattice compression by 0.045 % occurs when $\mu_0 H = 3$ T is applied (markers 1 → 2 in fig. 4.24) at 270 K and a lattice expansion by the same value appears at 200 K (markers 3 → 4 in fig. 4.24). The transition 1 → 3 redrawn from [40] causes a compression by about 0.2 % without an applied magnetic field. This oscillatory lattice modification is presumably caused by a field-induced FM-like alignment due to the magnetic moments' reorientation. In addition, it can be assumed that the relative c -lattice compression of approximately -0.1 % with regard to the AFM configuration (the reference state 1 in fig. 4.24) may be an equilibrium c -lattice for the stabilization of the collinear magnetic configuration.

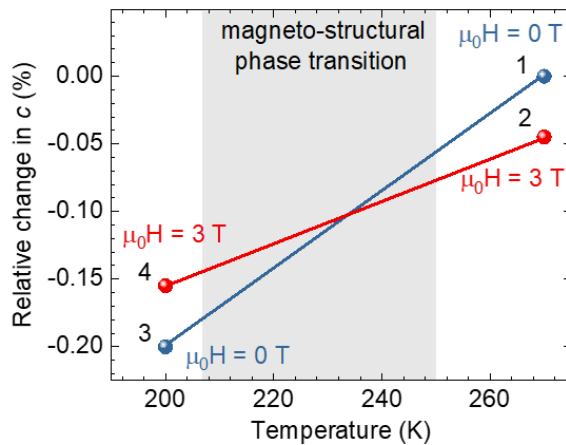


Figure 4.24 Relative c -lattice change with respect to the reference at 270 K at $\mu_0 H = 0$. Blue and red circles represent states at $\mu_0 H = 0$ and 3 T, respectively. The grey area indicates the magneto-structural phase transition. Redrawn from [98].

Hence, the noncollinear states 2 and 4 with a magnetic field induced FM can be understood as intermediate states between the magnetic configurations stabilized at fixed temperatures without an applied magnetic field. The correlation between the observed uniaxial magnetostriction and the magnetoresistance for Mn₂GaC across the magneto-structural phase transition is discussed in chapter 4.2.3.

4.2.3 Field- and temperature-dependent magnetoresistance

The electrical resistivity ρ as a function of temperature (fig. 4.25) decreases with decreasing temperature revealing a general metallic behavior [55]. At 300 K, the measured ρ for the Mn₂GaC film is 2 $\mu\Omega\text{m}$ which is comparable to 1.5 $\mu\Omega\text{m}$ obtained for the quaternary (M_{0.5}Mn_{0.5})₂GaC MAX phase films [95]. The observed non-linear behavior of $\rho(T)$ above 200 K correlates with a similar trend obtained for the Ti₂AlC and Cr₂AlC [143] and Cr_{2-x}M_xGeC with M = Ti, V, Mn, Fe, and Mo [144] MAX phase

compounds, where it was ascribed to phonon contributions. The deflection of $\rho(T)$ at 300 K becomes stronger with increasing the applied magnetic field. Besides, the influence of the magneto-structural transformations can be observed in the magnification near the transition temperature (fig. 4.25(b)). These transformations result in a gap between the ascending and the descending branches in $\rho(T)$ curves. This gap shows a pronounced field dependence being about 0.035 $\mu\Omega\text{m}$ for μ_0H of 5 and 9 T, and 0.046 $\mu\Omega\text{m}$ for $\mu_0H = 0$. Such an observation of a larger gap for $\mu_0H = 0$ correlates good with the magnetostriction studies (chapter 4.2.2) reporting the larger *c*-lattice change at $\mu_0H = 0$ than with the presence of $\mu_0H \neq 0$.

The residual resistivity ratio (RRR) calculated for Mn_2GaC and $(\text{Mo}_{0.5}\text{Mn}_{0.5})_2\text{GaC}$ by the eq. 2.15 is 3.0 and 1.3 [95], respectively. Since the influence of structural imperfections on electric properties is shown to be stronger in quaternary alloys due to an increase of additional defects [144], the obtained larger RRR for the ternary compound is in agreement with this model.

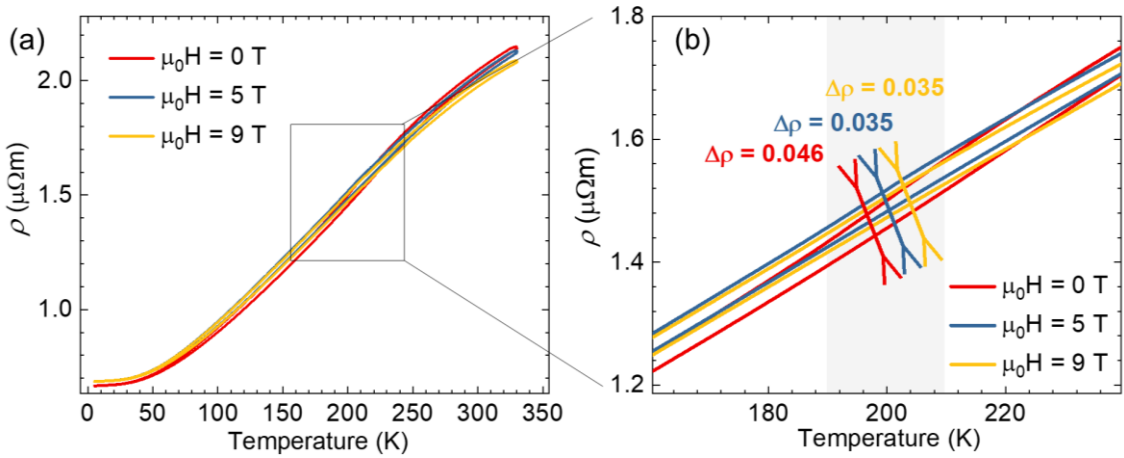


Figure 4.25 (a) Temperature-dependent electrical resistivity ρ for different external magnetic fields including cooling and warming curves, (b) Magneto-structural phase transition area, where the splitting between the cooling and warming branches was observed. Adapted from [98].

The magnetoresistance (MR) was calculated according to the eq. 2.14 [47]

$$MR = \frac{\Delta\rho}{\rho} = \frac{\rho_{9T} - \rho_{0T}}{\rho_{0T}} , \quad (4.3)$$

where ρ_{9T} and ρ_{0T} are resistivities measured at 9 T and at 0 T, respectively. From the temperature-dependent ρ (fig. 4.25(a)), at $T = 300$ K, $\Delta\rho/\rho$ was found to be negative and of -0.9 % and -2.5 % for $\mu_0H = 5$ and 9 T. In contrast, at $T = 10$ K below T_t , $\Delta\rho/\rho$ is +2.9 % for both applied magnetic fields. The origin of this non-monotonic temperature dependence may be understood by inspecting the first derivative $d\rho/dT$ (fig. 4.26(b)). It displays a broad though distinct maximum near T_t indicating a strong influence of the magneto-structural transformations (chapter 4.2.2) on electrical properties, as the

spin configuration changes from a noncollinear AFM to a field induced FM state. The results are summarized in table 4.4.

Table 4.4 The residual resistivity ratio (RRR), the magnetoresistance (MR) and the electrical resistivity ρ for the 100 nm Mn₂GaC film at different applied magnetic fields μ_0H .

Applied μ_0H , T	RRR	MR, %		ρ , $\mu\Omega m$	
		T = 10 K	T = 300 K	T = 10 K	T = 300 K
0	3.05	-	-	0.67 ± 0.01	2.04 ± 0.01
5	2.95	+ 2.9	- 0.9	0.69 ± 0.01	2.03 ± 0.01
9	2.91	+ 2.9	- 2.5	0.69 ± 0.01	2.00 ± 0.01

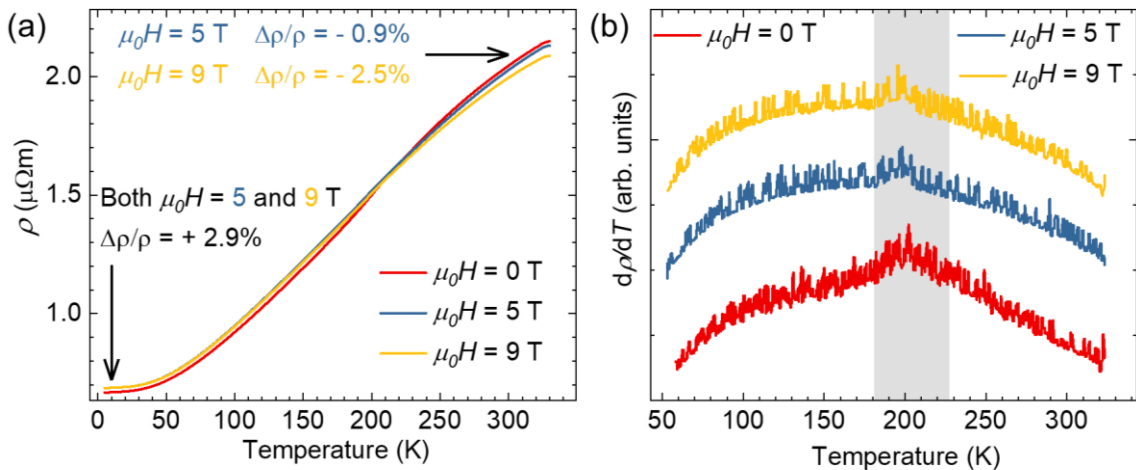


Figure 4.26 (a) Temperature-dependent electrical resistivity ρ measured at $\mu_0H = 0, 5$ and 9 T applied parallel to the film plane. (b) Corresponding derivatives over the temperature.

The field-dependent *MR* measured at $T = 200, 230$ and 300 K is shown in fig. 4.27. In contrast to $(\text{Mo}_{0.5}\text{Mn}_{0.5})_2\text{GaC}$ [95], the *MR* in Mn₂GaC demonstrates a hysteretic behavior revealing an asymmetry with respect to the applied magnetic field direction. The high asymmetric curves are observed for temperatures near the magneto-structural phase transition, albeit at $T = 300$ K the *MR* is more symmetric. At temperatures below T_t (fig. 4.27(a)), the *MR* is irreversible at μ_0H of about 7 T. This asymmetry can result from the magneto-structural transformations that lead to different electronic structures due to a change of the spin configuration. As an illustration, at μ_0H of around +0.8 T (fig. 4.27(a)), the asymmetry of *MR* between the positive and the negative branches reaches the value of 0.9 %. Thoughtfully, at small positive μ_0H , the positive field curve (blue) shows positive *MR*, whereas for the negative field curve (red) the *MR* is negative. This allows the read out of the magneto-structural states at μ_0H below 0.7 T by detecting the sign of the *MR*. The summarized parameters are listed in table 4.4.

AFM aligned moments at $T = 300$ K influence the MR while cooling the system across T_t . At $T = 200$ K, the MR behaves differently if Mn_2GaC was cooled down without μ_0H (green curve in fig. 4.27(a)) and with μ_0H of ± 9 T applied parallel to the film plane. This deviation can be attributed to the different electronic structure as compared to the field induced magnetic configuration stabilized after the application of μ_0H of 9 T and may be caused by a change of the charge carrier concentration and the density of states at the Fermi level. Nevertheless, the contour of the green and the red curves in fig. 4.27(a) is similar indicating that the magneto-structural transformations under the applied magnetic field behave alike. At temperatures above T_t , a complex MR behavior with a modified shape remains and an asymmetry points shift at a higher μ_0H as shown in fig. 4.27(b) - (d). The MR at 9 T is negative and in agreement with the sign change of MR across T_t . At higher temperatures, the irreversibility point decreases down to ~ 3 T, the asymmetry is reduced and the MR evolves mainly towards negative values, being positive and close to zero in μ_0H of ± 2.5 T.

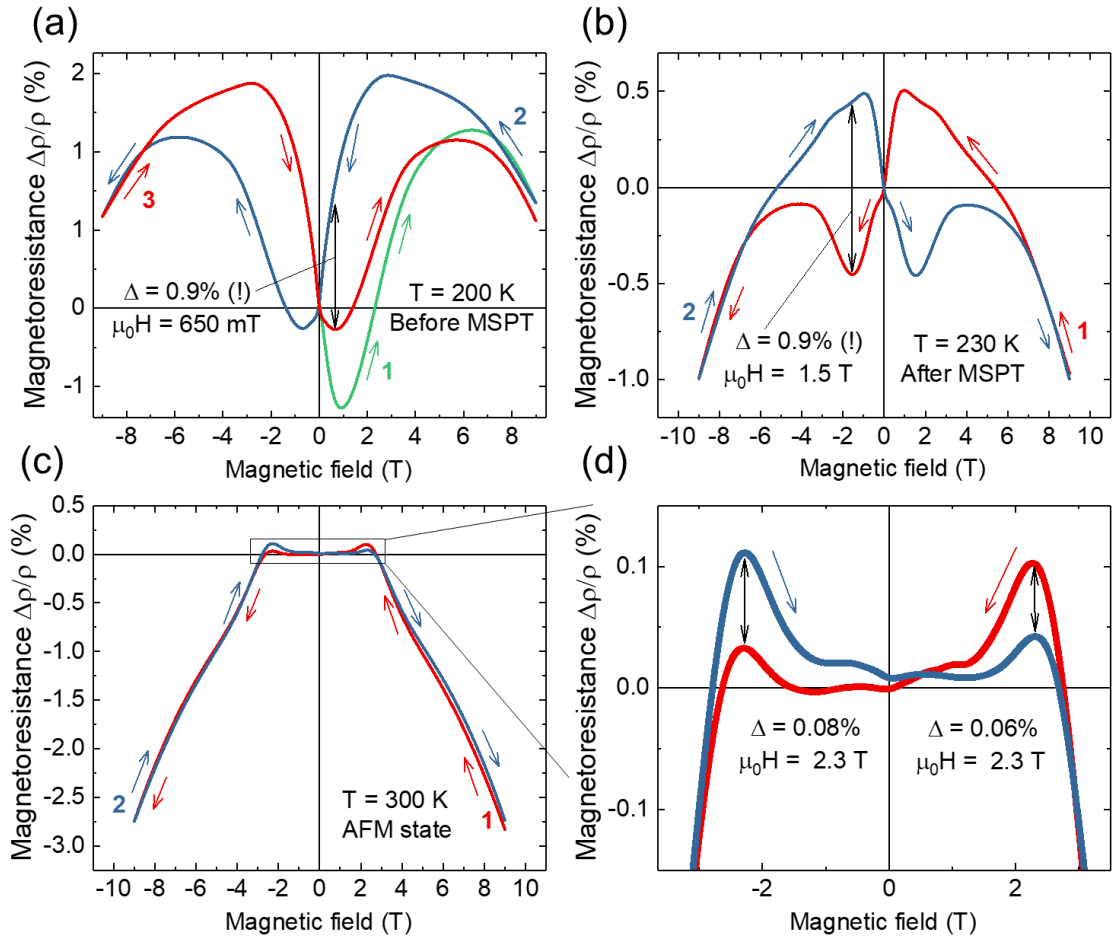


Figure 4.27 Magnetoresistance of the Mn_2GaC film for (a) 200 K, (b) 230 K and (c) 300 K. (d) Magnification of $\mu_0H = \pm 2.5$ T for (c). Arrows represent the sweeping direction and numbers define the measurement order. Adapted from [98].

4.2.4 Magnetic phase transitions

First principles calculations predict strong FM coupling between Mn atoms in Mn-C-Mn layers for Mn_2GaC [40], where the interatomic distance between Mn atoms is 0.267 nm which is below the threshold value of 0.288 nm for the onset of FM exchange observed in many Mn-based compounds with predominant FM coupling [141]. According to performed calculations [40, 41], magnetic states of various spin configurations can have similar equilibrium volumes and formation enthalpies differences. In particular, the difference in formation enthalpy and equilibrium volume between the ground FM state and the energetically lower lying AFM configurations are up to 2 meV/atom and about 0.2 $\text{\AA}^3/\text{formula unit}$, respectively [40, 41]. These results can well describe the observed critical magnetic transition temperature and the volumetric properties of the investigated Mn_2GaC material.

The measurement protocol for the temperature-dependent magnetization $M(T)$, shown in fig. 4.28, included the following steps: first, $M(T)$ of the zero-field-cooled (ZFC) state was measured from 5 to 300 K with an external magnetic field $\mu_0H = 0.2$ T applied parallel to the film plane. Then, without removing the field, the field-cooled (FC) $M(T)$ was measured from 300 to 5 K. As a last step, $M(T)$ was measured on warming the sample back to 300 K (field-warmed: FW). $M(T)$ of the blank substrate was measured separately and subtracted from the film signal (see Appendix, fig. A.1). The pronounced plateau from low temperatures up to about 150 K indicates the presence of long-range magnetic order. The magnetic phase transition occurs at about $T_t = 214$ K. This transition is much sharper than the one observed for $(\text{Cr}_{0.5}\text{Mn}_{0.5})_2\text{GaC}$ (fig. 4.8), where strong mixed interactions are found to be present.

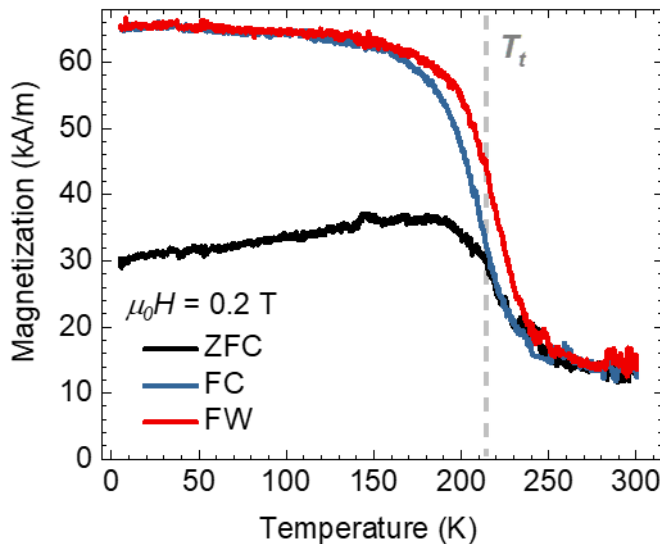


Figure 4.28 Zero-field-cooled (ZFC), field-cooled (FC) and field-warmed (FW) temperature-dependent magnetization $M(T)$ for the 100 nm Mn_2GaC film. Adapted from [98].

The presence of a thermal hysteresis around T_t between FC- and FW- $M(T)$ seen in fig. 4.29 is ascribed to a magneto-structural phase transition, whereas a splitting between ZFC and FC is a response from mixed magnetic interactions [122]. The FC- $M(T)$ is about 57 % larger (at 100 K) than the ZFC- $M(T)$. For the ZFC case, no preferred orientation of the magnetization is provided when cooling through T_t . A preferred orientation is provided when cooled through T_t under an external field so the $M(T)$ is larger than in the ZFC case. At 300 K, the non-zero M is an indication of the presence of a FM contribution arising from magnetic inhomogeneities or impurities. This is further discussed below with regard to the $M(H)$ data. The thermal hysteresis of about 9 K between FC- and FW- $M(T)$ branches denotes the presence of a structural transformation in agreement with reference [40].

We now turn to the high-temperature magnetization measurements. The reason for doing these studies is because Monte Carlo simulations predict an AF-PM magnetic transition for Mn_2GaC at around 660 K [41]. Therefore, we have measured $M(T)$ in the temperature range $300 \leq T \leq 850$ K. The data are shown in fig. 4.29. $M(T)$ was measured in three steps with an applied field of 1 T. First, field-warmed FW- $M(T)$ from 300 to 750 K was measured (1 red). Then, FC- $M(T)$ was measured down to 300 K (2 blue). In the next step, FC- $M(T)$ was measured from 850 K (3 green). The temperature-dependent background from the blank substrate was subtracted. A pronounced peak is observed at 507 K [98] for both red and blue curves with no transition hysteresis. This corresponds to a Néel temperature T_N . The background seen in fig 4.28 is also observed in these data.

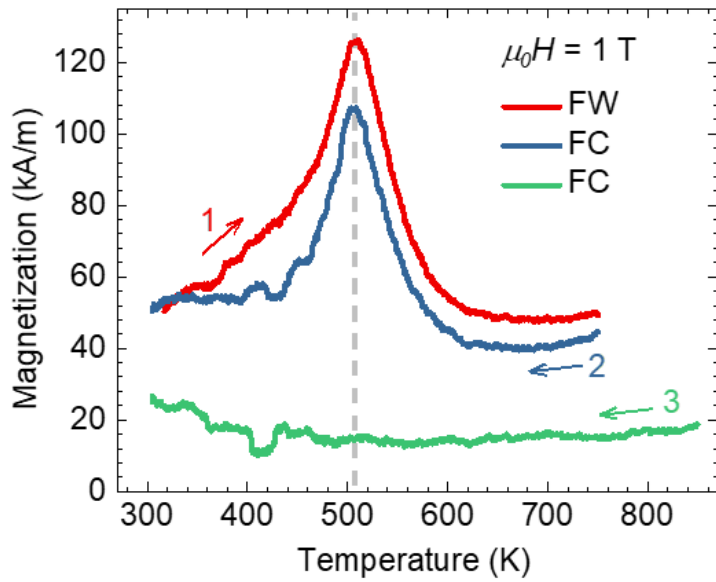


Figure 4.29 Field-warmed (FW) and field-cooled (FC) temperature-dependent magnetization $M(T)$ measured at 1 T applied parallel to the film plane. Adapted from [98].

On the other hand, FC- $M(T)$ measured downwards from 850 K (fig. 4.30) showed an absence of the peak. When brought up to these temperatures, the MAX-phase is no

longer stable, and the system transforms mainly into an antiperovskite Mn_3GaC , as observed in the low-temperature $M(T)$ discussed below. Furthermore, the synthesis of Mn_2GaC is performed at 823 K [24], so that when exceeding this temperature, a decomposition occurs.

The decomposition is reflected as a change in the magnetic properties. To confirm this, we measured ZFC- and FC- $M(T)$ under the same conditions that were used for Mn_2GaC (fig. 4.28). $M(T)$ displays an absence of a magneto-structural phase transition ascribed to the Mn_2GaC magnetic MAX phase [98]. Instead, we find $M(T)$ to exhibit features typical of Mn_3GaC as shown in fig. 4.30. The magnetization is nearly temperature independent for $5 \leq T \leq 160$ K after which it rapidly increases and makes a peak at about 220 K. This corresponds to the AFM-FM transition in Mn_3GaC . The magnetization then decreases as the system goes to a PM state through T_c [145, 146].

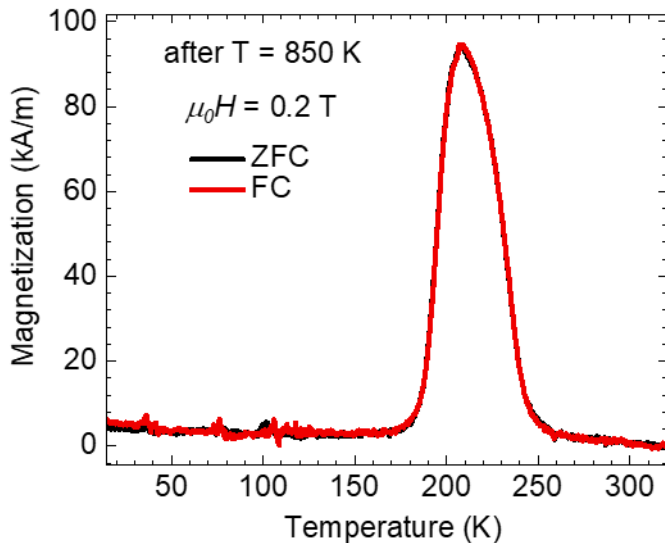


Figure 4.30 Zero-field-cooled (ZFC) and field-cooled (FC) temperature-dependent magnetization for the 100 nm Mn_2GaC film after heating up to 850 K, which does not follow the initial $M(T)$ shown in fig. 4.28.

4.2.5 Field-dependent magnetization and magnetic entropy change

The field-dependent magnetization $M(H)$ measured at temperatures across the magneto-structural phase transition is presented in fig. 4.31. The linear background originating from the substrate (fig. 4.31(a)) was subtracted by a linear fit to $M(H)$ at the highest measuring magnetic fields between 6.5 and 9 T [123, 124]. $M(H)$ for $150 \text{ K} \leq T \leq 300 \text{ K}$ were obtained by normalization with respect to the film volume.

$M(H)$ for many magnetic MAX phase films exhibits a retracing S-shaped curve between the negative and positive maximum field-extremes [23, 26-28, 37, 89, 95]. In contrast to this, for the present sample, $M(H)$ for $T \leq T_c$ do not retrace and show an opening between increasing- and decreasing-field measurements in the first and third quadrants indicating the presence of a metamagnetic transition (fig. 4.31(b)). At these temperatures, the compound is in a non-collinear FM state, and applying a field places

the system into a collinear state. The form of the $M(H)$ curves shown in fig. 4.31(b) is similar for all T except for 300 K. A background arising from magnetic inhomogeneities or impurities discussed in chapter 4.2.4 can also be observed in $M(H)$ as an initial fast rise in small fields, particularly in $M(H)$ for 300 K. The high-field hysteresis narrows with increasing temperature and is no longer present at 300 K (fig. 4.31(b)). The metamagnetic transition is most pronounced at 300 K where the compound is in an AFM state at low fields (fig. 4.31(b)). The transition to the FM state begins at about ± 2 T. The presence of these transitions can be interpreted as a spin reorientation process in an AFM structure beginning at a critical field $\mu_0 H_{cr}$. These features are similar to those observed in spin-flop metamagnetic transitions in AFM materials (e.g. FeCl_2 [147]) when an AFM sublattice abruptly rotates towards the direction of the magnetic field. Its broad shape can be understood to be due to magnetic inhomogeneities arising from competing AFM and FM interactions.

The saturation magnetization M_s was determined to be of 127 kA/m at 9 T for all T within a spread of 5 % with $M(H)$ for 300 K being slightly lower than the other $M(H)$ with M_s of 120 kA/m. The corresponding magnetic moment is estimated to be about $0.3 \mu_B/\text{Mn atom}$. This value is lower than the calculated magnetic moment for the collinear FM configuration, which is 1.6 - 1.8 $\mu_B/\text{Mn atom}$ depending on the calculation method [40]. This points out to a non-collinear alignment of the magnetic moments proposed earlier [24]. The coercive field $\mu_0 H_c$ is about 14 mT for $M(H)$ at all temperatures. The remanent magnetization M_r viewed in the inset of fig. 4.31(b) decreases from 15 to 2 kA/m for 150 and 300 K, respectively.

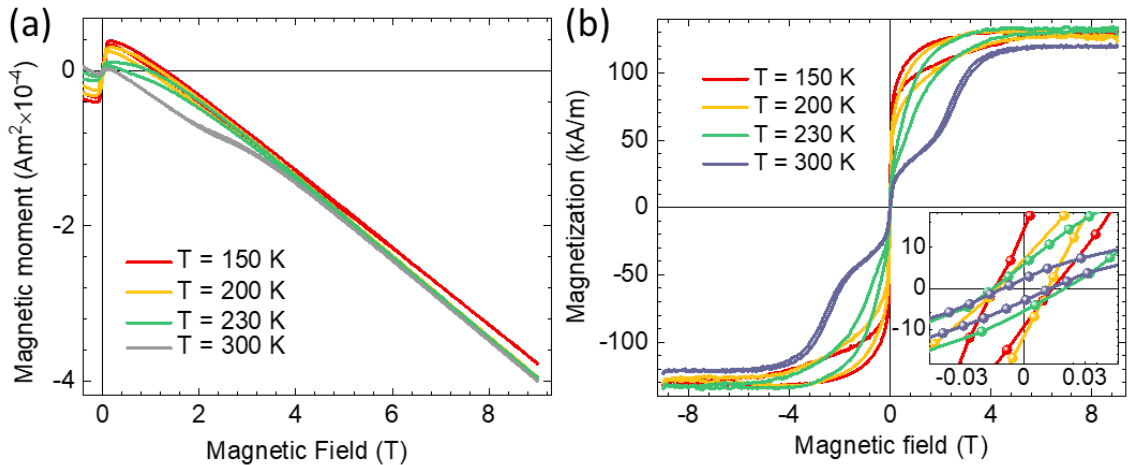


Figure 4.31 (a) Field-dependent magnetic moment for the 100 nm Mn_2GaC film. (b) Field-dependent magnetization for $150 \text{ K} \leq T \leq 300 \text{ K}$ after background subtraction and normalization with respect to the film volume. Inset shows a low-fields area. A magnetic field was applied parallel to the film plane. Adapted from [98].

We now present in fig. 4.32 $M(H)$ for temperatures $500 \leq T \leq 850 \text{ K}$ where the system is above T_N . The background contribution has been subtracted. Although the sample is predominantly in an AFM state below 500 K, the $M(H)$ curves have shapes

that would indicate the presence of FM contributions. This, in fact, persists up to 750 K, which is beyond the region where the peak in $M(T)$ occurs (fig. 4.32). At 850 K, this feature is still present, although the sample is no longer stable as a MAX phase but rather as an antiperovskite as shown in fig. 4.30. M_s for 750 K is about 50 kA/m. This form of saturation attained in small fields is ascribed to the presence of magnetic impurities observed also in figs. 4.28 and 4.29. There is, however, a second source of ferromagnetism which is intrinsic and leads to the observed form of $M(H)$ curves for $500 \leq T \leq 600$ K. This presumably arises due to mixed magnetic interactions prevailing even at these high temperatures. The Mn-C-Mn trilayers in the MAX phase are strongly covalently bound and have been predicted to give rise to FM exchange [40]. This is expected to be the source of the intrinsic magnetic inhomogeneity causing $M(H)$ to approach saturation at higher fields and at a slower rate than in the case for the magnetic impurities. In this field range, none of $M(H)$ reveal a typical linear behavior expected for a pure paramagnetism. One possible model to describe the observed high-temperature $M(H)$ behavior is that above T_t , Mn-C-Mn slabs in Mn_2GaC are still magnetically coupled, but Mn-Ga-Mn layers lose their interlayer coupling. If this model will be proven, then by heating Mn_2GaC above T_t , its layered structure would experience delamination and, thus, M-X-M layers and A interlayers can be partially or fully decoupled.

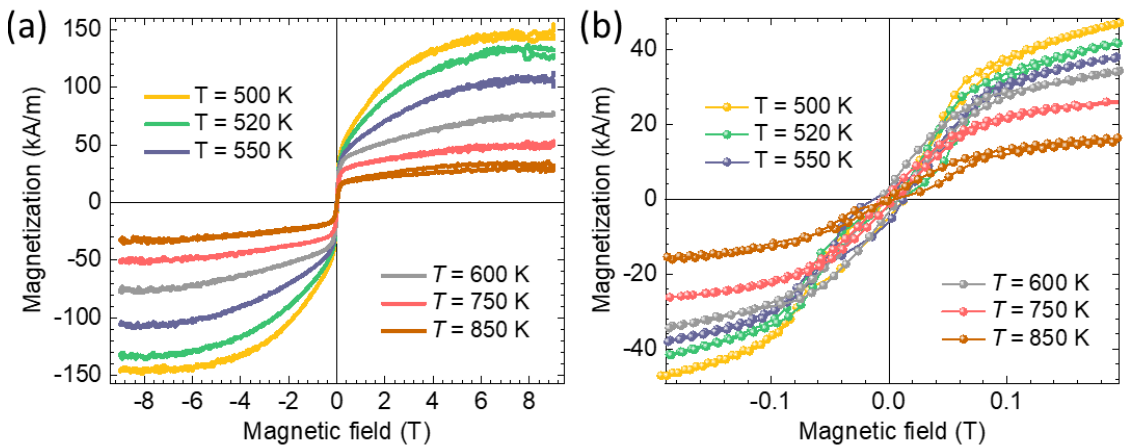


Figure 4.32 (a) Field-dependent magnetization $M(H)$ in the range $500 \text{ K} \leq T \leq 850 \text{ K}$ for the 100 nm Mn_2GaC film with the magnetic field applied in the film plane. (b) Low-fields area. Data were normalized with respect to the film volume and are presented after background subtraction.

Magneto-structural transitions in Mn-based Heusler alloys and antiperovskite compounds lead to magnetocaloric effects (MCE). MCE are characterized by a release or absorption of energy (heat) when a field is applied [47, 56]. This effect is widely studied due to its high potential for magnetic energy conversion applications and magnetic refrigeration [56, 57]. Due to a fact that Mn_2GaC exhibits a magneto-structural transformation (fig. 4.33), we examined the entropy change ΔS in the

vicinity of T_t (fig. 4.33(b)) to understand whether magnetic MAX-phase materials can be useful for MCE applications [98].

Isothermal $M(H)$ shown in fig. 4.33(a) were recorded in the temperature range $150 \leq T \leq 340$ K with a magnetic field from 0 to 9 T having the speed rate of 0.01 T/s. A magnetic field was applied parallel to the film plane for all presented measurements. Before each $M(H)$, the sample was zero-field-cooled from 300 K to the measuring temperature. To obtain ΔS , an integration was executed according to eq. 2.10 for the field ranges of $0 \leq \mu_0 H \leq 0.5$ T, $0 \leq \mu_0 H \leq 1.0$ T, and $0 \leq \mu_0 H \leq 2.0$ T (fig. 4.33). The largest ΔS is observed near T_t (fig. 4.33(b)). ΔS is negative, which is a typical response for materials with high magnetization states at lower temperatures [57]. An unpronounced ΔS observed for Mn_2GaC is a consequence of a broad phase transition (fig. 4.28) with a width of about 60 K and competing magnetic interactions [98]. $|\Delta S|$ shows a maximum at 0.26 and 0.44 J/kgK for the field ranges of $0 \leq \mu_0 H \leq 1.0$ T and $0 \leq \mu_0 H \leq 2.0$ T, respectively. These values are about one order of magnitude smaller than in compounds with a substantial MCE. For instance, the well-known magnetocaloric materials Mn_3GaC and $\text{La}_{0.83}\text{Sr}_{0.17}\text{MnO}_3$ exhibit a ΔS at 2 T of about 14 J/kgK [57] and 3.5 J/kgK [148].

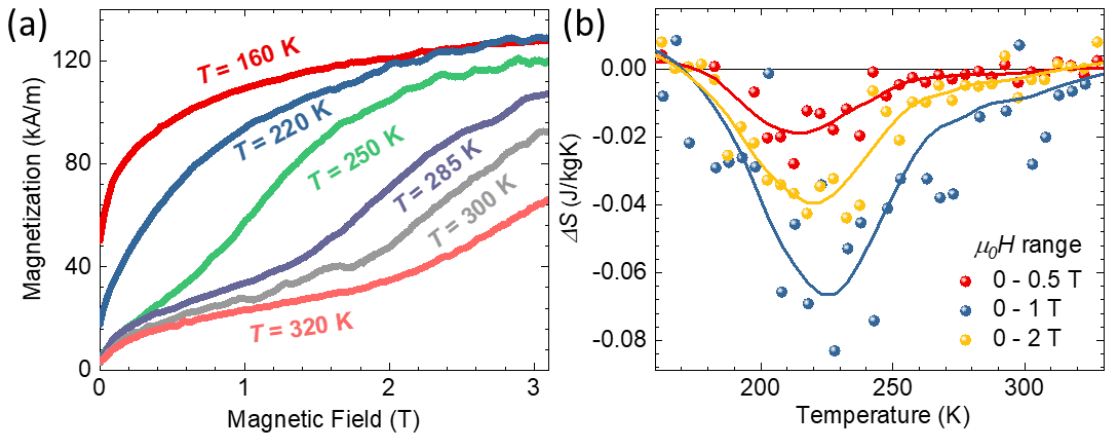


Figure 4.33 (a) Isothermal magnetization curves for the 100 nm Mn_2GaC film measured from 150 K to 340 K with 5 K step. (b) Temperature-dependent entropy change ΔS for applied magnetic fields in the range of 0 - 0.5, 0 - 1.0 and 0 - 2.0 T. Solid lines are guides for the eye [98].

To make magnetic MAX phases competitive in the MCE, a high magnetization and an abrupt magnetic phase transition are required [57]. Despite the fact that the Mn_2GaC film does not show any substantial MCE, MAX phases offer multi-faceted possibilities to tailor material properties via element-substitution on the M , A or X sites [11]. This opens a wide venue to tune magnetic properties like MCE to obtain a desired response. From this perspective, the appearance of MCE in Mn_2GaC can be a source of motivation for the further development of other magnetic MAX phases with magneto-structural transitions.

4.2.6 Angular- and frequency-dependent ferromagnetic resonance

An experimental setup based on a microwave short was used to study FMR in the frequency range $6 \text{ GHz} \leq f \leq 18 \text{ GHz}$, details are given in chapter 3.2.3. The sensitivity of this configuration is lower than of a resonant cavity-based setup, which resulted in recorded signals of smaller amplitude. The film specimen was cooled down from 300 to 100 K. A 9 T field was applied prior to measurements. Each $\partial\chi''/\partial H$ spectrum was recorded in the field range $0 \text{ T} \leq \mu_0 H \leq 0.5 \text{ T}$ starting from higher fields to ensure equal conditions of a magnetic moment's alignment along the applied field. A magnetic field was applied parallel to the film plane. An FMR signal for the *out-of-plane* configuration was not detected as the signal smears out while approaching the perpendicular orientation, which is shown below in fig. 4.38. Experimental FMR spectra for the zero-field-cooled (ZFC_{9T}) and field-cooled (FC_{9T}) protocols measured at 100 K are presented in figs. 4.34(a) – (b).

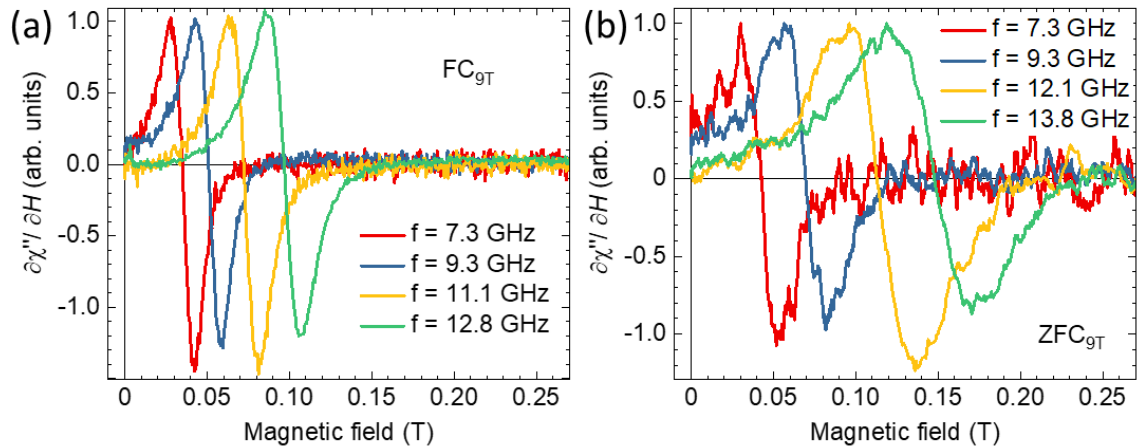


Figure 4.34 Absorption derivatives measured at 100 K for the Mn₂GaC film for the (a) field-cooled (FC_{9T}) and (b) zero-field-cooled (ZFC_{9T}) protocols at different frequencies. Measurements were performed with a magnetic field applied parallel to the film plane.

The frequency-dependent resonance field $\mu_0 H_r$ and linewidth $\mu_0 \Delta H$ for both ZFC_{9T} and FC_{9T} are shown in figs. 4.35(a) and (b), respectively. The experimental data for $\mu_0 H_r$ were fitted according to eq. 2.30 for the *in-plane* configuration to determine a *g*-factor and a perpendicular magnetic anisotropy constant $K_{2\perp}$. For all fits, $M_s = 127 \text{ kA/m}$ from $M(H)$ curves was used. The quality of the fit appeared to be similar for fixed *g* factor within the range of $1.9 \leq g \leq 2.2$, despite the data were taken at the wide frequency range of $6 \text{ GHz} \leq f \leq 18 \text{ GHz}$.

The obtained $K_{2\perp}$ of the ZFC_{9T} and FC_{9T} protocols for $1.9 \leq g \leq 2.2$ were found to be negative with $-100 \text{ kJ/m}^3 \leq K_{2\perp} \leq -67 \text{ kJ/m}^3$ and $-135 \text{ kJ/m}^3 \leq K_{2\perp} \leq -97 \text{ kJ/m}^3$, respectively. It becomes clear that from this experimental data one cannot distinguish a difference in a *g*-factor for the ZFC_{9T} and FC_{9T} protocols. However, $K_{2\perp}$ for FC_{9T} showed a magnitude, which is about 40 % bigger than it was observed for ZFC_{9T}. $\mu_0 \Delta H$

exhibits a nonlinear dependence with a tendency to saturate at low frequencies, which point out to additional contributions to the two main mechanisms that define the relaxation rate of M , which are the intrinsic damping and the inhomogeneous line broadening [60]. In order to specify possible contributions to a model for a frequency-dependent $\mu_0\Delta H$, experimental data for a wider f range are required.

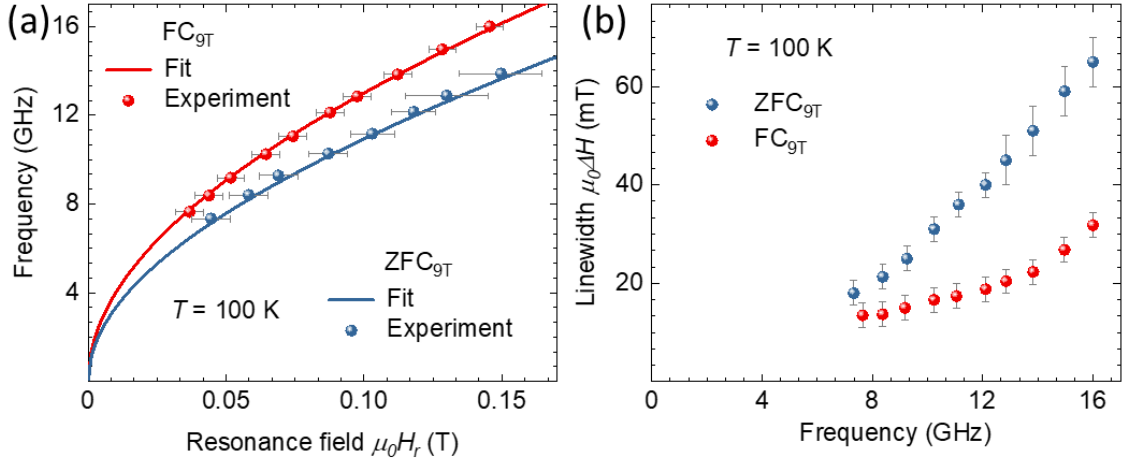


Figure 4.35 (a) Frequency-dependent resonance field $\mu_0 H_r$ and (b) linewidth $\mu_0\Delta H$ for the zero-field-cooled (ZFC_{9T}) and field-cooled (FC_{9T}) protocols. Measurements were performed at 100 K with an external magnetic field applied in the film plane.

As it was shown above, the resonance signal related to the Mn₂GaC film appears at fields below those that are characteristic for the electron paramagnetic resonance (EPR). The second signal was observed at higher fields and it was ascribed to an overmodulated sharp resonances from inclusions incorporated into the MgO substrate. Extracted $\mu_0 H_r$ and $\mu_0\Delta H$ for both ZFC_{9T} and FC_{9T} are shown in figs. 4.36(a) and (b), respectively. These resonances were observed for all films deposited on MgO and they are presented in the inset of fig. 3.9.

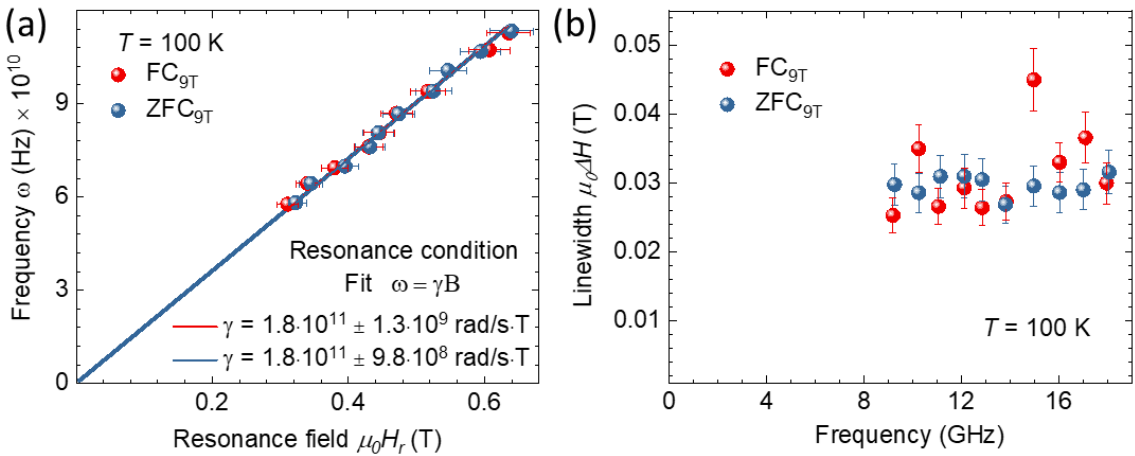


Figure 4.36 Frequency-dependent absorption derivative for the MgO substrate measured at 100 K. (a) Frequency-dependent resonance field $\mu_0 H_r$ with the fit according to the EPR resonance condition and (b) linewidth $\mu_0\Delta H$ for the zero-field-cooled (ZFC_{9T}) and field-cooled (FC_{9T}) protocols.

To confirm its EPR nature, the resonance condition for EPR shown in fig. 4.36 was used. According to this equation, EPR exhibits a linear frequency dependence. For $f = 9.4$ GHz, $\mu_0 H_r$ should appear at fields of about 345 mT assuming the free electron $g = 2.0023$ [149]. Experimental $\mu_0 \Delta H$ is found to be frequency independent, which is an additional hint to a non-FM origin of this resonance. Both quantities are independent on cooling protocol and, thus, we can conclude that they are not related to the FMR signal of Mn₂GaC.

A magnetic anisotropy with respect to the sample orientation was studied using the same principles described in chapters 3.2.3 and 4.1.3. FMR measurements were performed for the ZFC protocol at 110 K, where the system is in a noncollinear state. For the *in-plane* azimuthal angle φ rotation, we have measured microwave absorption derivative spectra $\partial \chi'' / \partial H$ for the angular range $0^\circ \leq \varphi \leq 358^\circ$ with 2° steps. Measurements were performed at $f = 9.47$ GHz with the modulation frequency of 100 kHz. The microwave power was adjusted to 19.7 mW, and the modulation amplitude to 0.3 mT. The quality factor Q was determined to be 1600 and 6200 for the *in-plane* and the *out-of-plane* configuration, respectively. The time constant and the conversion time on Lock-In were set to 20 ms and 40 ms, respectively.

An *in-plane* angular dependence for the Mn₂GaC film is anticipated to demonstrate a six-fold symmetry as for the (Cr_{0.5}Mn_{0.5})₂GaC films discussed in chapter 4.1.3, since both compounds exhibit a hexagonal crystal structure with the *c*-axis normal to the film plane [24, 98]. Also, a substrate roughness, domains or tilted grains can result in a summarized contribution, which is generally observed as a uniaxial magnetic anisotropy [75, 125, 138, 150]. Four $\partial \chi'' / \partial H$ spectra measured at distinct angles that correspond to the observed easy- and hard-axes for 110 K are presented in fig. 4.37(a). It can be seen in the inset in fig. 4.37(a), that an amplitude of substrate signals is much larger than for the FMR signal of Mn₂GaC. This effect is the result of a quality factor reduction occurring when a massive sample (substrate in this case) is placed across the resonant cavity, which disturbs the electrical field distribution while a sample rotates. An angular-dependent zero-field absorption is as well ascribed to the above-mentioned technical point.

The single FMR signal originating from the Mn₂GaC film is located at the magnetic field of about 94 mT for 110 K. The lineshape deviates from a symmetric Lorentzian derivative function expected for typical FMR signals for a metallic FM film [60]. The extracted $\mu_0 H_r$ and $\mu_0 \Delta H$ are presented in fig. 4.37(b). The sample showed a weak uniaxial character for both $\mu_0 H_r$ and $\mu_0 \Delta H$ with minima/maxima at every 90° . We note that the difference between the $\mu_0 H_r$ maxima at 90° and 270° is about 3 mT, which is small considering the error of the $\mu_0 H_r$ determination due to a high noise of the signal. On another hand, a similar asymmetry of the *in-plane* magnetic anisotropy was reported for NiFe/FeMn/CoFe trilayers that contain FM-AFM interfaces and exhibit an exchange bias [151]. In this reference, unidirectional and uniaxial magnetic anisotropies were found to be misaligned in the film plane, which resulted in an

angular dependence with unequal magnitude of maxima. A noncollinearity between these magnetic anisotropies was ascribed to a combination of a small *in-plane* magnetic anisotropy and magnetic frustration effects arising from yet inevitable structural imperfections such as roughness, defects, mosaicity, strain, and so forth [151]. The above-mentioned explanation may describe the observed angular dependence, since Mn_2GaC revealed a noncollinear magnetic configuration with competing AFM-FM interactions [41], a small *in-plane* magnetic anisotropy and structural inhomogeneities such as grains [24]. However, no exchange bias effects were detected for the Mn_2GaC film (e.g., chapter 4.2.5), which is an important contribution for the observation of a unidirectional magnetic response [151].

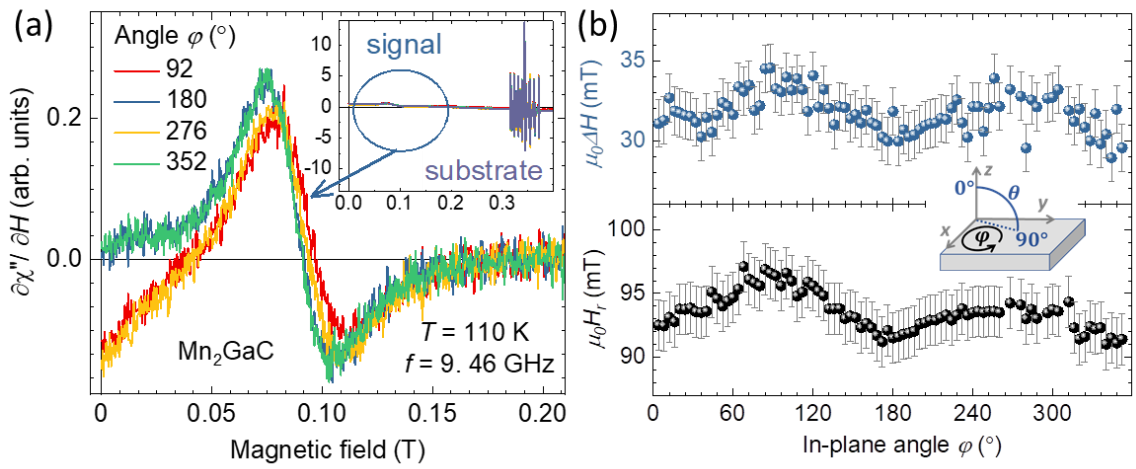


Figure 4.37 (a) Absorption derivatives for the Mn_2GaC film on the MgO substrate measured at 110 K for angles $92^\circ \leq \varphi \leq 352^\circ$. The inset demonstrates a relative ratio between signals from the substrate and the film. (b) The linewidth $\mu_0\Delta H$ and the resonance position μ_0H_r as a function of angle.

The variation of $\mu_0\Delta H$ between 0.030 and 0.035 T, shown in fig. 4.37(b) follows the μ_0H_r shift displaying minima and maxima at the same positions. It should be noted that the difference between minimum and maximum of about 5 mT is small taking into account the error in the $\mu_0\Delta H$ determination. A uniaxial character of the $\mu_0\Delta H$ angular dependence may be interpreted to be a result of contributions dominating over the intrinsic line broadening, which are related to an anisotropy distribution in the film plane caused by inhomogeneities and competing magnetic interactions.

Angular-dependent FMR studies for the *out-of-plane* configuration have been performed for $\text{ZFC}_{1.2\text{T}}$ and $\text{FC}_{1.2\text{T}}$ at 110 K with 2° steps and 0.5° near the *out-of-plane* orientation of the film specimen. For each microwave absorption derivative $\partial\chi''/\partial H$, the magnetic field was swept from high fields to zero. $\partial\chi''/\partial H$ were recorded at $f = 9.43\text{ GHz}$, the modulation frequency of 100 kHz , the microwave power was set to 19.7 mW . The quality factor was $Q = 5600$, the time constant and conversion time on a Lock-In amplifier were optimized to 20 and 40 ms , respectively. $\partial\chi''/\partial H$ for both $\text{ZFC}_{1.2\text{T}}$ and $\text{FC}_{1.2\text{T}}$ are presented in figs. 4.38(a) – (b). A small absorption signal observed at 0.02 T in fig. 4.38(a) is found to be angular-independent. For the $\text{FC}_{1.2\text{T}}$, it

is suppressed by a strong FMR signal. Qualitatively, signals for the $\text{FC}_{1.2\text{T}}$ protocol are located at lower fields and have much higher amplitude than for $\text{ZFC}_{1.2\text{T}}$. Primarily, it could mean a larger M and a resulting stronger magnetic anisotropy contribution. Asymmetries of the FMR signals are comparable for both protocols.

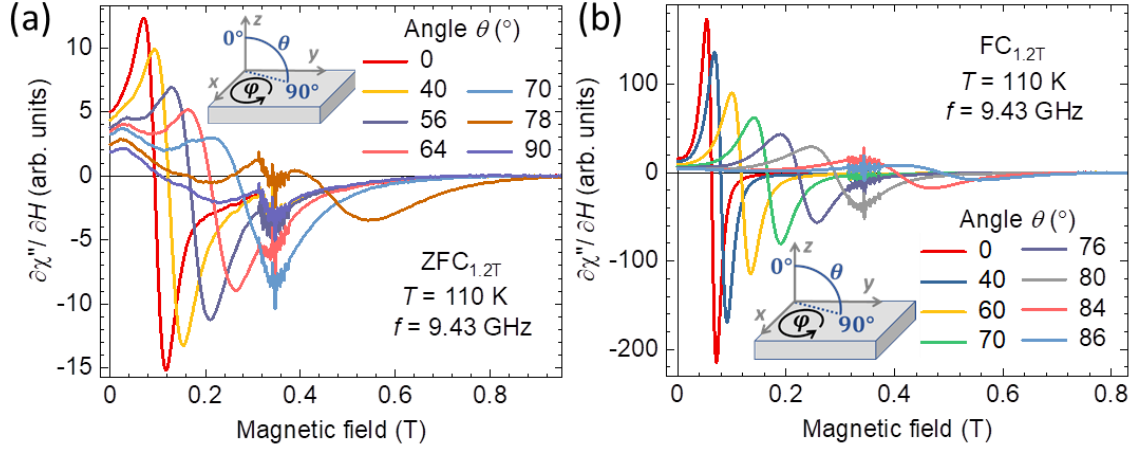


Figure 4.38 Angular-dependent absorption derivatives for the Mn_2GaC film measured at 110 K for the (a) zero-field-cooled ($\text{ZFC}_{1.2\text{T}}$) and (b) field-cooled ($\text{FC}_{1.2\text{T}}$) protocols. Insets show a schematic of the angle rotation.

Approaching an *out-of-plane* orientation, the FMR signal broadens out for both $\text{ZFC}_{1.2\text{T}}$ and $\text{FC}_{1.2\text{T}}$. Extracted μ_0H_r and $\mu_0\Delta H$ are presented in figs. 4.39(a) – (b). The angular-dependent μ_0H_r requires both *in-plane* and *out-of-plane* values to calculate the perpendicular magnetic anisotropy associated with an obtained curvature. However, for an exact position of $\theta = 0^\circ$ (see angles in fig. 4.39(d)), no data were extracted as the signal moves towards fields that are higher than the highest achieved field of 1.2 T. Obtained data sets were fitted by the Smit-Beljers approach described in chapter 3.2.3 and [115] to evaluate the magnetic anisotropy for these cooling protocols and justify the difference seen in μ_0H_r and $\mu_0\Delta H$. Extracted data regarding μ_0H_r and $\mu_0\Delta H$ are presented in figs. 4.39(a) – (c). Figs. 4.39(a) and (b) represent two approaches of the magnetization description within the free energy model. Conventional magnetization model is the one which is typically used for FM materials [60]. Based on experimental $M(H)$ curves given in literature showing much bigger amplitude of M for the *in-plane* orientation with respect to an applied magnetic field than for the *out-of-plane* (at this configuration almost no FM component can be seen) [24], an effective canting angle θ_{eff} to the M definition was introduced, which simulates this behavior reducing M while approaching the *out-of-plane* configuration from the *in-plane*. The best fits for both models are presented in figs. 4.39(a) and (b), and corresponding parameters are summarized in table 4.5. The conventional model describes the whole landscape, but it cannot perform a fit for 0° orientation, giving much high values of μ_0H_r than the experimental ones. In contrast, fig. 4.39(b) shows a better fit for 0° assuming the model with θ_{eff} . The conventional model shows that there is a substantial difference for $K_{2\perp}$.

obtained for the $ZFC_{1.2T}$ and $ZFC_{1.2T}$ protocols. In contrast, by introducing θ_{eff} , magnitudes become nearly the same for both protocols. θ_{eff} is smaller for $FC_{1.2T}$, which can be understood in a way that M is better aligned. This outcome correlates with experimental data, e.g. $M(H)$ shown in fig. 4.40, where by cooling the system under an applied magnetic field and by measuring at fields up to 1.2 T, it changes its magnetization by 56 %. However, a theoretical modeling is required to justify values obtained from the fit.

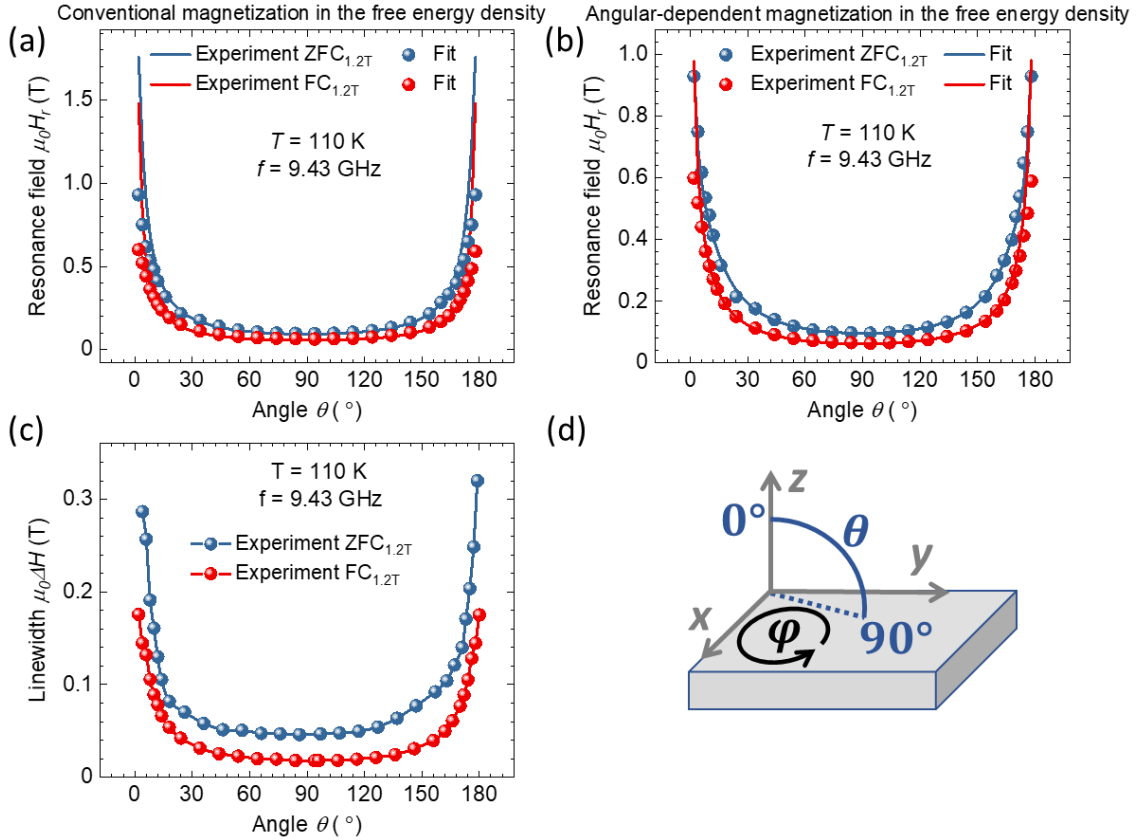


Figure 4.39 Angular-dependent resonance field $\mu_0 H_r$ for the zero-field-cooled ($ZFC_{1.2T}$) and field-cooled ($FC_{1.2T}$) protocols along with the fits by the Smit-Beljers approach using (a) a standard description of the magnetization M and (b) an implemented effective canting angle of M . (c) Angular-dependent linewidth $\mu_0 \Delta H$ for the same protocols. (d) Rotation of angles for a film specimen.

The angular-dependent $\mu_0 \Delta H$ demonstrates a maximum for the *out-of-plane* configuration, which can be explained by a larger distribution of local magnetic anisotropies. It is reasonable to assume, since the Mn₂GaC film exhibits lateral grains of about 400 nm [24], so that the shape anisotropy pushes magnetic moments to be aligned in the film plane, but once an applied field rotated to the *out-of-plane*, then each local inhomogeneous entity (e.g. grain) may have its own favorable orientation *in-plane*. $\mu_0 \Delta H$ for the $ZFC_{1.2T}$ protocol exhibit a larger change than the one for the $FC_{1.2T}$, which could be a measure of a lower magnetic homogeneity. In this regard, it would be useful to observe how an applied magnetic field during a cooling procedure can influence the domain structure.

Table 4.5 A perpendicular magnetic anisotropy constant $K_{2\perp}$ and effective canting angle θ_{eff} of the magnetization obtained from fits to an angular-dependent resonance field for the zero-field-cooled (ZFC_{1.2T}) and field-cooled (FC_{1.2T}) protocols by the Smit-Beljers approach with a conventional or angular-dependent M term.

Protocol	Fit	$K_{2\perp}$, kJ/m ³	θ_{eff} , °
ZFC _{1.2T}	Conventional M	- 61.4	-
ZFC _{1.2T}	Angular-dependent M	- 61.7	23
FC _{1.2T}	Conventional M	- 115.5	-
FC _{1.2T}	Angular-dependent M	- 61.3	0.2

The magnetic MAX phase film Mn₂GaC was investigated by means of FMR. At 110 K, an assumed noncollinear AFM state with a canting angle provides a description of the free energy landscape obtained by an angular-dependent $\mu_0 H_r$. A presence of a canting nature of different magnitude can be considered, since the intensity of the microwave absorption derivative (that is proportional to the total M of the sample [60]) appeared to be significantly smaller for the ZFC_{1.2T} protocol than for FC_{1.2T}. A relative comparison of these intensities can be performed, because the measurements were performed one after another on the same sample. It was shown that a cooling with an external magnetic field stabilizes a magnetic configuration with a higher homogeneity, which can be a result of a different canting angle chosen by the compound to minimize its energy. The change of $\mu_0 \Delta H$ towards smaller values as well as lower $\mu_0 H_r$ supports this statement. As another option, it can be assumed that the Mn₂GaC possesses more fan-like magnetic structure [40]. It can be understood as via the external magnetic field an additional energy is delivered to the system, which makes frustrated magnetic moments favor to be cooperatively aligned along the external magnetic field.

4.2.7 Temperature-dependent ferromagnetic resonance

In chapter 4.2.4, the presence of competing magnetic interactions was discussed with respect to the observed difference between ZFC- and FC- $M(T)$. Therefore, at low fields, such a mixed magnetism is anticipated to be reflected in a magnetic history-dependent $M(H)$. In order to correlate magnetometry and FMR studies, $M(H)$ shown in figs. 4.40(a) – (d) were measured for ZFC and FC protocols at magnetic fields that were used for FMR studies. First, ZFC- $M(H)$ were measured at 100 K within the range of ± 1.2 and ± 9.0 T (fig. 4.40), which are denoted as ZFC_{1.2T} and ZFC_{9T}. A demagnetization sequence was carried out at 310 K before cooling to ensure the same initial state at 100 K. Afterwards, FC- $M(H)$ at 100 K were obtained by cooling the sample from 310 K through T_t under $+ 1.2$ and $+ 9.0$ T (fig. 4.40). These $M(H)$ are denoted as FC_{1.2T} and FC_{9T}.

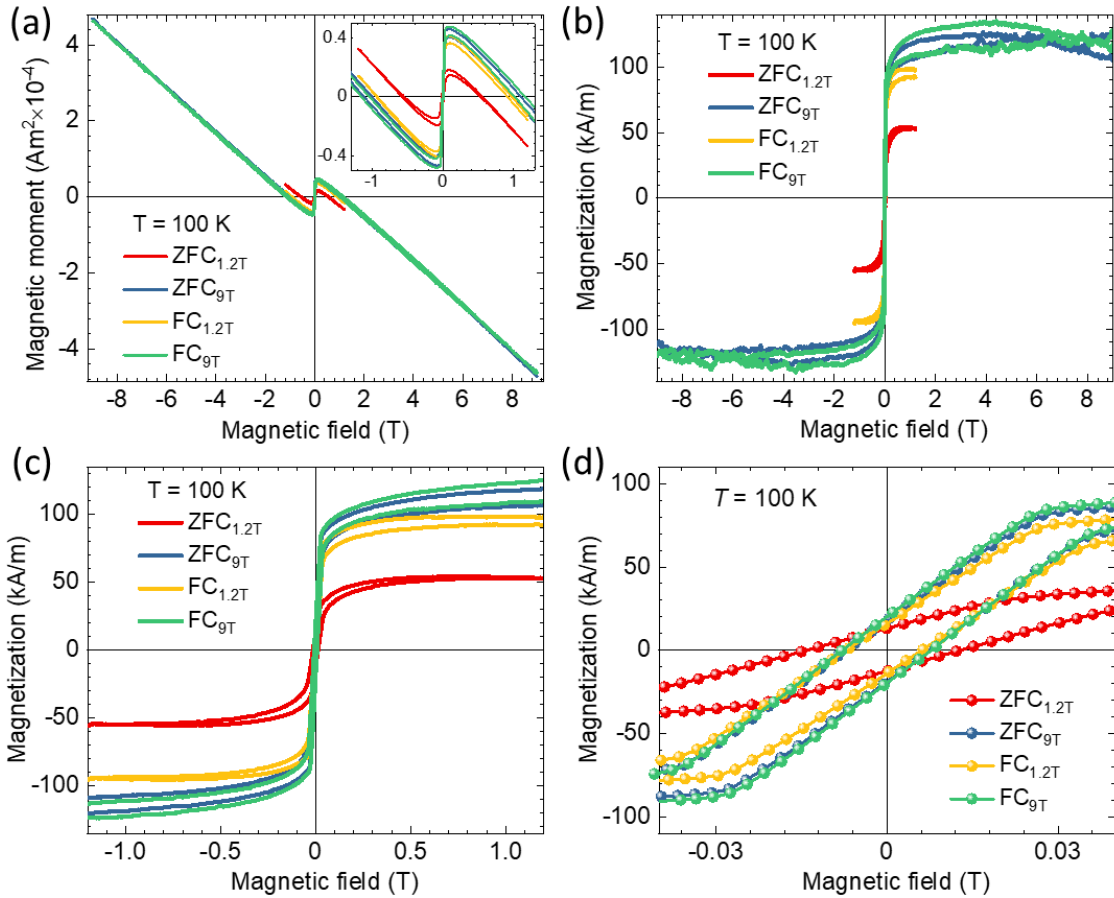


Figure 4.40 (a) Raw field-dependent magnetic moment for the 100 nm Mn_2GaC film. (b) Field-dependent magnetization after background subtraction and normalization with respect to the film volume. (c) and (d) represent magnified fields of ± 1.2 and $\pm 0.04 \text{ T}$. Measurements were performed with a magnetic field applied parallel to the film plane following the zero-field-cooled (ZFC) and field-cooled (FC) protocols. The field in the underscore (e.g. $\text{ZFC}_{1.2\text{T}}$) defines a measuring field range and magnitude of the field while cooling for the FC case.

The non-retracing character of $M(H)$ for all above mentioned protocols seen in fig. 4.40(c) indicates the presence of intrinsic metamagnetic transformations. $M(H)$ for $\text{ZFC}_{1.2\text{T}}$ returns to the starting point at 1.2 T whereas $M(H)$ for $\text{FC}_{1.2\text{T}}$ does not. $\text{ZFC}_{9\text{T}}$ and $\text{FC}_{9\text{T}}$ show an identical behavior but they do not coincide at 1.2 T. This difference can be understood to be related to field-induced irreversible effects that occur while cooling the system under an applied magnetic field. At 1.2 T, the magnetization $M_{1.2\text{T}}$ is 54 kA/m for the $\text{ZFC}_{1.2\text{T}}$ case which is about 56 % of 96 kA/m obtained for $\text{FC}_{1.2\text{T}}$. For 9 T, $M_{9\text{T}}$ is 122 kA/m on the descending $M(H)$ and 109 kA/m on the ascending $M(H)$ branches for both $\text{ZFC}_{9\text{T}}$ and $\text{FC}_{9\text{T}}$, so that there is nearly no difference when compared to the $\text{FC}_{1.2\text{T}}$ case. The low-fields area is magnified in fig. 4.40(b), where a coercive field $\mu_0 H_c$ of 13 mT can be observed for $\text{ZFC}_{1.2\text{T}}$, whereas for the other protocols it is of 7 mT. This 75 % increase of $\mu_0 H_c$ together with the 56 % reduction of $\text{ZFC}-M_{1.2\text{T}}$ can be associated with a strong magnetic frustration in the system. An applied magnetic field of 1.2 T is not high enough to align the magnetic moments at 100 K. On another hand,

$\text{FC}_{1.2\text{T}}$ has reached about 78 % of the obtained M values for $\text{ZFC}_{9\text{T}}$. It appears that when cooling across the magneto-structural phase transition under a small applied field of 1.2 T, most of the magnetic moments align along the field direction.

These cooling protocols $\text{ZFC}_{1.2\text{T}}$ and $\text{FC}_{1.2\text{T}}$ were repeated for FMR studies to observe an influence on dynamic magnetic properties for Mn_2GaC , since different M and μ_0H_c should reflect on the FMR line evolution. Temperature-dependent FMR spectra for $140 \text{ K} \leq T \leq 230 \text{ K}$ measured for $\text{ZFC}_{1.2\text{T}}$ and $\text{FC}_{1.2\text{T}}$ cases are shown in figs. 4.41(a) and (b), respectively, as a field derivative of the imaginary part of the high frequency susceptibility tensor over an applied magnetic field. Technical parameters included the measuring frequency $f = 9.46 \text{ GHz}$ with the modulation frequency of 100 kHz. The microwave power was adjusted to 19.7 mW, the field modulation amplitude to $\Delta_B = 1.5 \text{ mT}$, and the quality factor Q was determined to be 3700. The time constant and conversion time on Lock-In amplifier were set to 20 ms and 40 ms, respectively.

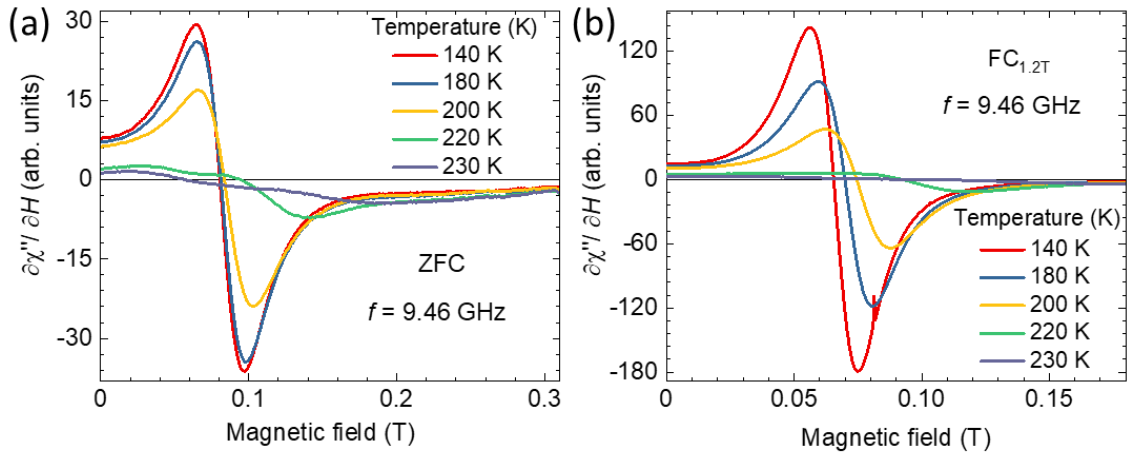


Figure 4.41 Ferromagnetic resonance spectra for the Mn_2GaC film measured in the range of $140 \text{ K} \leq T \leq 230 \text{ K}$ with a magnetic field of 1.2 T applied parallel to the film plane for the (a) zero-field-cooled (ZFC) and (b) field-cooled ($\text{FC}_{1.2\text{T}}$) protocols.

Figs. 4.41(a) and (b) show field-dependent FMR signals that were observed for both $\text{ZFC}_{1.2\text{T}}$ and $\text{FC}_{1.2\text{T}}$. With increasing temperature, both signals move towards higher fields experiencing a line broadening and intensity reduction. In fig. 4.41(a), at low fields of about 0.02 T, the left part of an additional subtle resonance is visible. This signal was observed for temperatures above 220 K for both $\text{ZFC}_{1.2\text{T}}$ and $\text{FC}_{1.2\text{T}}$. Its μ_0H_r and $\mu_0\Delta H$ were not evaluated since the right part of the signal and the resonance position are obstructed by the dominant FMR signal. Nevertheless, we note that the signal slightly moves to lower fields between 220 and 230 K, while for $230 \text{ K} \leq T \leq 245 \text{ K}$ it is constant. One option is that this low-field resonance signal could be associated with minor traces of an Mn_3GaC phase reported for the Mn_2GaC film [24]. However, μ_0H_r for the bulk Mn_3GaC was found to be at much higher field of 0.29 T for 170 K [152]. Therefore, this resonance signal does not originate from bulk Mn_3GaC .

ZFC- and FC-FMR signals are demonstrated in figs. 4.42(a) - (b) for 140 and 220 K that are across T_t . Blue colored curves show ZFC-FMR signals, while for FC measurements the FMR lines are red. The relative intensity of the FC-FMR signal is higher than for the ZFC case since the system is not saturated at 1.2 T, which is consistent to $M(H)$ curves shown in fig. 4.40. At 140 K, both FMR signals exhibit well defined lineshape, while at 220 K, they are broader with a distorted asymmetric lineshape. At 140 K, μ_0H_r for the ZFC is about 0.015 T larger than for the FC case, and $\mu_0\Delta H$ is found to be about 0.013 T smaller for the FC than for the ZFC case. This behavior indicates that the Mn₂GaC film exhibits a higher magnetic homogeneity when cooling across T_t with an applied magnetic field.

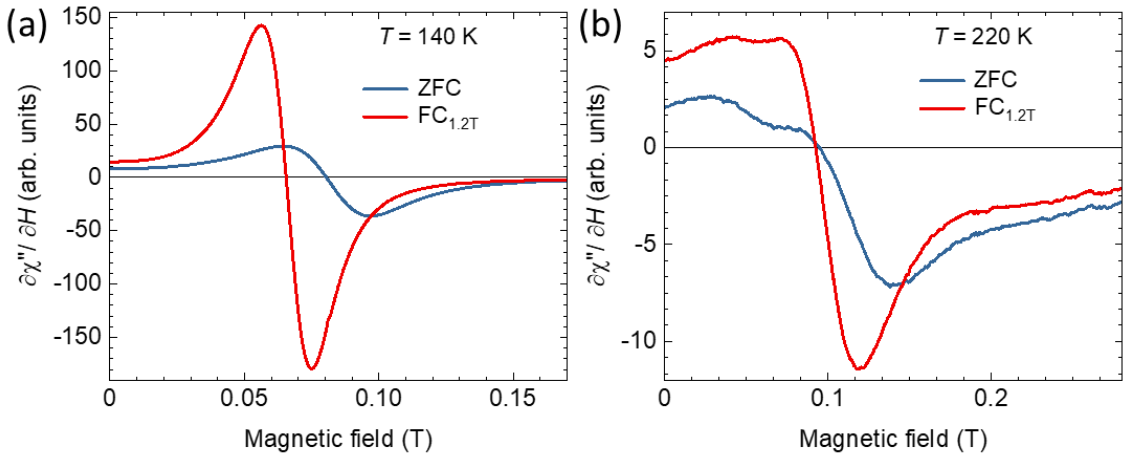


Figure 4.42 Ferromagnetic resonance spectra measured for the Mn₂GaC film at (a) 140 K and (b) 220 K, which are below and above the magneto-structural phase transition (fig. 4.28). Data represent the zero-field-cooled (ZFC) and field-cooled at 1.2 T (FC_{1.2T}) protocols with a magnetic field applied parallel to the film plane.

Extracted μ_0H_r and $\mu_0\Delta H$ as a function of temperature are shown in fig. 4.43. Below 200 K, where the system is presumably in a noncollinear magnetic state, the μ_0H_r change between 120 and 180 K is 0.002 T and 0.007 T for the ZFC and FC cases, respectively. For the same temperature range, $\mu_0\Delta H$ changes by 0.001 T and 0.003 T for ZFC and FC case, respectively. Thus, the system exhibits a plateau with minor changes in μ_0H_r and $\mu_0\Delta H$. On the other hand, both quantities experience major changes across the magneto-structural phase transition above 200 K. For example, at 200 K $\leq T \leq$ 245 K, μ_0H_r and $\mu_0\Delta H$ for both ZFC_{1.2T} and FC_{1.2T} protocols experience a rapid increase changing by about 0.12 T and 0.065 T, respectively. These results agree with an observed difference in ZFC- and FC- $M(T)$ (fig. 4.28). A higher M for the FC- $M(H)$ corresponds to the lower μ_0H_r and the opposite stands for the ZFC case. This effect can be understood by a higher magnetic homogeneity of the system when cooling it under the external magnetic field. Qualitatively, the FMR signal intensity decreases with increasing T across the magneto-structural phase transition, which correlates with the reduction of the FM component observed at low-fields area on $M(H)$ (fig. 4.29).

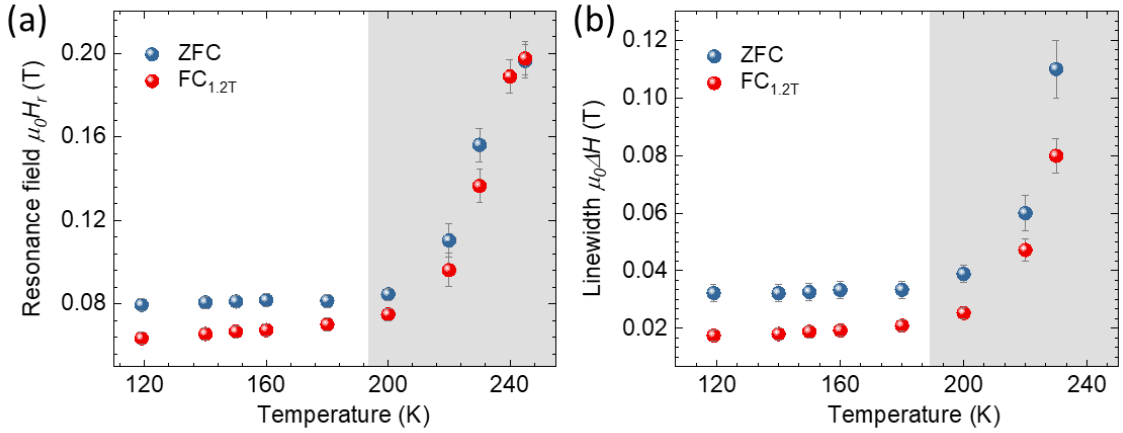


Figure 4.43 Temperature-dependent (a) resonance field $\mu_0 H_r$ and (b) linewidth $\mu_0 \Delta H$ measured for the zero-field-cooled (ZFC) and field-cooled at 1.2 T (FC) protocols with a magnetic field applied parallel to the film plane. The light grey area represents the magneto-structural transition.

High-temperature absorption derivatives were obtained for the temperature range $450 \text{ K} \leq T \leq 530 \text{ K}$ to examine a magnetic phase transition area from an AFM to a presumably PM state near T_t of 507 K, which is discussed in chapter 4.2.4. A magnetic field was applied in the film plane for all measurements. Microwave absorption derivatives and corresponding $\mu_0 H_r$ and $\mu_0 \Delta H$ are presented in figs. 4.44(a) - (b), respectively. $\mu_0 H_r$ and $\mu_0 \Delta H$ were determined according to the procedure described in chapter 3.2.3.

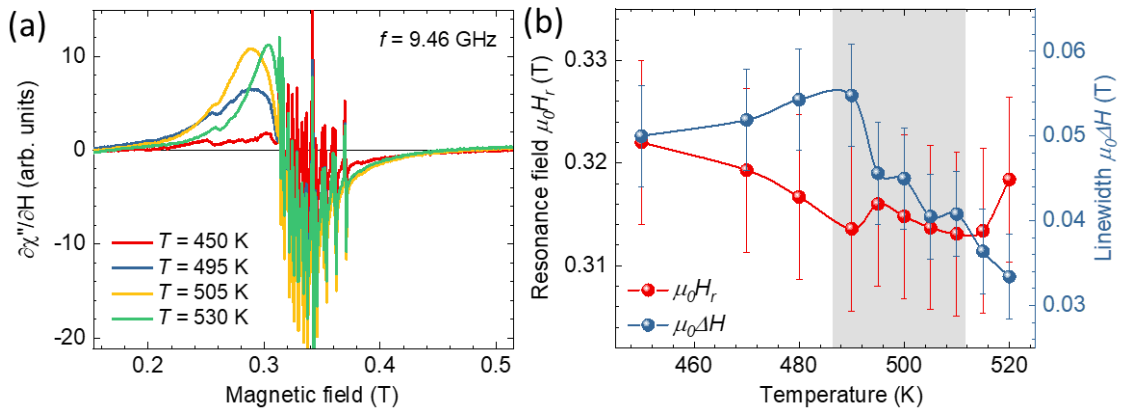


Figure 4.44 (a) Temperature-dependent absorption derivatives for the Mn_2GaC film obtained for $450 \text{ K} \leq T \leq 530 \text{ K}$. (b) Extracted resonance field $\mu_0 H_r$ and linewidth $\mu_0 \Delta H$, grey area defines the magnetic phase transition observed in fig. 4.29.

Approaching T_t , there is almost no signal observed for 450 K, whereas at 500 K and higher, the FMR signal emerges in the vicinity of a magnetic field that corresponds to a g -factor of the free electron. It means that all observed signals are just a bit lower than a PM region. The presence of signals confirms that there is a non-zero M at $T > T_t$, which correlates to $M(H)$ shown in fig. 4.32. $\mu_0 H_r$ does not experience any significant shift within the studied temperature range, while $\mu_0 \Delta H$ showed about 10 % increase in the

vicinity of T_t – a behavior that can be interpreted as an indication of a phase transition. As it was discussed in chapter 4.2.6, the FMR signal showed a weak angular dependence at T_t , which supports a FM contribution to a signal.

As for the $(\text{Cr}_{0.5}\text{Mn}_{0.5})_2\text{GaC}$ films in chapter 4.1.3, here we evaluate the effective magnetization $\mu_0 M_{\text{eff}}$ by taking into account the model of a film with an applied field in the film plane. For the calculation, eq. 2.31 was used and a g -factor of 2 was assumed. Consequently, $K_{2\perp}$ was determined by eq. 2.31. The temperature-dependent $\mu_0 M_{\text{eff}}$ and $K_{2\perp}$ are presented in figs. 4.45(a) and (b), respectively. $\mu_0 M_{\text{eff}}$ follows the magneto-structural phase transition exhibiting a plateau below 200 and dropping above. The splitting between $\text{ZFC}_{1.2\text{T}}$ and $\text{FC}_{1.2\text{T}}$ reflects in the observed $M(T)$ behavior as well. Both protocols show a negative $K_{2\perp}$, which decreases its magnitude with increasing T while approaching the transition to an AFM state (see fig. 4.45). The negative sign implies that M lies in the film plane defining an easy axis for a magnetic anisotropy. To compare the magnitude of $K_{2\perp}$ with well-known materials, a magnetically soft permalloy $\text{Ni}_{81}\text{Fe}_{19}$ exhibits a nearly zero $K_{2\perp}$ [46], whereas a pure Fe $K_{2\perp}$ gives values of about 48 kJ/m^3 [47]. Some magnetically hard materials show three or more orders of magnitude larger $K_{2\perp}$, for example, CoPt with $K_{2\perp}$ of about $4.9 \times 10^3 \text{ kJ/m}^3$ or SmCo₅ which possesses $K_{2\perp}$ of about $17.2 \times 10^3 \text{ kJ/m}^3$ [47]. Therefore, the Mn_2GaC film does not demonstrate a strong magnetic anisotropy.

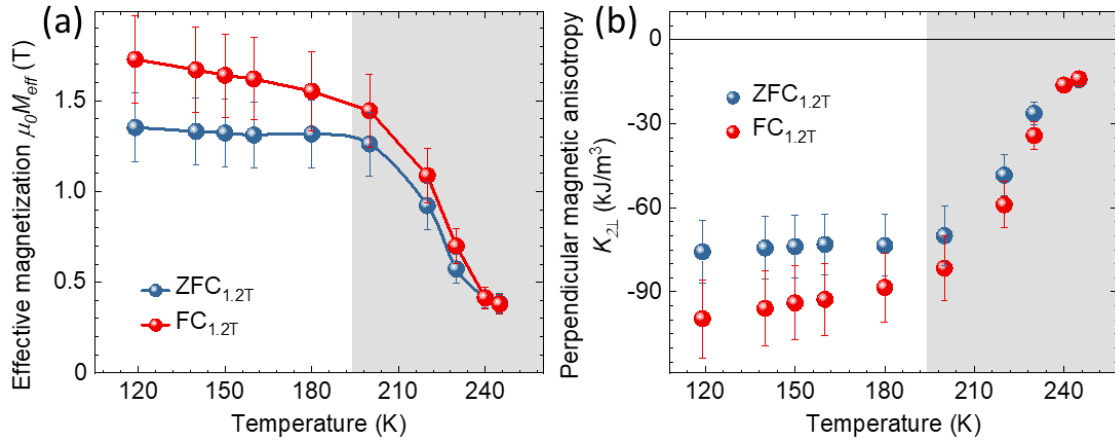


Figure 4.45 Temperature-dependent (a) effective magnetization $\mu_0 M_{\text{eff}}$, and (b) perpendicular magnetic anisotropy constant $K_{2\perp}$ for the zero-field-cooled ($\text{ZFC}_{1.2\text{T}}$) and field-cooled at 1.2 T ($\text{FC}_{1.2\text{T}}$) protocols.

4.2.8 Correlation of electronic, magnetic and structural properties

For the qualitative analysis and direct comparison, the magnetic field dependencies of the MS, MR and magnetization are plotted together on one graph for the temperature above and below the magneto-structural phase transition (fig. 4.28). In fig. 4.46(a) at magnetic fields up to 1.5 T, at 280 K, the MS displays a plateau indicating that the c -lattice parameter remains constant. The magnetization shows a rapid linear response to the applied magnetic field, what can be interpreted in a way the magnetic field leads

to a canting of the magnetic moments and provides the net magnetization without noticeable change in the crystal lattice. At magnetic fields above 1 T the magneto-structural transformation occurs as the compression of the atomic planes, manifested by the increase in negative MS, and the magnetization goes sharply up to a plateau at $\sim 5 - 6$ T. An opening on the magnetization field dependence $M(H)$ could be addressed by irreversible magneto-structural transformations.

At 200 K (fig. 4.46(b)) below the magneto-structural phase transition, the MS is found to be positive and the magnetization (blue curve) reveals the opposite behavior. It sharply increases at the magnetic field below 1 T following by further magnetic moments alignment towards FM state, which causes lattice tension marked as increase of MS (red circles). When magnetic field exceed 1 T, FM spin alignment requires a larger distance between Mn-C-Mn slabs across the Ga atomic layers, which results in an expansion of the lattice. Observed magneto-structural transformations are in line with the DFT calculations [34, 88, 89], which predict a strong influence of the magnetic configuration on the *c*-lattice variation in Mn_2GaC with competing AFM and FM interactions across the Ga atomic layers.

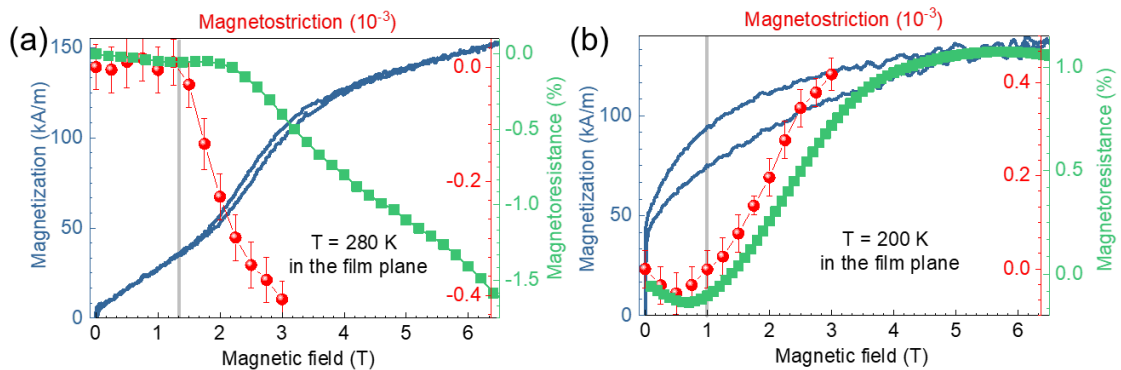


Figure 4.46 Combined plots for magnetostriction (red circles and red inner scale bar to the right), magnetization (blue line) and magnetoresistance (green squares) measured for (a) 280 K and (b) 200 K. Adapted from [98].

Electrical conductivity also shows a noticeable response to the magneto-structural transformations. Fig. 4.46(a) show that the compressive *c*-axis strain (negative MS) leads to a decrease of the electrical resistivity delivering -1.4% of MR at $T > T_t$ and 6 T applied magnetic field. It indicates that the decrease of the *c*-axis lattice parameter leads to a higher concentration of the charge carriers at EF and, accordingly the decrease of resistivity. Although the magnetization and the MS show good correlation as a function of field, MR in fig. 4.46(a)decreases at larger fields. This delay in response of the MR is a direct result of the formation of lattice imperfections when structural deformations begin. The decrease of the carrier mobility due to enhanced lattice imperfections compensates the contribution from the increased carrier concentration due to lattice compression ensuring that the MR remains almost constant up to 2 T. At the point when the MS approaches its saturation, the MR begins to decrease as the

increased carrier concentration dominates. The positive MS, which arises due to the tensile strain for temperatures below T_t results in an increase of the interlayer distance, and the charge carrier concentration decreases, where the MR reaches + 1 % at 6 T. This simplified picture of changing the carrier concentration at the Fermi level qualitatively explains the sign change of MR whilst crossing T_t of 214 K. However, a spin dependent scattering of charge carriers must also be involved in Mn_2GaC , similar to what has been found for $(\text{Mn}_{0.5}\text{Mn}_{0.5})_2\text{GaC}$ thin films [95]. In fig. 4.46(b), the rapid increase of the magnetization below 1 T with a negligibly small MS is accompanied by negative MR of about - 0.1 % which is still smaller than the positive MR caused by c -lattice tension at larger magnetic fields.

5 Conclusions

The structural and magnetic characterization of the $(\text{Cr}_{0.5}\text{Mn}_{0.5})_2\text{GaC}$ and Mn_2GaC MAX phase films were presented. Examination of the magnetic response on external stimuli such as temperature and magnetic field, magnetic phase transitions, magnetostriction, magnetoresistance, magnetic anisotropy, stabilization of different magnetic configurations under field-cooling, and thickness-dependence of magnetic properties were discussed within the present thesis.

(Cr_{0.5}Mn_{0.5})₂GaC.

Heteroepitaxial films synthesized by the magnetron sputtering on MgO substrate form chemically homogeneous layers with nanosized percolation on the surface due to the step-flow growth mode. No *c*-lattice strain within 12.5 - 156 nm-films was observed. The thickness dependence of magnetic properties was studied magnetometry and ferromagnetic resonance (FMR). At 100 K, the films did not show significant changes in magnetic response and can be characterized as soft FM material with the magnetization M_{57} of 200 kA/m, the coercive field of less than 4 mT and the remanent magnetization of less than 25 kA/m. $M(T)$ showed a broad magnetic phase transition with the transition temperature of about 230 K; a smeared $M(T)$ shape and the splitting between zero-field-cooled (ZFC) and field-cooled (FC) $M(T)$ indicate the presence of mixed magnetic interactions. FMR showed broad resonance signals with the linewidth $\mu_0\Delta H$ of 45 ± 5 mT for 20.8 – 156 nm films and 61 ± 5 mT for the 12.5 nm film. The resonance field position μ_0H_r was found to be thickness-independent for 20.8 – 156 nm; the 12.5 nm film had a higher μ_0H_r that points to a stronger magnetic anisotropy contribution. At $T = 300$ K, the FMR signal was still present for all thicknesses, which is consistent with the magnetometry results that show mixed magnetic interactions in the system. The angular-dependent μ_0H_r for 110 K showed a similar trend for all films with the perpendicular uniaxial magnetic anisotropy constant $K_{2\perp}$ of $10.5 \text{ kJ/m}^3 \pm 10\%$. The films were found to be environmentally stable without change of magnetic properties for more than one year at ambient conditions without any capping layer. The possibility to vary thickness in the range 20.8 - 156 nm with similar magnetic response combined with their stability at ambient conditions make these films potentially attractive for applications, where corrosion resistance is required.

Mn₂GaC.

In contrast to the $(\text{Cr}_{0.5}\text{Mn}_{0.5})_2\text{GaC}$ films, the ternary compound Mn_2GaC demonstrated a more complex magnetic response. The Mn_2GaC film exhibits a broad magneto-structural phase transition from a noncollinear ferromagnetic state to an antiferromagnetic state with T_t of about 214 K. The splitting between ZFC and FC $M(T)$ measured at $\mu_0H = 0.2$ T of about 57 % confirms competing magnetic interactions or/and a noncollinear magnetic state with a canting angle of M . The second magnetic transition was observed at $T = 507$ K as a peak in $M(T)$ which defines a transition from

an antiferromagnetic to a magnetically disordered state. This transition temperature is the highest reported value for magnetic MAX phases which opens a venue of its use in electronic components operating at extreme temperatures. Magneto-structural transformations across T_t resulted in an observed large uniaxial magnetostriction of 450 ppm. Additionally, this effect was accompanied by a sign change: under the magnetic field applied parallel to the film plane, the c -axis of the unit cell experienced compression at $T < T_t$ or expansion at $T > T_t$ of the same magnitude. This may be used in valve components that operate in the vicinity of T_t . A noncollinear antiferromagnetic state with spin-reorientation transition at $T = 214$ K can be effectively tuned by cooling the material across the magneto-structural phase transition with or without μ_0H . FMR demonstrated that by cooling the material with or without magnetic field it is possible to reach about 30 % change in μ_0H_r and 40 % in $\mu_0\Delta H$. A complex formation of the magnetic configuration with presumably unsaturated state governs this effect. Therefore, the material can be suggested as a candidate for remote-controlled actuators, when a change of magnetic response can be performed without an exchange of the operating component but by the special cooling procedure that includes a magnetic field of less than 2 T. Mn_2GaC exhibits a highly asymmetric change of the magneto-resistance under applied μ_0H of ± 9 T. In addition, the magnetoresistance reaches up to 3 % at $\mu_0H = 2.2$ T at $T = 300$ K with the sign change. A complex non-monotonous behavior can be used in applications that measure MR and, thus, can determine a magnetic history of the specimen. By measuring the sign of the MR , it could be possible to identify whether the object was situated in a negative or a positive μ_0H .

Comparison of $(\text{Cr}_{0.5}\text{Mn}_{0.5})_2\text{GaC}$ and Mn_2GaC .

To compare both compounds, it may be considered that the substitution of 50 % Mn by slightly smaller Cr atoms in $(\text{Cr}_{0.5}\text{Mn}_{0.5})_2\text{GaC}$ relieves a frustration of magnetic sublattices by breaking the competing interactions within Mn-Ga-Mn slabs and, thus, disrupts magneto-structural transformations. However, a Cr-Mn combination on the M -site results in a broader magnetic phase transition than in Mn_2GaC . Furthermore, the MAX phase $(\text{Cr}_{0.5}\text{Mn}_{0.5})_2\text{GaC}$ films have been synthesized in a thickness range from 10 to 570 nm with high phase purity over the whole thickness range [26]. In contrast, no phase pure Mn_2GaC film is reported in the literature with thinner than 100 nm; the competing Mn_3GaC phase was present in most cases. The combined approach of characterization techniques towards fundamental investigation of the magnetic MAX phases' response to the external magnetic field and temperature demonstrated a strong correlation of spin, lattice and electronic structure. The observed magnetic properties reveal the potential to explore new functionalities. The results suggest the use of these materials as components for spintronic devices, surface resistant sensors and magnetic coatings. New element combinations could lead to complementary useful material responses that will successfully promote magnetic MAX phase films towards industrial applications.

6 Outlook

During the last decade, MAX phases were produced by many techniques, one of the most developed for a magnetic MAX phase film synthesis is magnetron sputtering [86]. Recently, non-conventional techniques like microwave heating and spark-plasma sintering were offered for a magnetic MAX phases synthesis of a good quality and profitable cost production [153, 154]. Regardless of the method, a synthesis of complex magnetic MAX phases itself needs to be optimized in terms of phase purity, thickness and composition control. A possibility to combine more than three elements opens a way to tune material properties such as magnetization, magnetic anisotropy or ordering temperature.

MAX phases for flexible electronics could be beneficial because of their crack healing properties [16]. Stabilization of magnetic MAX phase on flexible substrates [155] and investigation of its performance as a function of stress is a perspective research area.

Inspired by a MAX phases' diversity, reports about new magnetic MAX phase compounds appear in the literature much more often than a comprehensive study of their properties. For example, magnetic microstructure and domains' formation in any kind of magnetic MAX phases have not yet been reported up to my knowledge, albeit an observed lateral grains formation of about 150 nm for the magnetic MAX phase $(Cr_{0.5}Mn_{0.5})_2GaC$ film [26] have raised my interest towards this study.

Mn_2GaC MAX phase compound, once produced in bulk, may be of interest for magnetic shape memory alloys due to its magneto-structural changes upon applied temperature or magnetic field. Such alloys remember the predefined shape before magnetic field is applied [156]. Then, after mechanical deformations like stretching, this material is able to come back to its initial state that was "programmed" by an applied magnetic field. This effect is possible to reach due to reversible magneto-structural phase transition between two crystal structures stabilized at certain temperature range.

Theoretical prediction of stable MAX phases containing Fe, Ni or Co and its subsequent synthesis remains a challenging task, the first Fe-based MAX phase film was produced in 2017 [157]. Potentially, it could enhance magnetization and improve related properties like magnetostriction or magnetocaloric effect.

Investigation of two-dimensional, "graphene-like", MXenes [15] is another rapidly expanding field of research evolved right after MAX phases. In that light, MAX phases serve as precursors for a chemical or a physical process of separating M-X-M sheets of the material by removing A element [158]. With the possibility of composition modification at a wide range, Ti-based MXenes Ti_3C_2 already showed high performance as antennas for wireless communication and supercapacitors. No experimental evidence regarding magnetic MXene is reported so far, which opens a venue of further exploration.

7 Appendix

A1. Magnetic characterization of the substrate

MgO (111) single crystals were used as substrates for deposition of $(\text{Cr}_{0.5}\text{Mn}_{0.5})_2\text{GaC}$ and Mn_2GaC by magnetron sputtering at Linköping University, Sweden. These substrates were chosen after comparing the quality of films deposited on 4H-SiC (0001) and Al_2O_3 (0001) [26]. The MgO (111) substrate provides the best quality of epitaxial layers with preferred *c*-axis orientation normal to the substrate basal plane [26].

The influence of the substrate can be significant, especially if its contribution to the total magnetization of the film on the substrate is strong, as in thin films. The substrate contributes with a temperature-independent DM part and can also contain a temperature-dependent part due to PM impurities. The particle-induced X-ray emission (PIXE) analysis showed that commercially available MgO substrate crystals may contain impurity ions such as Fe, Cr, V, and Mn [113]. Their presence is observed by the appearance of EPR lines [113]. The majority of the impurities are magnetically isolated metal ions.

The temperature-dependent magnetization of a blank MgO substrate was measured to evaluate its contribution to the total signal. To characterize the substrate, the magnetic susceptibility χ was plotted as a function of temperature (fig. A.1(a)). It is calculated from the measured magnetic moment normalized with respect to the substrate volume and divided by the applied magnetic field of $\mu_0H = 0.2$ T. The temperature dependence correlates with that described in reference [113]. It shows a sharp increase at low temperatures, which is an indicator of the presence of a Langevin PM component, and it becomes negative above 50 K, where the DM contribution dominates. The magnetization curves are presented in the inset of fig. A.1(a). At high-temperatures, the field-dependence is linear with the slope increasing as the temperature rises, and at low-temperatures, the signal has a complex S-shape arising from the competition of strong paramagnetism and diamagnetism.

The magnetic susceptibility of the substrate χ_{sub} can be described as a sum of the temperature-independent DM χ_{DM} component and the temperature-dependent PM χ_{PM} component. According to the Curie-Weiss law, χ_{PM} is directly proportional to the effective Curie constant C' of the PM contribution and is inversely proportional to the temperature [47]. Therefore, it can be written as $\chi = \chi_{\text{DM}} + C'/T$. The multiplication of this equation on both sides by the temperature gives $\chi T = \chi_{\text{DM}}T + C'$. If χT is plotted as a function of T , then χ_{DM} becomes the slope and C' the intercept with the ordinate (fig. A.1(b)). From the linear fit for 50 – 300 K, the obtained χ_{DM} and C' are $-1.812 \pm 0.002 \times 10^{-5}$ and $5.50 \pm 0.04 \times 10^{-4}$ K, respectively. The DM contribution is consistent to the literature values for a pure MgO of $\chi_{\text{DM}} = -2 \times 10^{-5}$ [113] and $\chi_{\text{DM}} = -1.80 \times 10^{-5}$ [113]. In this thesis, C' is found to be of about 20 % larger than that

reported $C' = 4.4 \times 10^{-4}$ K in [113]. Thus, studied MgO showed an anticipated magnetic behavior, which made it a suitable substrate for a magnetic film with a FM signal of a rather small magnitude.

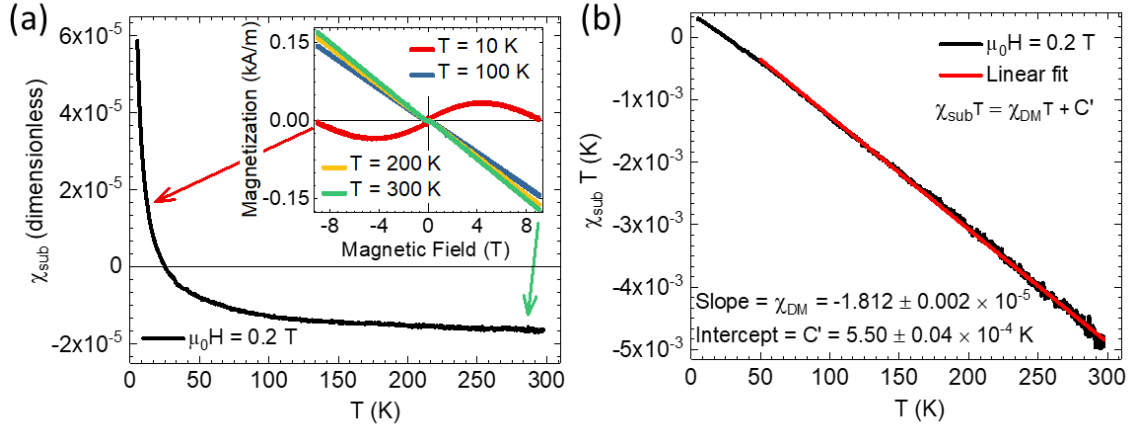


Figure A.1 (a) Temperature-dependent magnetic susceptibility of the blank MgO χ_{sub} measured with an applied magnetic field of $\mu_0H = 0.2$ T. Inset shows field-dependent magnetization curves at 10, 100, 200 and 300 K. (b) $\chi_{\text{sub}}T$ as a function of temperature. A linear fit gives a diamagnetic contribution χ_{DM} and the effective Curie constant C' .

A2. Local homogeneity of the films

The EDX spectroscopy (chapter 3.1.2) was used to examine the local homogeneity of the MAX phase $(\text{Cr}_{0.5}\text{Mn}_{0.5})_2\text{GaC}$ films with the thicknesses of 12.5 and 156 nm.

Fig. A.2(a) shows the measured EDX spectrum of the $(\text{Cr}_{0.5}\text{Mn}_{0.5})_2\text{GaC}$ 12.5 nm film on MgO substrate. Besides the four elemental peaks which corresponds to the film (Cr, Mn, Ga and C), additional peaks of Mg and O originate from the MgO substrate; the Cu peak is an artefact peak that arises from the sample holder [102]. In contrary, the generated spectrum for the elements of the film only shows the elemental peaks with respect to the experimental spectrum (fig. A.2(b)). The measured carbon peak C has a higher relative intensity than the generated one; this effect occurs due to a carbon's high probability of an elastic scattering [102]. In present samples, the EDX signal is dominated by the strong contribution from the MgO substrate (fig. A.2(a)). This effect is typically observed for a class of specimens made of a thin film on top of a bulk substrate and is governed by the penetration depth of the electron beam [102]. The described influence results in a decreased peak-to-background ratio for the characteristic peaks from the elements of the film which makes a quantitative analysis of the composition difficult [102].

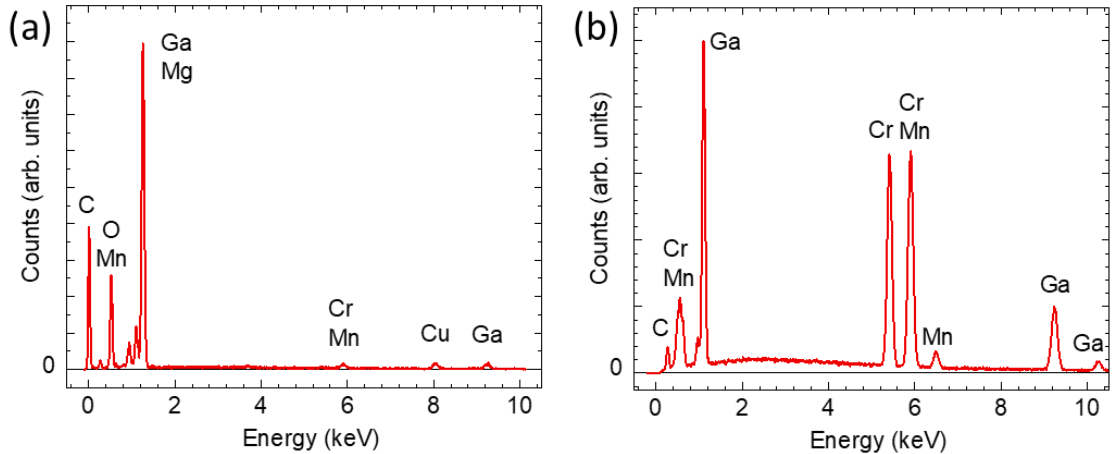


Figure A.2 (a) Measured EDX spectrum of the 12.5 nm $(\text{Cr}_{0.5}\text{Mn}_{0.5})_2\text{GaC}$ film. (b) Generated in INCA 4.4 EDX spectrum of a homogeneous $(\text{Cr}_{0.5}\text{Mn}_{0.5})_2\text{GaC}$ compound. For both EDX spectra, the accelerating voltage of 20 kV was used.

The penetration depth and the interaction volume of the electron beam with the $(\text{Cr}_{0.5}\text{Mn}_{0.5})_2\text{GaC}$ 12.5 nm film on MgO was simulated in CASINO (chapter 3.1.2). The simulation for the beam energies of 2 and 20 kV (fig. A.3) was used to illustrate the dominant substrate contribution to the EDX signal. The simulation parameters included the width of the electron beam of 2 nm, the angle of incidence that is perpendicular to the surface, and 200 electron trajectories to provide a sufficient amount of individual electron trajectories in the specimen volume. The specimen was defined according to given composition of $(\text{Cr}_{0.5}\text{Mn}_{0.5})_2\text{GaC}$ and the thickness was set

to 12.5 nm which was derived from XRR (table 4.1). In the simulation, blue trajectories define the electrons that are stopped inside the specimen due to an inelastic scattering; red trajectories originate from the electrons that are backscattered (fig. A.3).

Qualitative comparison shows that for the beam energy of 2 kV, the penetration depth is about 60 nm so the film is still visible (fig. A.3(a)). In contrary, for the beam energy of 20 kV, the penetration depth is above 4500 nm; therefore, the film's contribution to the EDX signal becomes smaller (fig. A.3(b)). Besides the penetration depth, the simulation provides an information about the straggling effect which is defined as a spread of the electrons' trajectories that are stopped inside the specimen. On the relative scale, the straggling increases from about 100 nm to about 6000 nm. The increase of both, the penetration depth and the straggling effect, result in the interaction volume increase by at least two orders of magnitude.

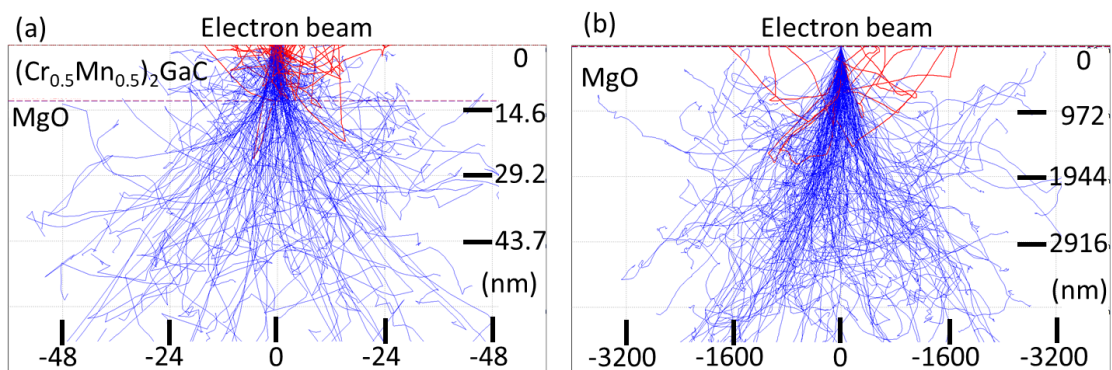


Figure A.3 Monte Carlo simulation of the penetration depth in the 12.5 nm $(\text{Cr}_{0.5}\text{Mn}_{0.5})_2\text{GaC}$ film at the beam energy of (a) 2 kV and (b) 20 kV with the beam oriented perpendicular to the surface. The simulation is performed for 200 electron trajectories.

Due to these challenges, the quantitative analyzation is difficult for the thin film on a thick substrate; nevertheless, the local homogeneity of the samples can be studied. The SEM images of the 12.5 and 156 nm films of $(\text{Cr}_{0.5}\text{Mn}_{0.5})_2\text{GaC}$ and the 100 nm film of Mn_2GaC were analyzed by the EDX mapping method (chapter 3.1.2). In the present work, the mapping matrix consisted of (512×382) measurement points. For each point, EDX detected a spectrum of the specimen's surface. By repeating scans with an automatic drift control, each point is kept on the exact position of the surface and, thus, held the full information of the measured spectrum. Further processing of the mapping matrix provided the local variation of elements. For this analysis, the EDX mapping matrix was divided into (50×40) squares; thus, each square held a certain amount of measurement points. The INCA software combines the obtained information into a summarized EDX spectrum that represents the at.% distribution of containing elements within the limitation of the thin film effect [102].

The presence of clusters was observed on the films' surfaces. Its origin was investigated in addition to the magnitude of the elements' distribution. First, the SEM image of the 12.5 nm $(\text{Cr}_{0.5}\text{Mn}_{0.5})_2\text{GaC}$ film with a cluster on the surface is presented in

fig. A.4(a). Obtained local element distributions of Mn, Ga and Cr are shown in figs. A.4(b) - (d), respectively. The local element variations are discussed within the error bar of an individual EDX spectrum that reaches about 1 at.%, because generated EDX signals from the main film components are obstructed by the substrate contribution. All analyzed elements exhibit local variations of less than 0.8 at.%; such small variations allow to describe the specimen as a homogeneous layer of Cr-Mn-Ga compound. The cluster on the film's surface (fig. A.4(a)) has an excessive amount of Mn and Ga ($\gg 2$ at.%) which is shown as white color on the color plots (figs. A.4(b) - (c)); however, Cr was found to have a local element variation of up to 2 % only on the one side of the cluster. It can be concluded that the clusters on the film surface are Mn-Ga dominated.

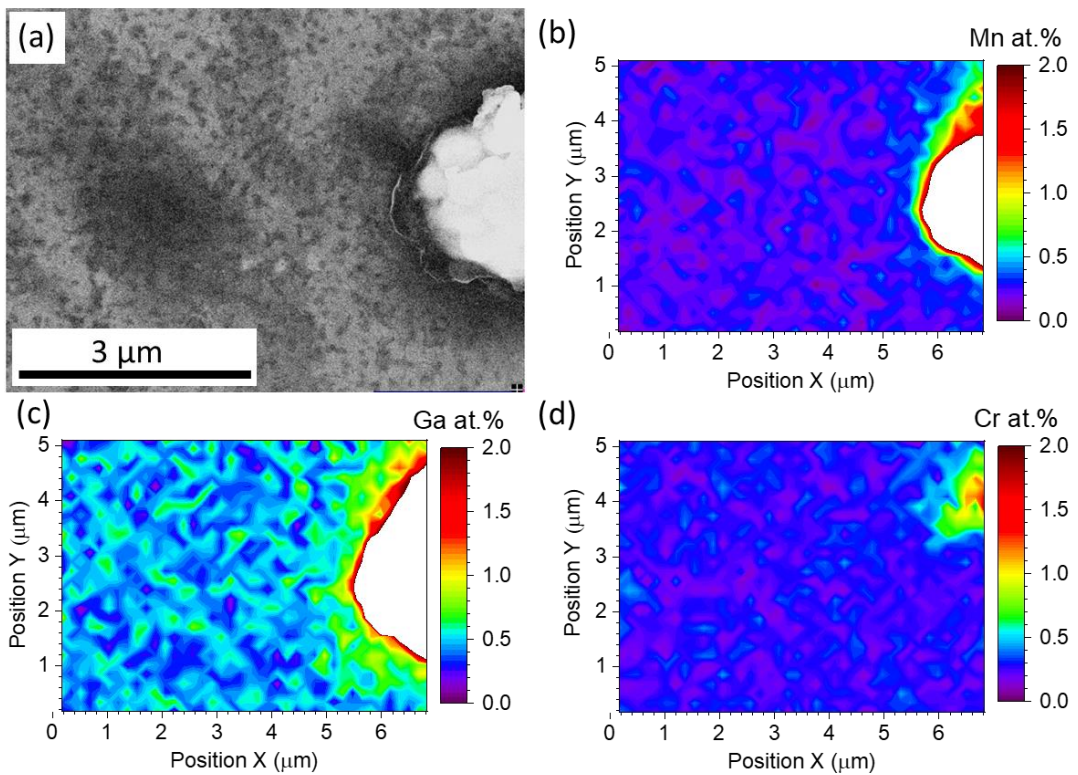


Figure A.4 (a) Scanning electron microscopy image of the 12.5 nm $(\text{Cr}_{0.5}\text{Mn}_{0.5})_2\text{GaC}$ film and the EDX mapping of the corresponding area for the (b) Mn, (c) Ga and (d) Cr element distribution.

The SEM image of the 156 nm $(\text{Cr}_{0.5}\text{Mn}_{0.5})_2\text{GaC}$ film with a cluster on the surface (fig. A.5(a)). The dark area on the bottom left part of the image is the overexposed surface due to the carbon deposition and it appears in the case of a protracted adjustment procedure and does not affect the EDX analysis. This cluster has an elongated shape and the lateral size of about $(20 \times 4) \mu\text{m}$. The local elements distribution over the surface is homogeneous (figs. A.5(b) - (d)) as in the case of the 12.5 nm film. Due to the thicker film thickness, the absolute values in at.% are higher, but show the same small variation as in the thinner sample. In the cluster area, the

excessive Ga amount is observed; it is accompanied by a slight reduction of Mn and a strong reduction of Cr.

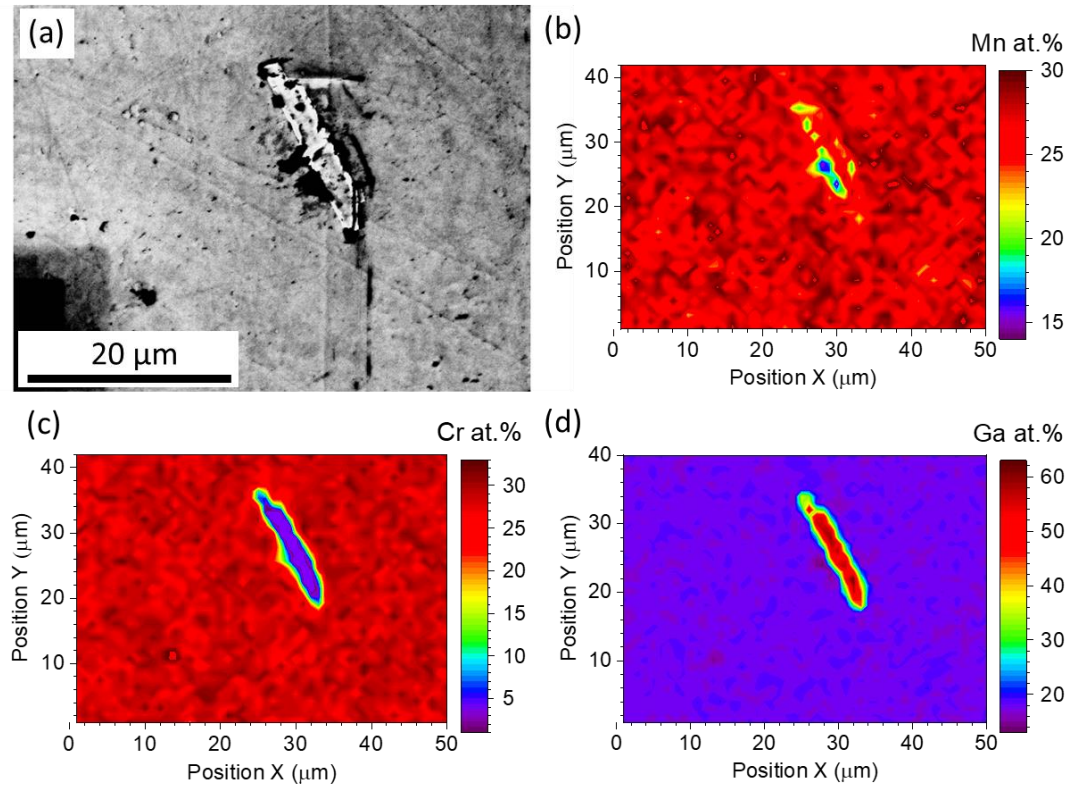


Figure A.5 (a) Scanning electron microscopy image of the 156 nm $(\text{Cr}_{0.5}\text{Mn}_{0.5})_2\text{GaC}$ film and the EDX mapping of the corresponding area for the (b) Mn, (c) Ga and (d) Cr element distribution.

List of Figures

Figure 1.1 (a) $M_{n+1}AX_n$ phase unit cell with the c -axis normal to the basal plane. (b) Nanolaminated $M_{n+1}AX_n$ phase structure with $n = 1$, where the monolayer of the A element is interleaved by $M-X-M$ slabs. M , A and X atoms are colored red, blue and black, respectively. Stronger bonds between $M-X-M$ and weaker bonds between $M-A-M$ layers are schematically shown on the left side by the grey solid lines. Redrawn from [14].	2
Figure 2.1 Classical types of magnetic order in (a) paramagnetic, (b) ferromagnetic, (c) ferrimagnetic, and (d) antiferromagnetic solid materials. Red arrows indicate orientation of the magnetic moments. Redrawn from [47].	6
Figure 2.2 Magnetic field-dependent magnetization for an arbitrary ferromagnetic material. The saturation magnetization M_s , the coercive field H_c and the remanent magnetization M_r are indicated.	7
Figure 2.3 Representation of a domain wall of (a) Bloch and (b) Néel type. The domain wall is the area between the blue dashed lines. Adapted from [52].	8
Figure 2.4 Representation of an electron e scattering path (green arrow) through (a) ordered crystal lattice, (b) crystal lattice with atomic defects and imperfections and (c) ordered crystal lattice that experience thermal vibrations. σ is the electrical conductivity and μ is the electron mobility. The drawing is adapted from [69].	12
Figure 2.5 Representation of the film geometry with respect to an external magnetic field H , resulting magnetization M and corresponding azimuthal φ_H and polar θ_H angles for H . Redrawn from [75].	14
Figure 2.6 Common growth mechanisms of thin films. (a) Frank-van-der-Merve growth, (b) Vollmer-Weber growth, (c) Stranski-Krastanov growth. Redrawn from [90, 91].	20
Figure 2.7 Schematically presented components of the magnetron sputtering setup. Targets with different material are shown in green, red and purple. The corresponding atoms shown as circles follow the same color code. Electrons are indicated as circles with a minus sign. The Ar gas flow is indicated by yellow dots. Redrawn from [14].	21
Figure 3.1 Representation of the Bragg's condition for a maximum constructive interference according to eq. 3.1.	26
Figure 3.2 Information regarding the film specimen that X-ray reflectivity can provide. Red and green curves are arbitrary XRR profiles for one and two interfaces, respectively. Redrawn from [101].	26
Figure 3.3 Schematic of the VSM option in the PPMS, adapted from [107]. The sample is fixed on a rod that is connected to the vibrational drive unit. The sample moves through the detection coils.	30
Figure 3.4 MPMS-XL detection coils configuration with respect to the specimen, which is attached to a straw-holder. On the right side, an induced voltage of the specimen that moves through the gradiometer detection system. The z -axis defines the specimen's position and the y -axis shows an output voltage. Adapted from [107].	31
Figure 3.5 Experimental configuration for electrical resistivity measurements using a standard 4-probe geometry. I and V indicate current and voltage, respectively. + and - specify their directions. The values s_x define the spacing between the probes. Adapted from [71].	32
Figure 3.6 Schematic of the experimental setup for the angular- and temperature-dependent ferromagnetic resonance studies based on a resonant cavity. Frequency range can be extended by complementary microwave bridges besides a standard X-band bridge.	33
Figure 3.7 Schematic of the experimental setup for the frequency- and temperature-dependent ferromagnetic resonance detection. Adapted from [111].	35
Figure 3.8 (a) Sample (green) mounted on the short-circuited end of the semi-rigid coaxial cable (yellow). An alternating magnetic field (red) is induced by the microwave near-field effect from the	

microwave short at the specimen area. (b) The semi-rigid cable with the microwave short and the mounted specimen. On the Teflon holder, the modulation coil is visible as well as the holder for the temperature sensor. Adapted from [111, 112].	35
Figure 3.9 Ferromagnetic resonance signal measured at 110 K for the zero-field-cooled (ZFC) Mn_2GaC film. The resonance field H_r and linewidth ΔH are marked. The red-colored part of the signal (magnified in the inset) displays multiple sharp resonances that originate from inclusions incorporated in the MgO substrate. The black dashed line indicates the linear background contribution.	36
Figure 4.1 $\theta - 2\theta$ X-ray diffraction scan of the $(\text{Cr}_{0.5}\text{Mn}_{0.5})_2\text{GaC}$ films for (a) 12.5 nm, (b) 20.8 nm, (c) 40.3 nm, and (d) 156 nm. (111) reflections originate from the MgO substrate. Adapted from [116].	40
Figure 4.2 Comparison of the (0006) peak position for the 12.5 nm, 20.8 nm, 40.3 nm and 156 nm $(\text{Cr}_{0.5}\text{Mn}_{0.5})_2\text{GaC}$ films. The violet asterisk marks peaks that may originate from tilted grains or from a trace amount of Cr_4Ga [116].	41
Figure 4.3 X-ray reflectivity profiles and corresponding fits for the (a) 12.5 nm, (b) 20.8 nm, and (c) 40.3 nm $(\text{Cr}_{0.5}\text{Mn}_{0.5})_2\text{GaC}$ films. Adapted from [116].	42
Figure 4.4 Scanning electron microscopy images of a surface for the (a) 12.5 nm, (b) 20.8 nm, (c) 40.3 nm, and (d) 156 nm $(\text{Cr}_{0.5}\text{Mn}_{0.5})_2\text{GaC}$ films. Data adapted from [116].	43
Figure 4.5 Scanning electron microscopy image for the 20.8 nm $(\text{Cr}_{0.5}\text{Mn}_{0.5})_2\text{GaC}$ film tilted by 60° .	43
Figure 4.6 (a)-(c) Scanning electron microscopy images for the 12.5 nm $(\text{Cr}_{0.5}\text{Mn}_{0.5})_2\text{GaC}$ film's surface and (d)-(f) respective overlaying masks (red) that identify a pores' area obtained using ImageJ [117, 119].	44
Figure 4.7 Temperature-dependent magnetic moment measured at $\mu_0 H = 0.02$ T applied parallel to the film plane for the (a) 156 and (b) 20.8 nm $(\text{Cr}_{0.5}\text{Mn}_{0.5})_2\text{GaC}$ films.	45
Figure 4.8 Temperature-dependent magnetization measured at $\mu_0 H = 0.2$ T applied parallel to the film plane for the (a) 156 nm, (b) 40.3 nm and (c) 20.8 nm $(\text{Cr}_{0.5}\text{Mn}_{0.5})_2\text{GaC}$ films. The background from the substrate has been subtracted (fig. A.1). Insets show the derivatives of $M(T)$ (red) with an "adjacent averaging filter" (black) of 5 and 10 points for 40.3 nm and 20.8 nm, respectively.	46
Figure 4.9 (a) Field-dependent magnetic moment for the 156 nm, 40.3 nm, 20.8 nm and 12.5 nm $(\text{Cr}_{0.5}\text{Mn}_{0.5})_2\text{GaC}$ films on MgO (111) at $T = 100$ K with $\mu_0 H$ applied parallel to the film plane. (b) Magnetization curves obtained from (a) after the background subtraction using a linear function fitted to the data between 3.5 and 5 T and after normalization with respect to volume of the films. The inset shows the magnification for ± 0.4 T.	47
Figure 4.10 Angular-dependent resonance field $\mu_0 H_r$ for the 156 nm $(\text{Cr}_{0.5}\text{Mn}_{0.5})_2\text{GaC}$ film at 110 K. A rotation was performed by changing (a) the azimuthal angle, or (b) the azimuthal and polar angles. The red solid lines represent the best match of the fit by Smit-Beljers approach to experimental data.	50
Figure 4.11 Angular-dependent resonance field $\mu_0 H_r$ measured at 110 K for the (a) 40.3 nm, (b) 20.8 nm, and (c) 12.5 nm $(\text{Cr}_{0.5}\text{Mn}_{0.5})_2\text{GaC}$ films. The angle of 0° defines the external magnetic field applied perpendicular to the film plane. The solid red line represents the result of fits by the Smit-Beljers approach. (d) angular-dependent linewidth $\mu_0 \Delta H$ at 110 K for all investigated films.	51
Figure 4.12 (a) Ferromagnetic resonance spectra for the 156 nm, 40.3 nm, 20.8 nm and 12.5 nm $(\text{Cr}_{0.5}\text{Mn}_{0.5})_2\text{GaC}$ films measured at 110 K. A magnetic field was applied parallel to the film plane. Narrow resonances between 0.31 and 0.38 T shown in the inset for 300 K originate from MgO inclusions. (b) Magnification of the FMR signal. Data adapted from [116].	53
Figure 4.13 Temperature-dependent resonance field $\mu_0 H_r$ for the 156 nm, 40.3 nm, 20.8 nm and 12.5 nm $(\text{Cr}_{0.5}\text{Mn}_{0.5})_2\text{GaC}$ films with a magnetic field applied in the film plane. Adapted from [116].	54
Figure 4.14 (a) Temperature-dependent linewidth $\mu_0 \Delta H$ for the 12.5 nm, 20.8 nm, 40.3 nm and 156 nm $(\text{Cr}_{0.5}\text{Mn}_{0.5})_2\text{GaC}$ films; (b) Field-dependent absorption derivatives for the 20.8 nm film at 110, 180 and	

240 K. Positions, where the <i>y-axis</i> is zero, are displayed by the black solid line for each individual measurement.....	54
Figure 4.15 Thickness-dependent effective magnetization $\mu_0 M_{eff}$ at $T = 110$, 190 and 240 K for the 156 nm, 40.3 nm, 20.8 nm and 12.5 nm $(Cr_{0.5}Mn_{0.5})_2GaC$ films. Partially adapted from [116].....	55
Figure 4.16 (a) Thickness-dependent perpendicular magnetic anisotropy constant $K_{2\perp}$ for the 156 nm, 40.3 nm, 20.8 nm and 12.5 nm $(Cr_{0.5}Mn_{0.5})_2GaC$ films at 110 K for the case when a magnetic field is applied in the film plane. (b) $K_{2\perp}$ multiplied by the thickness d (blue circles) to determine the volume K_V and surface K_S contributions from the linear fit (red line).....	57
Figure 4.17 (a) $K_{2\perp}$ versus $M(T)/M(100\text{ K})$ for α determination according to eq. 2.23. (b) Comparison between $K_{2\perp}(T)/K_{2\perp}(100\text{ K})$ and $M(T)/M(100\text{ K})^\alpha$. Data analyzed for the 156 nm $(Cr_{0.5}Mn_{0.5})_2GaC$ film.	58
Figure 4.18 Normalized absorption derivatives measured on the same sample for the 20.8 nm $(Cr_{0.5}Mn_{0.5})_2GaC$ film with a magnetic field applied in the film plane recorded for the time interval of 1 year. Adapted from [116].....	59
Figure 4.19 $\theta - 2\theta$ X-ray diffraction scan for the 100 nm Mn_2GaC film measured at $T = 300$ K. An asterisk at about 40 deg. is attributed to trace amounts of Mn_3GaC (111) [98].	60
Figure 4.20 Mn_2GaC film on MgO :(a) Bright-field transmission electron microscopy (TEM) image, cross-section; (b) High-angle annular dark-field scanning TEM (HAADF/STEM) image, cross-section. White or grey points correspond to Ga or Mn atomic columns, respectively. Selected area electron diffraction patterns recorded (c) in the plane of the film with the [0001] zone axis and (d) the cross-section of the [0110] zone axis. (e) The line-scan analysis using STEM/energy-dispersive X-ray (EDX) spectroscopy along the yellow arrow on the HAADF/STEM image that demonstrates a Ga and Mn distribution. Adapted from [98].....	61
Figure 4.21 Scanning electron microscopy images for the (a), (c) 100 nm and (b), (d) 370 nm Mn_2GaC films to compare their surface morphology.	62
Figure 4.22 High-resolution X-ray diffraction scan in the vicinity of the (0006) reflection as a function of the scattering vector Q at magnetic fields of $0\text{ T} \leq \mu_0 H \leq 3\text{ T}$ applied parallel to the film plane: (a) below and (b) above the magneto-structural phase transition at 214 K [98].....	64
Figure 4.23 (a) Field-dependent interplane distance Δd with respect to the d-spacing at zero field d_0 for 200 and 280 K with a magnetic field applied parallel to the Mn_2GaC film plane. (b) Magneto-structural transformations across the transition temperature T_t shown on a doubled unit-cell: (I) At $T > T_t$, the system has an AFM configuration and the spin alignment is predominantly collinear. (II) At $T < T_t$, the Mn_2GaC undergoes a magnetic phase transition characterized by a magnetic spin trans-formation to a noncollinear AFM state resulting in a <i>c</i> -lattice compression ($C_{II} < C_I$). An external magnetic field initiates a parallel spin alignment for (III) and (IV) cases, resulting in a <i>c</i> -lattice compression ($C_{III} < C_I$) and expansion ($C_{IV} > C_{II}$), respectively. Adapted from [98].....	65
Figure 4.24 Relative <i>c</i> -lattice change with respect to the reference at 270 K at $\mu_0 H = 0$. Blue and red circles represent states at $\mu_0 H = 0$ and 3 T, respectively. The grey area indicates the magneto-structural phase transition. Redrawn from [98].	66
Figure 4.25 (a) Temperature-dependent electrical resistivity ρ for different external magnetic fields including cooling and warming curves, (b) Magneto-structural phase transition area, where the splitting between the cooling and warming branches was observed. Adapted from [98].....	67
Figure 4.26 (a) Temperature-dependent electrical resistivity ρ measured at $\mu_0 H = 0$, 5 and 9 T applied parallel to the film plane. (b) Corresponding derivatives over the temperature.....	68
Figure 4.27 Magnetoresistance of the Mn_2GaC film for (a) 200 K, (b) 230 K and (c) 300 K. (d) Magnification of $\mu_0 H = \pm 2.5$ T for (c). Arrows represent the sweeping direction and numbers define the measurement order. Adapted from [98].	69

Figure 4.28 Zero-field-cooled (ZFC), field-cooled (FC) and field-warmed (FW) temperature-dependent magnetization $M(T)$ for the 100 nm Mn ₂ GaC film. Adapted from [98].	70
Figure 4.29 Field-warmed (FW) and field-cooled (FC) temperature-dependent magnetization $M(T)$ measured at 1 T applied parallel to the film plane. Adapted from [98].	71
Figure 4.30 Zero-field-cooled (ZFC) and field-cooled (FC) temperature-dependent magnetization for the 100 nm Mn ₂ GaC film after heating up to 850 K, which does not follow the initial $M(T)$ shown in fig. 4.28.	72
Figure 4.31 (a) Field-dependent magnetic moment for the 100 nm Mn ₂ GaC film. (b) Field-dependent magnetization for 150 K $\leq T \leq$ 300 K after background subtraction and normalization with respect to the film volume. Inset shows a low-fields area. A magnetic field was applied parallel to the film plane. Adapted from [98].	73
Figure 4.32 (a) Field-dependent magnetization $M(H)$ in the range of 500 K $\leq T \leq$ 850 K for the 100 nm Mn ₂ GaC film with the magnetic field applied in the film plane. (b) Low-fields area. Data were normalized with respect to the film volume and are presented after background subtraction.	74
Figure 4.33 (a) Isothermal magnetization curves for the 100 nm Mn ₂ GaC film measured from 150 K to 340 K with 5 K step. (b) Temperature-dependent entropy change ΔS for applied magnetic fields in the range of 0 – 0.5, 0 – 1.0 and 0 – 2.0 T. Solid lines are guides for the eye [98].	75
Figure 4.34 Absorption derivatives measured at 100 K for the Mn ₂ GaC film for the (a) field-cooled (FC _{9T}) and (b) zero-field-cooled (ZFC _{9T}) protocols at different frequencies. Measurements were performed with a magnetic field applied parallel to the film plane.	76
Figure 4.35 (a) Frequency-dependent resonance field $\mu_0 H_r$ and (b) linewidth $\mu_0 \Delta H$ for the zero-field-cooled (ZFC _{9T}) and field-cooled (FC _{9T}) protocols. Measurements were performed at 100 K with an external magnetic field applied in the film plane.	77
Figure 4.36 Frequency-dependent absorption derivative for the MgO substrate measured at 100 K. (a) Frequency-dependent resonance field $\mu_0 H_r$ with the fit according to the EPR resonance condition and (b) linewidth $\mu_0 \Delta H$ for the zero-field-cooled (ZFC _{9T}) and field-cooled (FC _{9T}) protocols.	77
Figure 4.37 (a) Absorption derivatives for the Mn ₂ GaC film on the MgO substrate measured at 110 K for angles $92^\circ \leq \varphi \leq 352^\circ$. The inset demonstrates a relative ratio between signals from the substrate and the film. (b) The linewidth $\mu_0 \Delta H$ and the resonance position $\mu_0 H_r$ as a function of angle.	79
Figure 4.38 Angular-dependent absorption derivatives for the Mn ₂ GaC film measured at 110 K for the (a) zero-field-cooled (ZFC _{1.2T}) and (b) field-cooled (FC _{1.2T}) protocols. Insets show a schematic of the angle rotation.	80
Figure 4.39 Angular-dependent resonance field $\mu_0 H_r$ for the zero-field-cooled (ZFC _{1.2T}) and field-cooled (FC _{1.2T}) protocols along with the fits by the Smit-Beljers approach using (a) a standard description of the magnetization M and (b) an implemented effective canting angle of M . (c) Angular-dependent linewidth $\mu_0 \Delta H$ for the same protocols. (d) Rotation of angles for a film specimen.	81
Figure 4.40 (a) Raw field-dependent magnetic moment for the 100 nm Mn ₂ GaC film. (b) Field-dependent magnetization after background subtraction and normalization with respect to the film volume. (c) and (d) represent magnified fields of ± 1.2 and ± 0.04 T. Measurements were performed with a magnetic field applied parallel to the film plane following the zero-field-cooled (ZFC) and field-cooled (FC) protocols. The field in the underscore (e.g. ZFC _{1.2T}) defines a measuring field range and magnitude of the field while cooling for the FC case.	83
Figure 4.41 Ferromagnetic resonance spectra for the Mn ₂ GaC film measured in the range of 140 K $\leq T \leq$ 230 K with a magnetic field of 1.2 T applied parallel to the film plane for the (a) zero-field-cooled (ZFC) and (b) field-cooled (FC _{1.2T}) protocols.	84
Figure 4.42 Ferromagnetic resonance spectra measured for the Mn ₂ GaC film at (a) 140 K and (b) 220 K, which are below and above the magneto-structural phase transition (fig. 4.28). Data represent the zero-	

field-cooled (ZFC) and field-cooled at 1.2 T (FC _{1.2T}) protocols with a magnetic field applied parallel to the film plane.....	85
Figure 4.43 Temperature-dependent (a) resonance field μ_0H_r and (b) linewidth $\mu_0\Delta H$ measured for the zero-field-cooled (ZFC) and field-cooled at 1.2 T (FC) protocols with a magnetic field applied parallel to the film plane. The light grey area represents the magneto-structural transition.....	86
Figure 4.44 (a) Temperature-dependent absorption derivatives for the Mn ₂ GaC film obtained for 450 K $\leq T \leq$ 530 K. (b) Extracted resonance field μ_0H and linewidth $\mu_0\Delta H$, grey area defines the magnetic phase transition observed in fig. 4.29.....	86
Figure 4.45 Temperature-dependent (a) effective magnetization μ_0M_{eff} , and (b) perpendicular magnetic anisotropy constant $K_{z\perp}$ for the zero-field-cooled (ZFC _{1.2T}) and field-cooled at 1.2 T (FC _{1.2T}) protocols.	87
Figure 4.46 Combined plots for magnetostriction (red circles and red inner scale bar to the right), magnetization (blue line) and magnetoresistance (green squares) measured for (a) 280 K and (b) 200 K. Adapted from [98].....	88
Figure A.1 (a) Temperature-dependent magnetic susceptibility of the blank MgO χ_{sub} measured with an applied magnetic field of $\mu_0H = 0.2$ T. Inset shows field-dependent magnetization curves at 10, 100, 200 and 300 K. (b) $\chi_{sub}T$ as a function of temperature. A linear fit gives a diamagnetic contribution χ_{DM} and the effective Curie constant C'	96
Figure A.2 (a) Measured EDX spectrum of the 12.5 nm (Cr _{0.5} Mn _{0.5}) ₂ GaC film. (b) Generated in INCA 4.4 EDX spectrum of a homogeneous (Cr _{0.5} Mn _{0.5}) ₂ GaC compound. For both EDX spectra, the accelerating voltage of 20 kV was used.....	97
Figure A.3 Monte Carlo simulation of the penetration depth in the 12.5 nm (Cr _{0.5} Mn _{0.5}) ₂ GaC film at the beam energy of (a) 2 kV and (b) 20 kV with the beam oriented perpendicular to the surface. The simulation is performed for 200 electron trajectories.	98
Figure A.4 (a) Scanning electron microscopy image of the 12.5 nm (Cr _{0.5} Mn _{0.5}) ₂ GaC film and the EDX mapping of the corresponding area for the (b) Mn, (c) Ga and (d) Cr element distribution.	99
Figure A.5 (a) Scanning electron microscopy image of the 156 nm (Cr _{0.5} Mn _{0.5}) ₂ GaC film and the EDX mapping of the corresponding area for the (b) Mn, (c) Ga and (d) Cr element distribution.	100

List of Tables

Table 4.1 Results of XRR measurements for $(Cr_{0.5}Mn_{0.5})_2GaC$ series. The nominal thickness is given besides the parameters obtained from the XRR fit: thickness d , density ρ and roughness r [115]....	42
Table 4.2 $K_{2\perp}$ and g -factor obtained from the FMR data fit by the Smit-Beljers approach for 110 K with a magnetic field applied in the film plane for the $(Cr_{0.5}Mn_{0.5})_2GaC$ films of different thickness d	50
Table 4.3 Resonance field μ_0H_r , effective magnetization μ_0M_{eff} , perpendicular magnetic anisotropy constant $K_{2\perp}$, and linewidth $\mu_0\Delta H$ obtained from the FMR data measured at 110 K for 12.5 nm, 20.8 nm, 40.3 nm and 156 nm $(Cr_{0.5}Mn_{0.5})_2GaC$ films with a magnetic field applied in the film plane.	56
Table 4.4 The residual resistivity ratio (RRR), the magnetoresistance (MR) and the electrical resistivity ρ for the 100 nm Mn_2GaC film at different applied magnetic fields μ_0H	68
Table 4.5 A perpendicular magnetic anisotropy constant $K_{2\perp}$ and effective canting angle θ_{eff} of the magnetization obtained from fits to an angular-dependent resonance field for the zero-field-cooled (ZFC _{1.2T}) and field-cooled (FC _{1.2T}) protocols by the Smit-Beljers approach with a conventional or angular-dependent M term.....	82

List of Publications

1. 2014 **J. P. Novoselova**, A. P. Safronov, O. M. Samatov, I. V. Beketov, H. Khurshid, Z. Nemati, H. Srikanth, T. P. Denisova, R. Andrade, and G. V. Kurlyandskaya. Laser target evaporation Fe₂O₃ nanoparticles for water based ferrofluids: focus on biomedical applications. *IEEE Trans. Magn.*, **50**, 11, 4600504.
DOI: 10.1109/TMAG.2014.2323354.
2. 2015 **I. P. Novoselova**, A. P. Safronov, O. M. Samatov, A. I. Medvedev, and G. V. Kurlyandskaya. Biocompatible ferrofluids with iron oxide nanoparticles fabricated by laser target evaporation. *IEEE Magnetic Letters*, **6**, 6700204.
DOI: 10.1109/LMAG.2015.2471280.
3. 2016 G. V. Kurlyandskaya, **Iu. P. Novoselova**, V. V. Schupletsova, R. Andrade, N. A. Dunec, L. S. Litvinova, A. P. Safronov, K. A. Yurova, N. A. Kulesh, A. N. Dzyuman, I. A. Khlusov. Nanoparticles for magnetic biosensing systems. *Journal of Magnetism and Magnetic Materials*, **431**, 249–254.
DOI: <https://doi.org/10.1016/j.jmmm.2016.07.056>.
4. 2016 **Iu. P. Novoselova**, A. P. Safronov, O. M. Samatov, and G. V. Kurlyandskaya. Magneto-inductive heating of water-based iron oxide ferrofluids. *AIP Conference Proceedings*, **1767**, 020016.
DOI: <http://dx.doi.org/10.1063/1.4962600>.
5. 2016 **I. P. Novoselova**, A. P. Safronov, O. M. Samatov, I. V. Beketov, A. I. Medvedev, and G. V. Kurlyandskaya. Water based suspensions of iron oxide obtained by laser target evaporation for biomedical applications. *Journal of Magnetism and Magnetic Materials*, **415**, 35–38.
DOI: <https://doi.org/10.1016/j.jmmm.2016.01.093>.
6. 2016 N. A. Kulesh, **I. P. Novoselova**, A. P. Safronov, I. V. Beketov, O. M. Samatov, G. V. Kurlyandskaya, M. Morozova, and T. P. Denisova. Total reflection x-ray fluorescence spectroscopy as a tool for evaluation of iron concentration in ferrofluids and yeast samples. *Journal of Magnetism and Magnetic Materials*, **415**, 39–44.
DOI: <https://doi.org/10.1016/j.jmmm.2016.01.095>.
7. 2017 **I. P. Novoselova**, O. M. Samatov, G. S. Kupriyanova, A. M. Murzakaev, A. P. Safronov, G. V. Kurlyandskaya. Magnetic properties of iron oxide nanoparticles obtained by laser evaporation. *Russian Physics Journal*, **59**, 9, 1491–1497.
DOI: 10.1007/s11182-017-0935-8.
8. 2018 **I. P. Novoselova**, A. Petruhins, U. Wiedwald, Á. S. Ingason, T. Hase, F. Magnus, V. Kapaklis, J. Palisaitis, M. Spasova, M. Farle, J. Rosen, and R. Salikhov. Large uniaxial magnetostriction with sign inversion at the first order phase transition in the nanolaminated Mn₂GaC MAX phase. *Scientific Reports*, **8**, 2637.
DOI: 10.1038/s41598-018-20903-2.
9. 2019 **I. P. Novoselova**, A. Petruhins, U. Wiedwald, D. Weller, J. Rosen, M. Farle and R. Salikhov. Long-term stability and thickness dependence of magnetism in thin (Cr_{0.5}Mn_{0.5})₂GaC MAX phase films. *Materials Research Letters*, **7**, 4, 159–163.
DOI: <https://doi.org/10.1080/21663831.2019.1570980>.
10. 2019 A. A. Chlenova, **I. P. Novoselova**, R. Salikhov, M. Farle, V. N. Lepalovskij, J. T. Gorriño, G. V. Kurlyandskaya. Fe_xNi_{100-x} thin film systems with slight deviations from zero magnetostriction compositions: focus on pressure sensor applications. *Key Engineering Materials*, **826**, 11–18.
DOI: <https://doi.org/10.4028/www.scientific.net/KEM.826.11>

Acknowledgements

I acknowledge the Deutsche Akademische Austauschdienst e.V. (DAAD) for the grant "Doctoral Programmes in Germany" № 57214224 I received to finance my Ph.D studies.

I am grateful to Prof. Dr. Michael Farle for the supervision of my doctoral studies and enlightening discussions. I am thankful to Dr. Ruslan Salikhov for the project we worked together on, for coaching me how to plan my experiments independently. I thank our secretaries Helga Mundt and Sabina Grubba, whose brilliant help with paperwork never should be taken for granted.

I would like to thank Prof. Dr. Johanna Rosén and her group members for providing samples and a great collaboration. Especially, I would like to acknowledge Dr. Andrejs Petruhins for his support with X-ray diffraction data acquisition and discussions that resulted in publications.

Furthermore, I would like to express my gratitude to Priv. Doz. Dr. Ulf Wiedwald for the support with scanning electron microscopy (SEM), vibrating sample magnetometry, and electron transport experiments as well as for fruitful discussions and interest in my research. I thank Dr. Marina Spasova for performing transmission electron microscopy study of the highest quality and support with the structural analysis. I am thankful to Dr. Detlef Spoddig for the technical support with SEM and ferromagnetic resonance (FMR). Dr. Ralf Meckenstock, M. Sc. Benjamin Zingsem and M. Sc. Thomas Feggeler are acknowledged for the theoretical support and discussions regarding FMR data interpretation.

I am grateful to Prof. Dr. Mehmet Acet, Dipl.-Ing. Michael Vennemann and Dr. Anna Semisalova for their never-ending enthusiasm in my research and mutual understanding. I am thankful to my fellow students, not individually named, for amiable discussions both scientific and personal, for being such an enjoyable company, support and stress relievers. You always have been there for me, and it was precious to have you by my side during all this time.

I acknowledge discussions with Prof. Dr. Hongbin Zhang regarding theoretical calculations of magnetic anisotropy for the Mn₂GaC film. My thanks go also to Dr. Marek Wojcik and Dr. Ewa Jedryka for test measurements on the Mn₂GaC film using nuclear magnetic resonance and following discussions.

Last but not least, I am immensely thankful to my family and friends for an unconditional support and encouragement.

Bibliography

- [1] O'Handley, R. C. *Modern Magnetic Materials: Principles and Applications*, New York, Chichester, Weinheim, Brisbane, Singapore, Toronto: John Wiley & Sons (2000).
- [2] Haun, J. B., Yoon, T.-J., Lee, H., Weissleder, R. Magnetic nanoparticle biosensors. *Wiley Interdisciplinary Reviews: Nanomedicine and Nanobiotechnology* **2**(3), 291-304 (2010).
- [3] Prokopenko, O. V., Krivorotov, I. N., Bankowski, E., Meitzler, T., Jaroch, S., Tiberkevich, V. S., Slavin, A. N. Spin-torque microwave detector with out-of-plane precessing magnetic moment. *Journal of Applied Physics* **111**, 123904 (2012).
- [4] Ono, H., Ito, T., Yoshida, S., Takase, Y., Hashimoto, O., Shimada, Y. Noble Magnetic Films for Effective Electromagnetic Noise Absorption in the Gigahertz Frequency Range. *IEEE Transactions on Magnetics* **40**(4), 2853 (2004).
- [5] Torrejon, J., Riou, M., Araujo, F. A., Tsunegi, S., Khalsa G., Querlioz D., Bortolotti P., Cros, V., Yakushiji, K., Fukushima, A., Kubota, H., Yuasa, S., Stiles, M. D., Grollier, J. Neuromorphic computing with nanoscale spintronic oscillators. *Nature* **547**, 428 (2017).
- [6] Hellman F., Hoffmann, A., Tserkovnyak, Y., Beach, G. S. D., Fullerton, E. E., Leighton, C., MacDonald, A. H., Ralph, D. C., Arena, D. A., Dürr, H. A., Fischer, P., Grollier J., Heremans, J. P., Jungwirth, T., Kimel, A. V., Koopmans, B., Krivorotov, I. N., May, S. J., Petford-Long, A. K., Rondinelli, J. M., Samarth, N., Schuller, I. K., Slavin, A. N., Stiles, M. D., Tchernyshyov, O., Thiaville, A., Zink, B. L. Interface-Induced Phenomena in Magnetism. *Review of Modern Physics* **89**, 025006 (2017).
- [7] Liu, J. P., Fullerton, E., Gutfleisch, O., Sellmyer, D. J. *Nanoscale Magnetic Materials and Applications*, Dordrecht, Heidelberg, London, New York: Springer (2009).
- [8] Kelly, P. J., Arnell, R. D. Magnetron sputtering: a review of recent developments and applications. *Vacuum* **56**, 159-172 (2000).
- [9] Nowotny, V. Strukturchemie einiger Verbindungen der Übergangsmetalle mit den elementen C, Si, Ge, Sn. *Progress in Solid State Chemistry* **5**, 27-70 (1971).
- [10] Barsoum, M. W. The $M_{N+1}AX_N$ phases: A new class of solids. *Progress in Solid State Chemistry*, **28** 201-281 (2000).
- [11] Sokol, M., Natu, V., Kota, S., Barsoum, M. W. On the Chemical Diversity of the MAX Phases. *Trends in Chemistry* **1**(2), 210-223 (2019).
- [12] Högberg, H., Hultman, L., Emmerlich, J., Joelsson, T., Eklund, P., Molina-Aldareguia, J. M., Palmquist, J. P., Wilhelmsson, O., Jansson, U. Growth and characterization of MAX-phase thin films. *Surface and Coatings Technology* **193**, 6-10 (2005).

- [13] Magnuson M., Mattesini M. Chemical bonding and electronic-structure in MAX phases as viewed by X-ray spectroscopy and density functional theory. *Thin Solid Films* **621**, 108-130 (2017).
- [14] Petruhins, A. *Synthesis and characterization of magnetic nanolaminated carbides*, *Linköping Studies in Science and Technology*, Dissertations, Linköping: Linköping University Electronic Press (2018).
- [15] Eklund, P., Rosen, J., Persson, P. O. Å. Layered ternary $M_{n+1}AX_n$ phases and their 2D derivative MXene: an overview from a thin-film perspective. *Journal of Physics D: Applied Physics* **50**, 113001 (2017).
- [16] Farle, A.-S., Kwakernaak, C., van der Zwaag, S., Sloof, W. G. A conceptual study into the potential of $M_{n+1}AX_n$ -phase ceramics for self-healing of crack damage. *Journal of the European Ceramic Society* **35**, 37-45 (2015).
- [17] Sun, Z. M. Progress in research and development on MAX phases: a family of layered ternary compounds. *International Materials Reviews* **56**(3), 143-166 (2011).
- [18] Low, I. M. An Overview of Parameters Controlling the Decomposition and Degradation of Ti-Based $M_{n+1}AX_n$ Phases. *Materials (Basel)* **12**(3), 473 (2019).
- [19] Meshkian, R., Tao, Q., Dahlqvist, M., Lu, J., Hultman, L., Rosen, L. Theoretical stability and materials synthesis of a chemically ordered MAX phase, Mo_2ScAlC_2 , and its two-dimensional derivate Mo_2ScC_2 MXene. *Acta Materialia* **125**, 476-480 (2017).
- [20] Tao, Q., Lu, J., Dahlqvist, M., Mockute, A., Calder, S., Petruhins, A., Meshkian, R., Rivin, O., Potashnikov, D., Caspi, E. a. N., Shaked, H., Hoser, A., Opagiste, C., Galera, R.-M., Salikhov, R., Wiedwald, U., Ritter, C., Wildes, A. R., Johansson, B., Hultman, L., Farle, M., Barsoum, M. W., Rosen, J. Atomically Layered and Ordered Rare-Earth i-MAX Phases: A New Class of Magnetic Quaternary Compounds. *Chemistry of Materials* **31**, 2476-2485 (2019).
- [21] Dahlqvist, M., Lu, J., Meshkian, R., Tao, Q., Hultman, L., Rosen, J. Prediction and synthesis of a family of atomic laminate phases with Kagome-like and in-plane chemical ordering, *Science Advances*. **3** e1700642 (2017).
- [22] Tao, Q., Dahlqvist, M., Lu, J., Kota, S., Meshkian, R., Halim, J., Palisaitis, J., Hultman, L., Barsoum, M. W., Persson, P. O. Å., Rosen, J. Two-dimensional $Mo_{1.33}C$ MXene with divacancy ordering prepared from parent 3D laminate with in-plane chemical ordering. *Nature Communications*, **8** 14949 (2017).
- [23] Ingason, A. S., Mockute, A., Dahlqvist, M., Magnus, F., Olafsson, S., Arnalds, U. B., Alling, B., Abrikosov, I. A., Hjörvarsson, B., Persson, P. O., Rosen, J. Magnetic self-organized atomic laminate from first principles and thin film synthesis. *Physical Review Letters* **110**, 195502 (2013).
- [24] Ingason, A. S., Petruhins, A., Dahlqvist, M., Magnus, F., Mockute, A., Alling, B., Hultman, L., Abrikosov, I. A., Persson, P. O. Å., Rosen, J. A Nanolaminated Magnetic Phase: Mn_2GaC . *Materials Research Letters* **2**(2), 89-93 (2013).

- [25] Petruhins, A., Ingason, A. S., Dahlqvist, M., Mockute, A., Junaid, M., Birch, J., Lu, J., Hultman, L., Persson, P. O. Å., Rosen, J. Phase stability of $\text{Cr}_{n+1}\text{GaC}_n$ MAX phases from first principles and Cr_2GaC thin-film synthesis using magnetron sputtering from elemental targets. *Physica Status Solidi (RRL) - Rapid Research Letters* **7**(11), 971-974 (2013).
- [26] Petruhins, A., Ingason, A. S., Lu, J., Magnus, F., Olafsson, S., Rosen, J. Synthesis and characterization of magnetic $(\text{Cr}_{0.5}\text{Mn}_{0.5})_2\text{GaC}$ thin films. *Journal of Materials Science*, **50**(13) 4495-4502 (2015).
- [27] Meshkian, R., Ingason, A. S., Arnalds, U. B., Magnus, F., Lu, J., Rosen, J. A magnetic atomic laminate from thin film synthesis: $(\text{Mo}_{0.5}\text{Mn}_{0.5})_2\text{GaC}$. *APL Materials* **3**, 076102 (2015).
- [28] Mockute, A., Persson, P. O. Å., Magnus, F., Ingason, A. S., Olafsson, S., Hultman, L., Rosen, J. Synthesis and characterization of arc deposited magnetic $(\text{Cr},\text{Mn})_2\text{AlC}$ MAX phase films. *Physica Status Solidi (RRL) - Rapid Research Letters* **8**(5), 420-423 (2014).
- [29] Mockute, A., Lu, J., Moon, E. J., Yan, M., Anasori, B., May, S. J., Barsoum, M. W., Rosen, J. Solid Solubility and Magnetism upon Mn Incorporation in the Bulk Ternary Carbides Cr_2AlC and Cr_2GaC . *Materials Research Letters* **3**(1), 16-22 (2014).
- [30] Jungfleisch, M.B., Zhang, W., Hoffmann, A. Perspectives of antiferromagnetic spintronics. *Physics Letters A* **382**(13), 865-871 (2018).
- [31] Stöhr, J., Siegmann, H. C. *Magnetism: From Fundamentals to Nanoscale Dynamics*, Berlin, Heidelberg: Springer (2006).
- [32] Kampfrath, T., Sell, A., Klatt, G., Pashkin, A., Mährlein, S., Dekorsy, T., Wolf, M., Fiebig, M., Leitenstorfer, A., Huber, R. Coherent terahertz control of antiferromagnetic spin waves. *Nature Photonics* **5**, 31-34 (2010).
- [33] Ingason, A. S., Dahlqvist, M., Rosen, J. Magnetic MAX phases from theory and experiments; a review. *Journal of Physics: Condensed Matter* **28**, 433003 (2016).
- [34] Ingason, A. S., Petruhins, A., Rosen, J., Toward Structural Optimization of MAX Phases as Epitaxial Thin Films. *Materials Research Letters* **4**(3), 152-160 (2016).
- [35] Sethulakshmi, N., Mishra, A., Ajayan, P. M., Kawazoe, Y., Roy, A. K., Singh, A. K., Tiwary, C. S. Magnetism in two-dimensional materials beyond graphene. *Materials Today* **27**, 107-122 (2019).
- [36] Berger, O. The correlation between structure, multifunctional properties and application of PVD MAX phase coatings. Part I. Texture and room temperature properties. *Surface Engineering*, DOI 10.1080/02670844.2019.1611195, 1-43 (2019).
- [37] Lai, C.-C., Tao, Q., Fashandi, H., Wiedwald, U., Salikhov, R., Farle, M., Petruhins, A., Lu, J., Hultman, L., Eklund, P., Rosen, J. Magnetic properties and structural characterization of layered $(\text{Cr}_{0.5}\text{Mn}_{0.5})_2\text{AuC}$ synthesized by thermally induced substitutional reaction in $(\text{Cr}_{0.5}\text{Mn}_{0.5})_2\text{GaC}$. *APL Materials* **6**, 026104 (2018).

- [38] Ma, X., Zhang, Q., Luo, Z., Lin, X., Wu, G. A novel structure of Ferro-Aluminum based sandwich composite for magnetic and electromagnetic interference shielding. *Materials & Design* **89**, 71-77 (2016).
- [39] Zhang, Q., Magnetic Field Shielding in Jaroszewski, M., Thomas, S., Rane, A.V. *Advanced Materials for Electromagnetic Shielding*, Hoboken NJ: John Wiley and Sons, 109-146 (2019).
- [40] Dahlqvist, M., Ingason, A. S., Alling, B., Magnus, F., Thore, A., Petruhins, A., Mockute, A., Arnalds, U. B., Sahlberg, M., Hjörvarsson, B., Abrikosov, I. A., Rosen, J. Magnetically driven anisotropic structural changes in the atomic laminate Mn₂GaC. *Physical Review B* **93**, 014410 (2016).
- [41] Thore, A., Dahlqvist, M., Alling, B., Rosen, J. Magnetic exchange interactions and critical temperature of the nanolaminate Mn₂GaC from first-principles supercell methods. *Physical Review B* **93**, 054432 (2016).
- [42] García, N., Muñoz, M., Qian, G. G., Rohrer, H., Saveliev, I. G., Zhao, Y.-W. Ballistic magnetoresistance in a magnetic nanometer sized contact: An effective gate for spintronics. *Applied Physics Letters* **79**, 4550-4552 (2001).
- [43] Egelhoff, W. F., Chen, P. J., Powell, C. J., McMichael, R. D., Stiles, R. D. Surface and interface effects in the growth of giant magnetoresistance spin valves for ultrahigh-density data-storage applications. *Progress in Surface Science* **67**, 355-364 (2001).
- [44] Rifai, D., Abdalla, A. N., Ali, K., Razali, R. Giant Magnetoresistance Sensors: A Review on Structures and Non-Destructive Eddy Current Testing Applications. *Sensors* **16**, 298 (2016).
- [45] Chiang, C.-Y., Jeng, J.-T., Lai, B.-L., Luong, V. S., Lu, C.-C. Tri-axis magnetometer with in-plane giant magnetoresistance sensors for compass application. *Journal of Applied Physics* **117**, 17A321 (2015).
- [46] Getzlaff, M. *Fundamentals of Magnetism*, Berlin, Heidelberg: Springer (2008).
- [47] Coey, J. M. D. *Magnetism and Magnetic Materials*, Cambridge, New York, Melbourne, Madrid, Cape Town, Singapore, Sao Paulo, Dehli, Dubai, Tokyo: Cambridge University Press (2010).
- [48] Schwabl, F., Brewer, W. D. *Statistical Mechanics*, 2nd Edition, Berlin, Heidelberg, New York: Springer (2006).
- [49] Kronmüller, H. Mikromagnetische Berechnung der Magnetisierung in der Umgebung unmagnetischer Einschlüsse in Ferromagnetika. *Zeitschrift für Physik* **168**, 478-494 (1962).
- [50] Abo, G. S., Hong, Y., Park, J., Lee, J., Lee, W., Choi, B. Definition of Magnetic Exchange Length. *IEEE Transactions on Magnetics* **49**(8), 4937-4939 (2013).
- [51] Hurd, C.M. Varieties of magnetic order in solids. *Contemporary Physics* **23**(5), 469-493 (2006).

- [52] Blundell, S. *Magnetism in Condensed Matter*, Oxford: Oxford University Press (2001).
- [53] Landau, L., Lifshitz, E. On the theory of the dispersion of magnetic permeability in ferromagnetic bodies, in Pitaevski, L.P. *Perspectives in Theoretical Physics*, Amsterdam: Pergamon, 51-65 (1992).
- [54] Fallarino, L., Oelschlägel, A., Arregi, J. A., Bashkatov, A., Samad, F., Böhm, B., Chesnel, K., Hellwig, O. Control of domain structure and magnetization reversal in thick Co/Pt multilayers. *Physical Review B* **99**, 024431 (2019).
- [55] Gross, R., Marx, A. *Festkörperphysik*, München: Oldenbourg Wissenschaftsverlag (2012).
- [56] Tishin, A. M., Spichkin, Y. I. *The Magnetocaloric Effect and its Applications*, Bristol and Philadelphia: IOP Publishing (2003).
- [57] Scheibel, F., Gottschall, T., Taubel, A., Fries, M., Skokov, K.P., Terwey, A., Keune, W., Ollefs, K., Wende, H., Farle, M., Acet, M., Gutfleisch, O., Gruner, M.E. Hysteresis Design of Magnetocaloric Materials-From Basic Mechanisms to Applications. *Energy Technology* **6**, 1397-1428 (2018).
- [58] Gibbs, M. R. J. *Modern Trends in Magnetostriction Study and Application*, Dordrecht: Springer (2000).
- [59] Joule, J. P. XVII. On the effects of magnetism upon the dimensions of iron and steel bars. *The London, Edinburgh, and Dublin Philosophical Magazine and Journal of Science* **30**(199), 76-87 (1847).
- [60] Farle, M. Ferromagnetic resonance of ultrathin metallic layers. *Reports on Progress in Physics* **61**, 755-826 (1998).
- [61] Jiles, D. *Introduction to magnetism and magnetic materials*, London: Chapman and Hall (1991).
- [62] Krishnan K.M. *Fundamentals and Applications of Magnetic Materials*, Oxford: Oxford University Press (2016).
- [63] Claeysen F., Lhermet N., Le Letty R., Bouchilloux, P. Actuators, transducers and motors based on giant magnetostrictive materials. *Journal of Alloys and Compounds* **258**, 61-73 (1997).
- [64] Clark A. E., Chapter 7 Magnetostrictive rare earth- Fe_2 compounds in Wohlfarth, E P. *Handbook of Ferromagnetic Materials*, Elsevier, 531-589 (1980).
- [65] Sujan, G.K., Quandt, E. Thin Films: Giant Magnetostrictive in *Reference Module in Materials Science and Materials Engineering*, Elsevier (2016).
- [66] Binasch, G., Grünberg, P., Saurenbach, F., Zinn, W. Enhanced magnetoresistance in layered magnetic structures with antiferromagnetic interlayer exchange. *Physical Review B* **39**(7), 4828-4830 (1989).

- [67] Baibich, M. N., Broto, J. M., Fert, A., Van Dau, F. N., Petroff, F., Etienne, P., Creuzet, G., Friederich, A., Chazelas, J. Giant Magnetoresistance of (001)Fe/(001)Cr Magnetic Superlattices, *Physical Review Letters* **61**(21), 2472-2475 (1988).
- [68] Fayngold, M., Fayngold, V. *Quantum Mechanics and Quantum Information: A Guide through the Quantum World*, Weinheim: Wiley VCH (2013).
- [69] Askeland, D. R., Wright, W. J. *The Science and Engineering of Materials*, 7th Edition, Boston: Cengage Learning (2016).
- [70] Halliday D., Resnick, R., Walker, J. *Fundamentals of Physics*, 10th Edition, Hoboken NJ: John Wiley & Sons (2013).
- [71] Miccoli, I., Edler, F., Pfnür, H., Tegenkamp, C. The 100th anniversary of the four-point probe technique: the role of probe geometries in isotropic and anisotropic systems. *Journal of Physics: Condensed Matter* **27**, 223201 (2015).
- [72] Wesche, R. *Physical Properties of High-Temperature Superconductors*, Chichester: John Wiley & Sons (2015).
- [73] Vonsovskii, S. V. *Ferromagnetic Resonance: The Phenomenon of Resonant Absorption of a High-Frequency Magnetic Field in Ferromagnetic Substances*, Oxford, London, Edinburgh, New York, Toronto, Paris, Frankfurt: Pergamon Press (1966).
- [74] Hubert, A., Schäfer, R. *Magnetic Domains: The Analysis of Magnetic Microstructures*, Berlin, Heidelberg: Springer (1998).
- [75] Meckenstock, R., Untersuchung der magnetischen Eigenschaften von Fe/Ag-Schichtsystemen mit der konventionellen und der ortsaufgelösten ferromagnetischen Resonanz, Dissertation, Bochum: Ruhr-Universität Bochum (1997).
- [76] Callen, H. B., Callen, E. The present status of the temperature dependence of magnetocrystalline anisotropy, and the $l(l+1)2$ power law, *Journal of Physics and Chemistry of Solids* **27**, 1271-1285 (1966).
- [77] Zakeri, K., Kebe, T., Lindner, J., Farle, M., Power-law behavior of the temperature dependence of magnetic anisotropy of uncapped ultrathin Fe Films on GaAs(001). *Physical Review B* **73**, 052405 (2006).
- [78] Mryasov, O. N., Nowak, U., Guslienko, K. Y., Chantrell, R. W., Temperature-dependent magnetic properties of FePt: Effective spin Hamiltonian model. *Europhysics Letters (EPL)* **69**(5), 805-811 (2005).
- [79] Gilbert, T. L. A phenomenological theory of damping in ferromagnetic materials. *IEEE Transactions on Magnetics* **40**(6), 3443-3449 (2004).
- [80] J. Smit, J., Beljers, H. G. Ferromagnetic resonance absorption in BaFe₁₂O₁₉, a highly anisotropic crystal. *Philips Research Reports* **10**, 113-130 (1955).
- [81] Barsukov, I., Meckenstock, R., Lindner, J., Möller, M., Hassel, C., Posth, O., Farle, M., Wende, H. Tailoring Spin Relaxation in Thin Films by Tuning Extrinsic Relaxation Channels. *IEEE Transactions on Magnetics* **46**(6), 2252-2255 (2010).

- [82] Jiang, S., Sun, L., Yin, Y., Fu, Y., Luo, C., Zhai, Y., Zhai, H. Ferromagnetic resonance linewidth and two-magnon scattering in $Fe_{1-x}Gd_x$ thin films. *AIP Advances* **7**, 056029 (2017).
- [83] Nembach, H. T., Silva, T. J., Shaw, J. M., Schneider, M. L., Carey, M. J., Maat, S., Childress, J.R. Perpendicular ferromagnetic resonance measurements of damping and Landé g-factor in sputtered $(Co_2Mn)_{1-x}Ge_x$ thin films. *Physical Review B* **84**, 054424 (2011).
- [84] Zakeri, K., Lindner, J., Barsukov, I., Meckenstock, R., Farle, M., von Hörsten, U., Wende, H., Keune, W., Rocker, J., Kalarickal, S. S., Lenz, K., Kuch, W., Baberschke, K., Frait, Z. Spin dynamics in ferromagnets: Gilbert damping and two-magnon scattering. *Physical Review B* **76**, 104416 (2007).
- [85] Palmquist, J.-P., Jansson, U., Seppänen, T., Persson, P. O. Å., Birch, J., Hultman, L., Isberg, P., Magnetron sputtered epitaxial single-phase Ti_3SiC_2 thin films. *Applied Physics Letters* **81**, 835-837 (2002).
- [86] Eklund, P., Beckers, M., Jansson, U., Höglberg, H., Hultman, L. The $M_{n+1}AX_n$ phases: Materials science and thin-film processing. *Thin Solid Films* **518**, 1851-1878 (2010).
- [87] Schroeder, J. L., Ingason, A. S., Rosén, J., Birch, J. Beware of poor-quality MgO substrates: A study of MgO substrate quality and its effect on thin film quality. *Journal of Crystal Growth* **420**, 22-31 (2015).
- [88] Dahlqvist M., Alling, B., Rosén, J., Stability trends of MAX phases from first principles. *Physical Review B* **81**, 220102 (2010).
- [89] Rosen, J. *Magnetic MAX phases from first principles and thin film synthesis*, Talk (2014).
- [90] Lüth, H. *Solid Surfaces, Interfaces and Thin Films*, Cham, Heidelberg, New York, Dordrecht, London: Springer (2015).
- [91] Mockuté, A. *Synthesis and Characterization of New MAX Phase Alloys, Linköping Studies in Science and Technology*, Dissertations, Linköping: Linköping University Electronic Press (2014).
- [92] Liu, Z., Waki, T., Tabata, Y., Yuge, K., Nakamura, H., Watanabe, I. Magnetic ground state of the $M_{n+1}AX_n$ -phase nitride Cr_2GaN . *Physical Review B* **88**, 134401 (2013).
- [93] Lin, S., Tong, P., Wang, B. S., Huang, Y. N., Lu, W. J., Shao, D. F., Zhao, B. C., Song, W. H., Sun, Y. P. Magnetic and electrical/thermal transport properties of Mn-doped $M_{n+1}AX_n$ phase compounds $Cr_{2-x}Mn_xGaC$ ($0 \leq x \leq 1$). *Journal of Applied Physics* **113**, 053502 (2013).
- [94] Tao, Q., Salikhov, R., Mockute, A., Lu, J., Farle, M., Wiedwald, U., Rosen, J. Thin film synthesis and characterization of a chemically ordered magnetic nanolaminate $(V,Mn)_3GaC_2$. *APL Materials* **4**, 086109, (2016).

- [95] Salikhov, R., Meshkian, R., Weller, D., Zingsem, B., Spoddig, D., Lu, J., Ingason, A. S., Zhang, H., Rosen, J., Wiedwald, U., Farle, M. Magnetic properties of nanolaminated $(\text{Mo}_{0.5}\text{Mn}_{0.5})_2\text{GaC}$ MAX phase. *Journal of Applied Physics* **121**, 163904 (2017).
- [96] Salikhov, R., Semisalova, A. S., Petruhins, A., Ingason, A. S., Rosen, J., Wiedwald, U., Farle, M. Magnetic Anisotropy in the $(\text{Cr}_{0.5}\text{Mn}_{0.5})_2\text{GaC}$ MAX Phase. *Materials Research Letters* **3**(3), 156-160 (2015).
- [97] Ingason, A. S., Pálsson, G. K., Dahlqvist, M., Rosen, J. Long-range antiferromagnetic order in epitaxial Mn_2GaC thin films from neutron reflectometry. *Physical Review B* **94**, 024416 (2016).
- [98] Novoselova, I. P., Petruhins, A., Wiedwald, U., Ingason, A. S., Hase, T., Magnus, F., Kapakis, V., Palisaitis, J., Spasova, M., Farle, M., Rosen, J., Salikhov, R. Large uniaxial magnetostriction with sign inversion at the first order phase transition in the nanolaminated Mn_2GaC MAX phase, *Scientific Reports* **8**, 2637 (2018).
- [99] Inaba, K. X-ray thin-film measurement techniques. I. Overview. *The Rigaku Journal* **24**(1), 10-15 (2008).
- [100] Birkholz, M. *Thin Film Analysis by X-Ray Scattering*, Weinheim: Wiley VCH (2006).
- [101] Yasaka, M. X-ray thin-film measurement techniques. V. X-ray reflectivity measurement. *The Rigaku Journal* **26**(2), 1-9 (2010).
- [102] Goldstein, J. I., Newbury D. E., Michael, J. R., Ritchie, N. W. M., Scott, J. H. J., Joy, D. C. *Scanning Electron Microscopy and X-Ray Microanalysis*, New York: Springer (2018).
- [103] Reimer, L., Kohl, H. *Transmission Electron Microscopy: Physics of Image Formation*, 5th Edition, New York: Springer (2008).
- [104] Leonard, D. N., Chandler, G. W., Seraphin, S. Scanning Electron Microscopy in Kaufmann, E. N. *Characterization of Materials*, New York: John Wiley & Sons (2012).
- [105] Drouin, D. CASINO, <https://www.gel.usherbrooke.ca/casino/>, last accessed: 2019/11/20.
- [106] Quantum Design, *Physical Property Measurement System Vibrating Sample Magnetometer (VSM) Option User's Manual*, Part Number 1096-100, A3 (2008).
- [107] Thomson, T. Magnetic properties of metallic thin films, in Barmak, K., Coffey, K. *Metallic Films for Electronic, Optical and Magnetic Applications*, Oxford Cambridge, Philadelphia, New Delhi: Woodhead Publishing, 454-546 (2014).
- [108] McElfresh, M. *Fundamentals of magnetism and magnetic measurements featuring Quantum Design's Magnetic Property Measurement System*, Quantum Design (1994).
- [109] Jiang, J., Weber, R. T. *ELEXSYS E 500 User's Manual: Basic Operations*, Bruker BioSpin Corporation (2001).
- [110] Chen, L.F., Ong, C.K., Neo, C.P., Varadan, V.V., Varadan, V.K. *Microwave Electronics: Measurement and Materials Characterization*, Chichester: John Wiley & Sons (2004).

- [111] Riebisch, M. *Hochfeld-Ferromagnetische Resonanz zur Untersuchung antiferromagnetischer Wechselwirkungen*, Master Thesis, Duisburg: Fakultät für Physik, Universität Duisburg-Essen (2014).
- [112] Scheibel, F. *Influence of hysteresis at magnetostructural transitions on the magnetocaloric properties of Heuslers, Antiperovskites, and Pnictides*, Dissertation, Duisburg: Fakultät für Physik, Universität Duisburg-Essen (2018).
- [113] Khalid, M., Setzer, A., Ziese, M., Esquinazi, P., Spemann, D., Pöppl, A., Goering, E., Ubiquity of ferromagnetic signals in common diamagnetic oxide crystals. *Physical Review B* **81**, 214414 (2010).
- [114] Flovik, V., Macià, F., Kent, A. D., Wahlström, E. Eddy current interactions in a ferromagnet-normal metal bilayer structure, and its impact on ferromagnetic resonance lineshapes. *Journal of Applied Physics* **117**, 143902 (2015).
- [115] Zingsem, B. A Theory of the Magnetodynamic Response Function, Master Thesis, Duisburg: Fakultät für Physik, Universität Duisburg-Essen (2016).
- [116] Novoselova, I. P., Petruhins, A., Wiedwald, U., Weller, D., Rosen, J., Farle, M., Salikhov, R. Long-term stability and thickness dependence of magnetism in thin $(\text{Cr}_{0.5}\text{Mn}_{0.5})_2\text{GaC}$ MAX phase films. *Materials Research Letters* **7**(4), 159-163 (2019).
- [117] Schindelin, J., Arganda-Carreras, I., Frise, E., Kaynig, V., Longair, M., Pietzsch, T., Preibisch, S., Rueden, C., Saalfeld, S., Schmid, B., Tinevez, J. Y., White, D. J., Hartenstein, V., Eliceiri, K. W., Tomancak, P., Cardona, A. Fiji: an open-source platform for biological-image analysis. *Nature Methods* **9**(7), 676-682 (2012).
- [118] Schneider, C. A., Rasband, W. S., Eliceiri, K. W. NIH Image to ImageJ: 25 years of image analysis. *Nature Methods* **9**(7), 671-675 (2012).
- [119] Hartig, S. M. Basic Image Analysis and Manipulation in ImageJ. *Current Protocols in Molecular Biology* **102**, 14.15.11-14.15.12 (2013).
- [120] Binder, K., Young, A. P. Spin glasses: Experimental facts, theoretical concepts, and open questions. *Reviews of Modern Physics* **58**(4), 801-976 (1986).
- [121] Vincent, E., Dupuis, V. Spin Glasses: Experimental Signatures and Salient Outcomes, in Lookman, T., Ren, X. *Frustrated Materials and Ferroic Glasses*, Cham: Springer, 31-56 (2018).
- [122] Krenke, T., Acet, M., Wassermann, E.F., Moya, X., Mañosa, L., Planes, A. Martensitic transitions and the nature of ferromagnetism in the austenitic and martensitic states of Ni-Mn-Sn alloys. *Physical Review B* **72**, 014412 (2005).
- [123] Ziese, M., Vrejoiu, I., Hesse, D. Structural symmetry and magnetocrystalline anisotropy of SrRuO_3 films on SrTiO_3 . *Physical Review B* **81**, 184418 (2010).
- [124] Scheibel, F., Spoddig, D., Meckenstock, R., Gottschall, T., Çakır, A., Krenke, T., Farle, M., Gutfleisch, O., Acet, M. Room-temperature five-tesla coercivity of a rare-earth-free shell-ferromagnet. *Applied Physics Letters* **110**, 192406 (2017).

- [125] Mathews, M., Postma, F. M., Lodder, J. C., Jansen, R., Rijnders, G., Blank, D. H. A. Step induced uniaxial magnetic anisotropy of $\text{La}_{0.67}\text{Sr}_{0.33}\text{MnO}_3$ thin films. *Applied Physics Letters* **87**, 242507 (2005).
- [126] Dubowik, J., Załęski, K., Głowiński, H., Gościańska, I. Angular dependence of ferromagnetic resonance linewidth in thin films. *Physical Review B* **84**, 184438 (2011).
- [127] Lindner, J., Lenz, K., Kosubek, E., Baberschke, K., Spodig, D., Meckenstock, R., Pelzl, J., Frait, Z., Mills, D. L. Non-Gilbert-type damping of the magnetic relaxation in ultrathin ferromagnets: Importance of magnon-magnon scattering. *Physical Review B* **68**, 060102 (2003).
- [128] Barsukov, I., Römer, F. M., Meckenstock, R., Lenz, K., Lindner, J., Hemken to Krax, S., Banholzer, A., Körner, M., Grebing, J., Fassbender, J., and Farle, M. Frequency dependence of spin relaxation in periodic systems, *Physical Review B* **84**, 140410 (2011).
- [129] Gradmann, U. Surface magnetism. *Journal of Magnetism and Magnetic Materials* **100**, 481-496 (1991).
- [130] Vaz, C. A. F., Bland, J. A. C., Lauhoff, G. Magnetism in ultrathin film structures. *Reports on Progress in Physics* **71**, 056501 (2008).
- [131] Spasova, M., Wiedwald, U., Ramchal, R., Farle, M., Hilgendorff, M., Giersig, M. Magnetic properties of arrays of interacting Co nanocrystals. *Journal of Magnetism and Magnetic Materials* **240**, 40-43 (2002).
- [132] Chatterjee, B. K., Ghosh, C. K., Chattopadhyay, K. K. Temperature dependence of magnetization and anisotropy in uniaxial NiFe_2O_4 nanomagnets: Deviation from the Callen-Callen power law. *Journal of Applied Physics* **116**, 153904 (2014).
- [133] Truong, A., Watanabe, A. O., Sekiguchi, T., Mortemousque, P. A., Sato, T., Ando, K., Itoh, K. M. Evidence of a perpendicular magnetocrystalline anisotropy in a Mn_5Ge_3 epitaxial thin film revealed by ferromagnetic resonance. *Physical Review B* **90**, 224415 (2014).
- [134] Liu, Z., Waki, T., Tabata, Y., Nakamura, H. Mn-doping-induced itinerant-electron ferromagnetism in Cr_2GeC . *Physical Review B* **89**, 054435 (2014).
- [135] Nowak, W. B. Thin metallic films for corrosion control. *Surface and Coatings Technology* **49**, 71-77 (1991).
- [136] Uchikoshi, T., Sakka, Y., Yoshitake, M., Yoshihara, K. A study of the passivating oxide layer on fine nickel particles. *Nanostructured Materials* **4**(2), 199-206 (1994).
- [137] Yu, M.-H., Lewis, L. H., Moodenbaugh, A. R. Large magnetic entropy change in the metallic antiperovskite Mn_3GaC . *Journal of Applied Physics* **93**, 10128-10130 (2003).
- [138] Prosen, R. J., Gran, B. E., Kivel, J., Searle, C. W., Morrish, A. H. Effect of Surface Roughness on Magnetic Properties of Films. *Journal of Applied Physics* **34**, 1147-1148 (1963).

- [139] Johnson, M. T., Bloemen, P. J. H., Broeder, F. J. A. d., Vries, J. J. d. Magnetic anisotropy in metallic multilayers. *Reports on Progress in Physics* **59**, 1409-1458 (1996).
- [140] Bruno, P., Renard, J.-P. Magnetic surface anisotropy of transition metal ultrathin films. *Applied Physics A* **49**, 499-506 (1989).
- [141] Gercsi, Z., Sandeman, K. G. Structurally driven metamagnetism in MnP and related Pnma compounds, *Physical Review B* **81**, 224426 (2010).
- [142] Waseda, Y., Matsubara, E., Shinoda, K. *X-Ray Diffraction Crystallography: Introduction, Examples and Solved Problems*, Heidelberg, Dordrecht, London, New York: Springer (2011).
- [143] Hettinger, J.D., Lofland, S.E., Finkel, P., Meehan, T., Palma, J., Harrell, K., Gupta, S., Ganguly, A., El-Raghy, T., Barsoum, M. W. Electrical transport, thermal transport, and elastic properties of M_2AlC ($M=Ti, Cr, Nb$, and V). *Physical Review B* **72** 115120 (2005).
- [144] Lin, S., Huang, Y., Zu, L., Kan, X., Lin, J., Song, W., Tong, P., Zhu, X., Sun, Y. Alloying effects on structural, magnetic, and electrical/thermal transport properties in MAX-phase $Cr_{2-x}M_xGeC$ ($M = Ti, V, Mn, Fe$, and Mo). *Journal of Alloys and Compounds* **680**, 452-461 (2016).
- [145] Dias, E. T., Priolkar, K. R., Ranjan, R., Nigam, A. K., Emura, S., Mechanism of magnetostructural transformation in multifunctional Mn_3GaC . *Journal of Applied Physics* **122**, 103906 (2017).
- [146] Çakır, Ö., Acet, M. Reversibility in the inverse magnetocaloric effect in Mn_3GaC studied by direct adiabatic temperature-change measurements. *Applied Physics Letters* **100**, 202404 (2012).
- [147] Carlin, R. L., van Duyneveldt, A. J. Special Topics: Spin-Flop, Metamagnetism, Ferrimagnetism and Canting, in Carlin, R. L., van Duyneveldt, A. J. *Magnetic Properties of Transition Metal Compounds*, New York: Springer, 172-194 (1977).
- [148] Das, K., Banu, N., Das, I., Dev, B. N. Significantly large magnetocaloric effect in polycrystalline $La_{0.83}Sr_{0.17}MnO_3$ near room temperature. *Physica B: Condensed Matter* **545**, 438-441 (2018).
- [149] Brustolon, M., Giamello, E. *Electron Paramagnetic Resonance: A Practitioners Toolkit*, Hoboken NJ: John Wiley & Sons (2009).
- [150] Hajihoseini, H., Kateb, M., Ingvarsson, S. P., Gudmundsson, J. T. Oblique angle deposition of nickel thin films by high-power impulse magnetron sputtering. *Beilstein Journal of Nanotechnology* **10**, 1914-1921 (2019).
- [151] Choi, H.-C., You, C.-Y., Kim, K.-Y., Lee, J.-S., Shim, J.-H., Kim, D.-H. Antiferromagnetic layer thickness dependence of noncollinear uniaxial and unidirectional anisotropies in $NiFe/FeMn/CoFe$ trilayers. *Physical Review B* **81**, 224410 (2010).
- [152] Scheibel, F., Zingsem, B., Feggeler, T., Meckenstock, R., Spoddig, D., Farle, M., Acet, M. Magnetic anisotropy of single-crystal antiperovskite Mn_3GaC studied by

ferromagnetic resonance and dynamic magnetic-response simulations. *Physical Review Materials* **3**, 054403 (2019).

[153] Hamm, C. M., Bocarsly, J. D., Seward, G., Kramm, U.I., Birkel, C. S. Non-conventional synthesis and magnetic properties of MAX phases $(\text{Cr/Mn})_2\text{AlC}$ and $(\text{Cr/Fe})_2\text{AlC}$. *Journal of Materials Chemistry C* **5**, 5700-5708 (2017).

[154] Hamm, C. M., Dürrschnabel, M., Molina-Luna, L., Salikhov, R., Spoddig, D., Farle, M., Wiedwald, U., Birkel, C. S. Structural, magnetic and electrical transport properties of nonconventionally prepared MAX phases V_2AlC and $(\text{V/Mn})_2\text{AlC}$. *Materials Chemistry Frontiers* **2**, 483-490 (2018).

[155] Sheng, P., Wang, B., Li, R. Flexible magnetic thin films and devices, *Journal of Semiconductors* **39**(1), 011006 (2018).

[156] Gabdullin, N., Khan, S. H. Review of properties of magnetic shape memory (MSM) alloys and MSM actuator designs. *Journal of Physics: Conference Series* **588**, 012052 (2015).

[157] Lai, C.-C., Petruhins, A., Lu, J., Farle, M., Hultman, L., Eklund, P., Rosen, J. Thermally induced substitutional reaction of Fe into Mo_2GaC thin films. *Materials Research Letters* **5**(8), 533-539 (2017).

[158] Naguib, M., Kurtoglu, M., Presser, V., Lu, J., Niu, J., Heon, M., Hultman, L., Gogotsi, Y., Barsoum, M. W. Two-dimensional nanocrystals produced by exfoliation of Ti_3AlC_2 . *Advanced Materials* **23**, 4248-4253 (2011).

Erklärung

Hiermit versichere ich, dass ich die am heutigen Tage eingereichte Dissertation

Magnetism of atomically laminated MAX phase Mn₂GaC and (Cr_{0.5}Mn_{0.5})₂GaC films

zur Erlangung des akademischen Grades eines Doktors der Naturwissenschaften (Dr. rer. nat.) selbstständig verfasst und in keinem weiteren Promotionsverfahren eingereicht habe. Es wurden keine anderen als die angegebenen Quellen und Hilfsmittel verwendet. Alle wörtlich oder inhaltlich übernommenen Stellen sind durch Zitate angemessen kenntlich gemacht.

Duisburg, den 18.12.2019

Iuliia P. Novoselova